Science Advances
AAAS

Supplementary Materials for

Modern human incursion into Neanderthal territories 54,000 years ago at Mandrin, France

Ludovic Slimak*, Clément Zanolli*, Tom Higham, Marine Frouin, Jean-Luc Schwenninger, Lee J. Arnold, Martina Demuro, Katerina Douka, Norbert Mercier, Gilles Guérin, Hélène Valladas, Pascale Yvorra, Yves Giraud, Andaine Seguin-Orlando, Ludovic Orlando, Jason E. Lewis, Xavier Muth, Hubert Camus, Ségolène Vandevelde, Mike Buckley, Carolina Mallol, Chris Stringer, Laure Metz

*Corresponding author. Email: slimak@univ-tlse2.fr (L.S.); clement.zanolli@gmail.com (C.Z.)

Published 9 February 2022, *Sci. Adv.* **8**, eabj9496 (2022)
DOI: 10.1126/sciadv.abj9496

This PDF file includes:

Supplementary Materials and Methods

X-ray microtomography. All the hominin specimens coming from Layers F to C at Mandrin were scanned using the X-ray microfocus instrument (X-µCT) Phoenix Nanotom 180 set of the FERMAT Federation from the Inter-university Material Research and Engineering Centre (CIRIMAT, UMR 5085 CNRS) of the University of Toulouse. Acquisitions were performed according to the following parameters: 130 kV, 170 µA, 1440 images taken over 360° (0.25° of angular step). The final volumes were reconstructed with a voxel size of 19 µm. The microtomographic acquisitions of the comparative fossil and extant hominid specimens were performed using various equipment including X-µCT and synchrotron radiation (SRX-µCT) and reconstructed with voxel sizes ranging from 9.26 to 53.20 µm.

Data processing. A semi-automatic threshold-based segmentation was carried out in Avizo 8.0 (FEI Visualization Sciences Group) following the half-maximum height method (HMH) (*71*) and the region of interest thresholding protocol (ROI-Tb) (*72*), taking repeated measurements on different slices of the virtual stack (*73*). A volumetric reconstruction was then generated for each specimen.

Crown dimensions. The mesiodistal and buccolingual tooth crown diameters were measured on the digital models (*74*) in Avizo v.8 for the Mandrin specimens. These measurements were compared with Neanderthals, Upper Pleistocene modern humans and Holocene modern humans ranging from the Mesolithic to the 20th century and from Europe (Belgium, Denmark, France, Germany, Hungary, Portugal, Sweden, United Kingdom) and Africa (South Africa) (*75, 76*; see Table S13). Adjusted Z-score analyses (*77, 78*) were performed on the mesiodistal and buccolingual diameter of the Mandrin specimens in comparison with the comparative specimens/samples. This statistical method allows the comparison of unbalanced and small samples, which is often the case when dealing with the fossil record, using the Student's t inverse distribution following the formula: [(x-m)/(s*sqrt(1+1/n)]/(Student.t.inverse(0.05;n-1)), where x is the value of the variable; m is the mean of the same variable for a comparative sample; n is the size of the comparative sample; and s is the standard deviation of the comparative sample.

3D lateral crown tissue proportions. Because of the moderate to advanced wear affecting most of the deciduous and permanent human teeth in the Mandrin assemblage, the 3D assessment of tissue proportions was limited to their lateral (non-occlusal) crown portion. A plane parallel to the cervical best-fit plane and located between the last plane showing a complete ring of enamel and the lowest points of enamel was used to cut the crown at the cervix. A parallel plane was set at the last point of enamel in the occlusal basin and all material above it was removed. The enamel and dentine portions between these two planes were preserved to estimate the lateral crown tissue proportions (*75, 79-81*). The following parameters were thus calculated on the new set of virtually reduced and simplified crowns: the lateral average enamel thickness (3D LAET, in mm) and the scale-free 3D lateral relative enamel thickness (3D LRET). Intra- and interobserver accuracy tests of the measures run by two observers provided differences <5%. Adjusted Z-score analyses (*77, 78*) were performed on the two tooth crown tissue proportions parameters for the Mandrin specimens in comparison with the comparative specimens/samples.

3D root proportions. Once the crown removed using a best-plane at the cervix, the plane was moved toward the root bifurcation and placed through the center of the interradicular surface to divide the roots into the root stem and root branch (*82*). The root stem volume (Vstem; mm^3) and root branch volume (Vbranch; mm^3), were measured and the volumetric bifurcation index (VBI; %) was computed following ref. *82*: Vstem/(Vstem+Vbranch)*100 (Table S19); a value of 0-24.9% denotes a cynotaurodont molar, a value of 25-49.9% indicates a hypotaurodont molar, a value of 50-74.9% corresponds to a mesotaurodont molar, and a value of 75-100% represents a hypertaurodont molar.

Geometric morphometric analyses. Bi-dimensional and three-dimensional geometric morphometric (2D and 3D GM) analyses were conducted on the virtual rendering of the Mandrin tooth crowns. For the deciduous specimens Man11 C 204, Man04 D 395, Man04 D 679 from the Layers C and D that show moderate to advanced occlusal wear, a 2D GM analysis of the occlusal crown outline was performed. The virtual surface of the tooth crown of each specimen was oriented in Avizo v.8 so that the cervical border was perpendicular to the optical axis in both mesio-distal and bucco-lingual directions (*83*). A scale was added on the screen and a screenshot of the occlusal surface was saved as a .jpg file. The pictures of all the specimens in occlusal view were imported in TpsUtil64 (*84*) to create a .tps file. This file was opened in TpsDig2 software (*84*) and a total of 100 equidistant semilandmarks were digitized around the crown (*83, 85*). For the least worn deciduous molar Man12 E 1300 from the Layer E and the first permanent molar Man98 F 811 from the Layer F we performed a 3D GM analyses of the enamel-dentine junction (EDJ). Because the dentine horn apices of some cusps were slightly affected by wear, we reconstructed them following two independent methods (Fig. S13). The first one is a geometric-based approach (geom) in which the virtual slices of each specimen were resampled to be parallel to the cervical plan. A parallel plane was then shifted towards each worn dentine horn extremity and two sections perpendicular to the cervical plane, corresponding respectively to the widest mesiodistal and buccolingual diameters of the last section of the dentine horn and intersecting its center, were used to reconstruct the height and orientation of each apex. Interpolations were then performed for rendering the 3D shape of the tips (*81*). We also reconstructed the dentine horn extremities by using a Neanderthal-like (NEA) and a modern human-like template (MH), respectively. The EDJs of both templates were superimposed on the original shape of the Mandrin specimens. However as illustrated in Fig. S14, while the EDJ morphology of Man12 E 1300 fits well with that of Upper Pleistocene modern human specimens, but it does not align with any of the EDJs of the Neanderthal upper dm2s included in our comparative sample. Whether the Mandrin Layer E tooth EDJ is aligned with respect to the trigon (using the position of the protocone and metacone, as well as that of the oblique crest and preserved portion of the marginal mesial crest) or with the talon (using the position of the protocone, metacone and hypocone, as well as that of the oblique crest, distal marginal crest and lingual marginal crest), the EDJ of the Neanderthal specimens either goes beyond the lingual aspect of Man12 E 1300, especially at the level of the hypocone (when aligned with the trigon) or is too short mesiodistally with respect to the occlusal outline of Man12 E 1300 (when aligned with the talon; Fig. S14). For this reason, we could not fully align the Neanderthal specimen used to reconstruct Man12 E 1300 dentine horns with the latter and we had to virtually cut the EDJ of the Neanderthal tooth into two parts at the level of the oblique crest. Then, the trigon and talon were aligned separately with the Layer E dm2 EDJ and the height and orientation of their dentine horn apices were used to create the NEA chimeric model. For the creation of the MH-based

chimeric model, the alignment was consistent between the specimens and the complete EDJ was used, without cutting the comparative dm2 EDJ. On each of the three reconstructed EDJ surfaces (geom, NEA and MH), five curves of 15 to 30 semilandmark were set along the marginal outline of the EDJ occlusal basin between each pair or cusps. We then computed the between-group principal component analyses (bgPCA) based on the Procrustes residuals and using the following three groups: Neanderthals (NEA), Upper Pleistocene modern humans (UPMH) and Holocene humans (HH). For all teeth, the bgPCA plots show similar group distributions than those obtained with cross-validation (Fig. S12), indicating that no spurious and inflated group separation occurs (*86*). Results of the bgPCA cross-validations exhibit high classification accuracy (from 70% for the LM1 to 85% for the for the complete Udm2 EDJ shape analysis), with most misclassifications happening between UPMH and HH, while only one to three specimens at most are misclassified between NEA and UPMH/HH (Table S20). The Mandrin specimens were then projected *a posteriori* in the bgPCA plots and the posterior probabilities were computed (Table S20). We also performed Jackknife cross-validated canonical variates analyses (CVA) based on the first few principal components (6 to 10 first PC) explaining ~90% of the total variance (*87*) and with the same groups to check the degree of correct classification among groups with another method (Table S21). Altogether, the analyses are consistent with each other and confirm that the groups observed in the bgPCA are not spurious (*86, 88*). We also note that the geometric-based reconstruction (geom) tends to result in straight and vertical dentine horns, which may artificially make it look more modern-like than Neanderthal-like (usually characterized by more internalized dentine horn tips). However, in all 3D GM analyses the three kinds of reconstructions (including NEA) fall close to each other and outside the Neanderthal range, indicating that the orientation of the dentine horn tips plays a minor role in the analyses and that it is the overall position of the dentine horns and crests are mainly responsible for shape differences between groups. The analyses were performed using the package Morpho v.2.7 (*89*) for R v.3.4 (*90*). Allometry was tested using multiple regressions (*91*) in which the explanatory variable is centroid size and the dependent variables are the PC and bgPC scores. For most teeth, the first two components of the bgPCA show no allometry (p-value>0.05), except in bgPC1 of the Udm2 EDJ shape analysis, where a weak allometric signal (p-value<0.01; R^2<0.3) is detected. The differences between specimens thus mostly represent shape-variation.

Since the distal portion of Man12 E 1300 is better preserved and it is a diagnostic region to discriminate between Neanderthals and modern humans (as it relates to the degree of development of the hypocone; *82*), we also conducted a 2D GM and a 3D GM analysis of the Udm2 EDJ restricted to the talon. For the 2D GM analysis, we oriented the EDJ of the specimens in occlusal view following the protocol described above and we placed three curves of 15 to 20 semilandmarks on the images, between the metacone and hypocone, between the protocone and hypocone and along the oblique crest. In the case of Man12 E 1300, the occlusal image of the original EDJ surface (unreconstructed) was used to place the semilandmark curves. We also placed 3D semilandmarks on the surface renderings of the specimens, still at the same position as for the 2D analysis and using the three 3D reconstructions of Man12 E 1300 (geom, NEA and MH). The same multivariate analyses as for the complete semilandmarks set were conducted for both the 2D and 3D analyses of the EDJ talon. Results of the PCA and bgPCA are illustrated in Fig. 7 and the cross-validation statistics are reported in Table S22.

Luminescence Dating

Multiple-grain aliquot quartz optical dating (University of Oxford). In 2014 and 2015, a series of 8 samples was collected in three sections at the Mandrin site. The sampling was carried out under an artificial shelter (opaque plastic tarpaulin) using filtered red light. After thoroughly cleaning the first 2 cm of exposed section, the OSL samples were collected in opaque plastic bags using a trowel. For each sample, an additional amount of sediment was collected in a transparent bag in order to determine the water content and the concentration of radioelements. *Dose rate determination.* For the external dose rate contribution, the beta dose rates were calculated from the uranium, thorium and potassium contents measured on a portion of sediment sub-sample (~8g) by inductively coupled mass spectrometry (ICP-MS) and inductively coupled atomic emission spectroscopy (ICP-AES). External beta dose rates were calculated considering the grain size attenuation factors for quartz (*92*), as well as water content (*93*). The measurement of water content yielded an average value of 12 ± 5 % (at 1σ) by weight at the sampling time. The 2σ uncertainty range of this average value encompasses a wide range of possible water contents during the past between drought and saturation (2% - 22%).

Gamma dose rates were determined from the measurement of the luminescence signal recorded by dosimeters buried in the sequence near the location of the sediment samples. The dosimeters consisted of three pellets of carbon-doped aluminum oxide (Al2O3:C, diameter: 5 mm, thickness: 1 mm) placed at the extremity of a ~30 cm-long metal tube. Before burial, the pellets were heated at 350°C to reset any remaining luminescence signal. The OSL signal measured in the laboratory was compared to those induced by an artificial beta source that had been calibrated using a reference block (*94*). The dosimeters were analyzed at the CRP2A laboratory, University of Bordeaux, France. The measured dose corresponds to a period of burial of 396 days. Each pellet was measured using a Daybreak 2200 OSL reader system (*95*) combining green light stimulation (Nichia NSPG310) and 7.5 mm Hoya U-340 filters for detection. The measured dose includes the present-day cosmic dose and the gamma dose (induced by the decay of radioelements scattered in a volume of $1m^3$ surrounding the measurement point), integrated over the time the dosimeter has been buried. Therefore, gamma doses determined from *in situ* records are more representative than those derived from the U, K, Th concentrations of a portion of sediment (few grams) and determined in the laboratory by gamma-ray spectrometry.

In heterogeneous environments such as Mandrin, where calcareous rocks and blocks are present through the sequence, it is not surprising that doses deduced from dosimeter measurements differ from the doses determined in the laboratory on portions of sediments. Indeed, this difference is to be expected given the difficulty of obtaining representative portions of sediments for laboratory gamma dose rate analyses. We distinguish three situations for gamma dose-rate calculations:

(i) The dose-rates measured *in situ* are systematically lower (~24% lower on average) than those calculated from K, U, and Th concentrations for samples X6717, 6718, 6761 and 6760. These differences arose because of the absence of calcareous lumps in samples analyzed by ICP – therefore the *in situ* measurements are considered the most reliable estimates of gamma dose-rates received by the samples during burial.

(ii) Both the laboratory and *in situ* gamma dose-rate estimates for samples X6719, 6721 and 6723 are similar at 1 sigma. Here we have used the *in situ* measurement for the calculation of the total dose rate to ensure consistency with samples X6717, 6718, 6761 and 6760.

(iii) The gamma dose-rate measured with the dosimeter exhibits an unexpectedly large error (~42% higher than the ICP-based gamma dose-rate) for sample X6720. Layer E is

sedimentalogically almost identical to Layer F, and the U, K, Th content for both samples (X6720 and X6721) are similar. It is therefore difficult to explain the high *in situ* gamma dose for X6720 on sedimentological grounds; though none of the techniques used in this study give any direct information concerning possible radionuclide disequilibrium and non-constant dose-rates through time. Nevertheless, given this is an isolated anomaly accompanied by a large associated uncertainty, we assume that the high *in situ* gamma dose rate for X6720 is due to an analytic problem with this particular dosimeter. The gamma dose rate has therefore been calculated from the concentrations of potassium (K), uranium (U) and thorium (Th) within the sediment.

Cosmic dose rates were calculated from the estimated burial depth of the sediments according to ref. *96*, taking into account the time-averaged geometry of bedrock overburden (see single-grain quartz OSL dating section for additional details). The internal dose rate of coarse quartz grains represents a minor contribution due to the trace amounts of intrinsic radioelements (~1 p.p.b, i.e. 0.001 μg/g) in contrast to the much higher concentrations found within sediments (typically 0.1 to 1 μg/g). An internal dose rate of 0.03 ± 0.02 Gy ka^{-1} (*97,98*) was assumed. The dose rates are given in Table S4.

Quartz preparation and instrumentation. Sample preparation for the multiple-grain OSL dating study involved the extraction of sand-sized (between 90 and 250 μm) quartz grains using wet sieving, hydrochloric acid (10%) and then hydrogen peroxide (30%) digestions, heavy liquid density separations (sodium polytungstate solutions at 2.70 g cm^{-3} and 2.62 g cm^{-3}) and finally etching with hydrofluoric acid (45 %). The purified quartz-rich fractions were dispensed into stainless steel cups over a circa 4 mm diameter area with a silicone oil adhesive.

OSL measurements were conducted using an automated lexsyg research device (*99*) equipped with a $^{90}Sr/^{90}Y$ ring shaped irradiation source (*100*) delivering ca. 0.063 ± 0.001 Gy s^{-1} at the sample position. The quartz OSL signal was stimulated with light from blue LEDs (LZ1-00B200) emitting at 458 nm. The resulting ultraviolet signal was detected by placing an optical filter (Hoya U-340 [7.5 mm]) in front of the photomultiplier tube (Hamamatsu H7360-02). The absence of feldspars was checked for all the samples with near-infrared stimulation using LEDs (LZ1-00R400) emitting at 850 nm, and the resulting signal was detected through a combination of filters (Schott BG 39 and AHF BrightLine HC 414/46). All measurements were performed in a nitrogen atmosphere. A standard single-aliquot regenerative dose (SAR) method (*54, 101*) was applied using successive doses of 30, 60, 120, 200, 0, 30, 30 Gy.

The OSL measurements were carried out for 40 s at 125°C after preheating. A fixed test dose of ~ 10 Gy was given after each natural and regenerative dose and the induced OSL signals (T_n or T_x) used to correct for any sensitivity changes during the successive SAR cycles. Between successive cycles, the samples were stimulation at 280°C and held for 40 s to fully reset the OSL signal. A duplicate regenerative dose was included in the procedure as well as a 'zero dose' to check for suitable sensitivity correction and the absence of thermal transfer, respectively. An extra step was applied to verify possible contamination of the etched quartz grains by feldspars, using an infrared exposure of 40 s at 50 °C (IR depletion-ratio test; *102*).

The net intensity of the OSL signal was integrated over the first 0.8 s, after subtracting the background signal derived from the last 8 seconds of stimulation. The D_e values and their uncertainties were estimated by interpolating the normalized natural OSL signal onto the normalized regeneration dose response curve, which was fitted using a single saturating exponential function of the form $I=I_0(1-\exp^{-D/D0})$. In this function, I corresponds to the intensity (L_x/T_x) at regenerative dose D, I_0 is the saturation value of the exponential curve and D_0 is the

characteristic saturation dose. The sensitivity corrected natural signal (L_n/T_n) was projected onto the fitted dose response curve to obtain the D_e and its associated uncertainty by interpolation using the Analyst software (*103*). The final age uncertainty also includes a further 3% to account for systematic errors in beta source calibration and ICP-MS/AES reproducibility.

Dose recovery test and plateau tests. Preheat plateau tests and dose recovery tests were carried out on three samples X6717, X6720 and X6723 to determine the optimum preheat (PH) temperatures to include in the SAR procedure. 15 aliquots per sample were bleached under natural sunlight for two days to reset any accumulated dose and were then given a known laboratory dose of ~70 Gy. Prior to the Ln and Lx measurements, fixed preheats of between 200°C and 280°C (with steps of 20 °C) for 10 s were applied to each aliquot. A lower temperature cut-heat (CT) was applied prior to the Tn and Tx measurements, which was systematically 40°C lower than the first PH. For all samples, the recovery ratios (given/measured dose) are consistently within 10% of unity, though the preheat combination that gives the best result (with recuperation less than 2%) is with a PH at 240°C for 10 s and a CH at 200°C.

Dose estimates and ages. For each sample, between 14 and 22 aliquots were measured and the resultant D_e values are displayed as AbanicoPlots (*104, 105*) in Fig. S15. For sample X6760, the Ln/Tn signal lay systematically beyond the saturation limit without intersecting the dose response curve, therefore finite age determination was not possible. For other samples, the over-dispersion (OD) values range between 11 and 27%. The origin of such overdispersion is difficult to determine on multi-grain aliquots because of the averaging effects. Based on our dose recovery tests, the overdispersion is expected to be less than 10% for a single population of grains. Therefore, for most samples in this study the additional scatter might be caused by micro-dosimetry variations, heterogeneous bleaching and/or minor post-depositional mixing (see single-grain quartz OSL dating section). For each sample, the accumulated dose is approximated by the unweighted mean of the D_e values, and the final age with its associated errors (at 1σ) is given in Table S5. Age uncertainties are based on the propagation, in quadrature, of random and systematic errors for all measured quantities. We were able to obtain 7 multiple-grain quartz OSL ages from Mandrin (Table S5). Two replicate samples from Layer H gave consistent ages at 86.5 ± 12.8 ka (X6761) and 85.9 ± 6.3 ka (X6723); the uppermost part of Layer F dates to 56.7 ± 6.9 ka (X6721), and the succession between F and E dates to 54.6 ± 2.9 ka (X6720). Subsequently, Layers D, C and B2, are dated to 51.6 ± 3.9 ka (X6719), 48.3 ± 3.5 ka (X6718) and 43.1 ± 3.2 ka (X6717), respectively.

Single-grain quartz optical dating (University of Adelaide). Four luminescence dating samples (MAN19-3 to MAN19-6) were additionally collected from Layers C, E and F in 2019, and analyzed at the University of Adelaide's Prescott Environmental Luminescence Laboratory (PELL). The 2019 luminescence dating study focused on single-grain quartz OSL analyses in order to gain further insights into any potential methodological complications that could have affected multiple-grain aliquot OSL dating in this setting; particularly the presence of insufficiently bleached grain populations (*106, 107*), contaminant grains associated with syn- or post-depositional mixing (*108, 109*), and aberrant grains displaying inherently unsuitable luminescence properties (*110, 111*).

Sample collection and preparation. Owing to the consolidated nature of the target sedimentary horizons, the 2019 luminescence dating samples were carefully hand-collected from cleaned faces at night with the aid of filtered red LED lighting. Following extraction, the samples were immediately wrapped in black opaque bags and secured using duct tape to prevent light

exposure during transportation and storage. Bulk sediment samples were also collected from the surrounding few cm of each luminescence sample position for beta dose rate determination and water content analysis.

Quartz (212-250 μm diameter) grains were extracted from the luminescence samples under safe light (dim red LED) conditions at the PELL facility and prepared for burial dose estimation using standard procedures (*112*). The sediment samples were initially sieved to isolate the fine sand fraction (90-300 μm). Organics and carbonates were then eliminated using concentrated (30%) hydrogen peroxide (H_2O_2) and hydrochloric (HCl) acid digestion. Quartz grains were isolated using heavy liquid (LST lithium heteropolytungstate) density ranges of 2.62 g/cm^3 to 2.72 g/cm^3. The 212-250 μm quartz fractions were then sieved and etched with hydrofluoric (HF) acid to remove the alpha-irradiated external layers (48% HF digestion for 40 min). The etched grains were subsequently washed in 30% hydrochloric acid to remove any precipitated fluorides and re-sieved using a 90 μm sieve to eliminate any disaggregated grains.

Dose rate determination. The environmental dose rates for the 2019 OSL samples have been calculated using a combination of *in situ* field gamma spectrometry and low-level beta counting. Gamma dose rates were determined from *in situ* measurements made using a Canberra NaI:Tl detector to account for any spatial heterogeneity in the surrounding (~30-50 cm diameter) gamma radiation field of each sample. The 'energy windows' approach described in ref. *113* was used to derive individual estimates of U, Th and K concentrations from the field gamma-ray spectra. External beta dose rates were determined from measurements made using a Risø GM-25-5 beta counter (*114*) on dried and homogenized, bulk sediments collected directly from the OSL sampling positions. This approach was used to ensure that beta dose rates were derived from sample sizes that more closely approximate the very short (~2-3 mm) beta particle radiation fields affecting these samples. Background-subtracted count rates were measured for three aliquots of each sample and compared with net count rates obtained simultaneously for a loess sediment standard with known U, Th and K concentrations (*115*). Final beta dose rate estimates were calculated after making allowance for beta dose attenuation due to grain-size effects and HF etching (*116*).

Cosmic-ray dose rates were determined using the approach described in ref *96*, after taking into consideration site altitude, geomagnetic latitude, and density / thickness of sediment overburden. The effects of bedrock shielding associated with the rock shelter have additionally been incorporated into the cosmic dose rate calculation using the integrated $\cos^2 \phi$-zenith angular dependence procedures outlined in refs *117 & 118*. A time-averaged bedrock attenuation adjustment was made based on the present-day rock shelter configuration (using zenith and azimuth angle bedrock coverage and thickness) and the inferred rock shelter dimensions at the time that each sediment layer was deposited (as determined from detailed geomorphic and sedimentological evidence, including former dripline positions), assuming linear retreat of the rock shelter threshold position over time.

A small, assumed internal (alpha plus beta) dose rate of 0.03 ± 0.01 Gy / ka has been included in the final dose rate calculations based on published ^{238}U and ^{232}Th measurements for etched quartz grains from a range of locations (*119-123*) and an alpha efficiency factor (*a*-value) of 0.04 ± 0.01 (*124, 125*).

Radionuclide concentrations and specific activities have been converted to dose rates using the conversion factors given in ref. *92*, making allowance for beta-dose attenuation (*116, 126*) and long-term sediment water contents (*127, 128*). The present-day sediment water contents of the 2019 luminescence dating samples were uncharacteristically low for this type of depositional

setting (ranging between 1.7 and 2.7% of dry sediment weight), and are not considered to be representative of moisture conditions prevailing throughout the burial period because the sediment exposures had partially dried out prior to sampling. To determine more suitable long-term sediment moisture contents for the 2019 samples, we have used 50% of their present-day saturated water contents based on proportional saturation water content assessments made on fresh exposures of analogous deposits in the immediate site surroundings. A relative uncertainty of 25% (1σ) has been assigned to the long-term moisture estimates of all four samples to accommodate any minor variations in hydrologic conditions during burial. This approach yielded long-term sediment moisture contents ranging between 9.2 ± 4.6% and 12.3 ± 6.1% for the 2019 luminescence dating samples at 2σ (average = 10.2 ± 5.1%), which are consistent with the long-term average water content adopted for the 2014–2015 luminescence dating samples.

D_e determination. Single-grain D_e measurements were made using Risø TL-DA-20 readers equipped with blue LED units (470 nm, maximum power of 92 mW/cm^2), infrared LED arrays (peak emission 850 nm, maximum power of 349 mW/cm^2), and 10 mW Nd:YVO_4 single-grain laser attachments emitting at 532 nm (maximum power of ~50 W/cm^2). Ultraviolet OSL signals were detected using Electron Tubes PDM 9107B photomultiplier tubes fitted with 7.5 mm-thick Hoya U-340 filters. Samples were irradiated with mounted ^{90}Sr/^{90}Y beta sources that had been calibrated to administer known doses to multiple-grain aliquots and single-grain discs. For single-grain measurements, spatial variations in the beta dose rate across the disc plane were taken into account by undertaking hole-specific calibrations using gamma-irradiated quartz. Purified quartz grains with a diameter of 212-250 μm were manually loaded onto aluminum discs drilled with a 10 x 10 array of 300 μm diameter holes to ensure true single-grain resolution during D_e evaluation (*129*).

For the 2019 samples, individual D_e values have been determined using the SAR procedure shown in Table S6, which yielded suitable multiple-grain aliquot and single-grain dose-recovery test results for sample MAN19-4 (see below). Sensitivity-corrected dose-response curves were constructed using the first 0.08 s of each OSL stimulation after subtracting a mean background count obtained from the last 0.25 s of the signal. Between 2100 and 2300 single-grain D_e measurements were made for each sample (Table S7), with individual D_e values being included in the final age calculation if they satisfied a series of standard and widely tested quality-assurance criteria (*130*). Specifically, single-grain OSL D_e estimates were rejected from further consideration if they exhibited one or more of the following properties: (i) weak OSL signals (i.e., the net intensity of the natural test-dose signal (T_n) was less than three times the standard deviation of the late-light background signal); (ii) poor recycling ratios (i.e., the ratios of sensitivity-corrected luminescence responses (L_x/T_x) for two identical regenerative doses were not consistent with unity at 2σ); (iii) high levels of signal recuperation / charge transfer between SAR cycles (i.e., the sensitivity-corrected luminescence response of the 0 Gy regenerative dose point amounted to >5% of the sensitivity-corrected natural signal response (L_n/T_n) at 2σ); (iv) anomalous dose-response curves (i.e., those displaying a zero or negative response with increasing dose) or dose-response curves displaying very scattered L_x/T_x values (i.e., those that could not be successfully fitted with the Monte Carlo procedure and, hence, did not yield finite D_e values and uncertainty ranges); (v) saturated or non-intersecting natural OSL signals (i.e., L_n/T_n values equal to, or greater than, the I_{max} saturation limit of the dose-response curve at 2σ); (vi) extrapolated natural signals (i.e. L_n/T_n values lying more than 2σ beyond the L_x/T_x value of the largest regenerative-dose administered in the SAR procedure); (vii) contamination by feldspar grains or inclusions (i.e., the ratio of the L_x/T_x values obtained for two identical

regenerative doses measured with and without prior IR stimulation (OSL IR depletion ratio; ref. *102*) was less than unity at 2σ). The OSL grain classification statistics obtained for each sample after applying these SAR quality assurance criteria are summarized in Table S7.

Individual and sample-averaged D_e estimates are presented throughout this study with their 1σ uncertainties, which are derived from three sources of uncertainty: (i) a random uncertainty term arising from photon counting statistics for each OSL measurement, calculated using Eq. 3 of ref. *131*; (ii) an empirically determined instrument reproducibility uncertainty of either 1.5% or 1.6% for each single-grain measurement, calculated specifically for the Risø readers used in this study according to the approach outlined in ref. *121*; and (iii) a dose-response curve fitting uncertainty determined using 1000 iterations of the Monte Carlo method described by ref. *132* and implemented in Analyst v4.

Fig. S16 shows representative OSL decay and dose response curves for individual grains that passed the SAR quality assurance criteria and were used for dating. The majority of accepted quartz grains display rapidly decaying OSL curves (reaching background levels within 0.5 s), which are characteristic of quartz signals dominated by the most readily bleachable (so-called 'fast') OSL component (Fig. S16 – compare OSL decay curve shape for a fast-dominated Risø calibration quartz grain; ref. *133*). The single-grain OSL dose-response curves are generally well-represented by a single saturating exponential function. On average, 30% of accepted grains per sample display moderately bright T_n (20 Gy) OSL signals of 100-1000 cts/0.08 s (Fig. S16a), and 5% of accepted grains per sample have relatively bright T_n OSL signals of >1000 cts/0.08 s (Fig. S16b). 65% of accepted grains have relatively dim T_n signal intensities of <100 cts/0.08 s (Fig. S16c), while samples MAN19-3 and MAN19-5 also contains a small number (<1%) of very bright accepted grains displaying T_n OSL signal intensities >10,000 cts/0.08 s (Fig. S16d). The average T_n OSL signal intensities of grains that passed the SAR quality assurance criteria is 400 cts/0.08 s for the four samples.

SAR validation test results. The suitability of the SAR D_e determination procedure (Table S6) was evaluated by undertaking a series of multiple-grain aliquot and single-grain dose-recovery tests on sample MAN19-4. Multiple-grain aliquot dose-recovery tests were first used to ascertain optimal preheating conditions for bulk grain populations. These tests were performed on ~180-grain aliquots using a series of different regenerative dose preheat (PH_1) conditions (ranging between 200 °C for 10 s and 260 °C for 10 s) and a fixed test dose preheat (PH_2) of 200 °C for 10 s, following the successful application of similar preheat combinations in the Mandrin multiple-grain aliquot OSL study. A known laboratory dose of 70 Gy was applied to groups of three aliquots after optically bleaching their natural OSL signals using two 1,000 s blue LED stimulations separated by a 10,000 s pause (to ensure complete decay of any photo-transferred charge in the 110 °C TL trap). The administered dose was treated as a surrogate natural dose and subsequently measured using a multiple-grain version of the SAR sequence shown in Table S6, which involved replacing 125°C green laser stimulations with 125°C blue LED stimulations for 60 s, and inserting a 50°C IR bleach for 40 s prior to each OSL measurement to remove any feldspar signal contamination. Figure S17a summarizes the results of the multiple-grain aliquot dose-recovery tests performed on sample MAN19-4. The most suitable dose-recovery results were obtained using a PH_1 of 240 °C for 10 s and a PH_2 of 200 °C for 10 s. This preheat combination yielded a weighted mean measured-to-given dose ratio of 1.00 ± 0.02, low inter-aliquot D_e scatter, low-dose and high-dose mean recycling ratios in agreement with unity at 1σ (0.99 ± 0.02 and 1.00 ± 0.01, respectively) and a mean recuperation ratio of less than 1%.

To confirm the suitability of this SAR procedure at the single-grain scale, we repeated the dose-recovery test on 1300 individual quartz grains from sample MAN19-4 using the optimum multiple-grain preheat conditions (PH_1 = 240 °C for 10 s, PH_2 = 200 °C for 10 s). A dose of 70 Gy was administered to these quartz grains after bleaching their natural signals using the same procedure described above. 11% of the measured grains (n = 139) satisfied the SAR quality assurance criteria and were included in the final D_e analysis (Table S7). The single-grain OSL dose recovery test yielded a mean measured-to-given dose ratio of 1.00 ± 0.02 and an overdispersion value of 9 ± 2%, confirming the suitability of the chosen preheat combination for this sample (Fig. S17b). These dose-recovery results support the general suitability of the SAR procedure and quality-assurance criteria for single-grain D_e estimation at Mandrin. They also provide a minimum estimate of the intrinsic single-grain D_e scatter and overdispersion that is expected to originate from the laboratory procedures themselves, and from grain-to-grain variations in luminescence responses to the fixed SAR conditions.

D_e results and ages. The single-grain OSL D_e distributions of grains that passed the SAR quality assurance criteria are shown as radial plots in Fig. S18. The final single-grain OSL ages are summarized in Table S8. All four single-grain OSL samples exhibit homogenous D_e distributions characterized by low-to-moderate dose dispersion (relative D_e range = 2.3–3.3), D_e scatter that is reasonably well-represented by the weighted mean value (as indicated by the large proportions of grains lying within the 2σ grey bands), and low overdispersion of 20 ± 2% to 23 ± 2% (Table S9, Fig. S18a-d). These overdispersion values are consistent with those typically obtained for ideal (well-bleached and unmixed) single-grain D_e datasets (e.g., global average overdispersion value of 20 ± 1% reported in ref. *134*, though they are slightly higher than the overdispersion value of 9 ± 2% obtained for the single-grain dose-recovery D_e dataset of MAN19-4. None of the D_e datasets are considered significantly positively skewed according to the weighted skewness test outlined by refs. *135, 136* (Table S9). Application of the maximum log likelihood (L_{max}) test (*108*) indicates that the central age model (CAM) is statistically favored over the three- or four-parameter minimum age models (MAM-3 or MAM-4) of ref. *137* for all four D_e datasets (Table S9).

Collectively, these single-grain OSL D_e characteristics suggest that the Layer C, E and F samples do not suffer from major extrinsic D_e scatter related to insufficient bleaching prior to burial (*138, 139*) or widespread post-depositional sediment mixing between units (*108*) which seems reasonable given that the host sediments were primarily deposited by aeolian processes in a relatively open rock shelter environment and were subsequently rapidly buried (see Supplementary Note 2). It is therefore likely that the low overdispersion observed for these samples is attributable to intrinsic experimental scatter not captured by the dose recovery test (e.g., grain-to-grain variations in luminescence responses due to the fixed SAR conditions; ref. *97* or extrinsic field-related scatter associated with beta-dose spatial heterogeneity (*140*). The single-grain OSL ages for MAN19-3 to MAN19-6 have been obtained using the weighted mean (CAM) D_e estimate, in accordance with their L_{max} test results, as outlined by ref. *107*.

The single-grain OSL ages obtained for the 2019 samples are stratigraphically consistent with each other at 2σ (Table S8), and in agreement with the surrounding multiple-grain OSL ages obtained on the 2014–2015 samples (Table S5), underscoring the compatibility of the two independent luminescence datasets. Layer C has a single-grain OSL age of 52.0 ± 2.9 ka (MAN19-3), while the Neronian Layer (E) is dated to 54.9 ± 3.1 ka (MAN19-4). The two replicate samples collected from Layer F (MAN19-5 and MAN19-6) yield statistically

indistinguishable ages of 60.6 ± 3.5 ka and 61.9 ± 3.7 ka, indicating deposition during mid-late MIS 4 or early MIS 3.

Thermoluminescence dating (Gif-sur-Yvette laboratory). Five flint artifacts (10-15 g each) from the 2014 and 2015 collections were identified as showing macroscopic burn marks. Of these, three passed the heating plateau test, indicating these samples were sufficiently heated in the past to be dated (Fig. S19).

After removing the 3 mm outer part of the flints using a cooled low speed saw, the samples were carefully crushed in an agate mortar and sieved to isolate the 100-160 μm grain fraction. Following washing in HCl (10%), and distilled water, the grains were fixed on stainless-steel discs for TL measurements (*141*). For each sample, four sub-fractions were irradiated with a ^{137}Cs gamma source (*142*) to artificially increase their dose, and TL measurements performed at 5°/s with a homemade reader (*143*). The TL signal centered around 380°C was selected with a UV-blue filter (~380 nm). This additive-dose technique allows determination of the sample paleodose by extrapolation of the dose response curve (fitted through the natural and natural+artificial dose points) to a zero signal.

The calculation of the internal dose-rate (mainly alpha and beta) of the flint samples was based on their U, Th and K concentrations, as determined by ICP-MS/AES of ~ 100 mg fractions. These dosimetric analyses were conducted at the CRP2A laboratory, University Bordeaux-Montaigne (France). At Mandrin, the internal dose rate accounts for 37% (X7381) of the total dose rate on average for the Layer G samples, and 60 ± 10% (X6313, -14) on average for the Layer J samples.

In heterogeneous sediments, the external gamma dose rate received by a given flint artifact is difficult to assess, because the sample is removed from its original burial context during excavation and *in situ* measurement is not possible at each sample's original location. For sample X7381, the external gamma dose has been taken as an average of six dosimeters inserted in Layer G and measured in 1999. For samples X6714 and X6713, the gamma dose rate has been reconstructed, based on the geochemical composition and radioisotope contents of the sediment and calcareous blocks, respectively, and after considering the relative proportional contributions of both fractions and a long-term water content of 12 ± 5% (identical to the present value). The final TL ages (Table S10) are 75.3 ± 3.8 ka (sample X7381) for Layer G, and the two samples from Layer J gave consistent ages at 80.6 ± 3.7 ka (X6713) and 82.7 ± 4.7 ka (X6714).

Bayesian model CQL code

```
Plot()
 {
 Outlier_Model("General",T(5),U(0,4),"t");
 Sequence("Grotte Mandrin sequence")
 {
  Boundary("Start J");
  Phase("J")
  {
   Date("X6713",N(2019-80600,2200))
   {
    Outlier("General", 0.05);
```

```
 };
 Date("X6714",N(2019-82700,2200))
 {
  Outlier("General", 0.05);
 };
};
Boundary("End J/Start I");
Boundary("End I/Start H");
Phase("H")
{
 Date("X6761",N(2015-86500,11300))
 {
  Outlier("General", 0.05);
 };
 Date("X6723",N(2014-85900,3900))
 {
  Outlier("General", 0.05);
 };
};
Boundary("EndH/Start G Ferrassie Mousterian");
Phase("G Ferrassie Mousterian")
{
 Date("X7381",N(2019-75300,1900))
 {
  Outlier("General", 0.05);
 };
 Date("Level G Ferrassie Mousterian");
};
Boundary("F/G");
Phase("F Quina Mousterian")
{
 Date("X6721",N(2014-56700,5200))
 {
  Outlier("General", 0.05);
 };
 Date("MAN19-5",N(2020-60600,1890))
 {
  Outlier("General", 0.05);
 };
 Date("MAN19-6",N(2020-61900,1880))
 {
  Outlier("General", 0.05);
 };
 Date("Level F Quina Mousterian");
};
Boundary("End F to OSL date");
```

```
Date("X6720 base E",N(2014-54600,1900))
{
 Outlier("General", 0.05);
};
Boundary("OSL date to E Niv 6");
Phase("E Niv 6 Neronian")
{
 Date("Neronian E");
 Date("MAN19-4",N(2020-54900,1715))
 {
  Outlier("General", 0.05);
 };
 Combine()
 {
  After()
  {
   Date(calBP(100000));
  };
  Before()
  {
   Date(calBP(49000));
  };
 };
};
Boundary("D Niv 5/E Niv 6");
Phase("D Niv 5")
{
 Date("X6719",N(2014-51600,1500))
 {
  Outlier("General", 0.05);
 };
 Combine()
 {
  After()
  {
   Date(calBP(100000));
  };
  Before()
  {
   Date(calBP(48000));
  };
 };
 Date("Level D Post Neronian 1");
};
Boundary("End of D/Sterile boundary");
Boundary("Start C2 Post Neronian");
```

```
Phase("C2")
{
 R_F14C("OxA-X-2286-14", 0.00485, 0.00108)
 {
  Outlier("General", 0.05);
 };
 Date("MAN19-3",N(2020-52000,1600))
 {
  Outlier("General", 0.05);
 };
};
Boundary("End C2/Start C1");
Phase("C1 PN2")
{
 R_F14C("OxA-X-2286-13", 0.00463, 0.00113)
 {
  Outlier("General", 0.05);
 };
 R_F14C("OxA-21691", 0.00354, 0.00096)
 {
  Outlier("General", 0.25);
 };
 Date("X6718",N(2014-48300,1800))
 {
  Outlier("General", 0.05);
 };
};
Boundary("End C1/Start B3");
Phase("B3 Mousterian PN2")
{
 R_F14C("OxA-22121", 0.00666, 0.00098)
 {
  Outlier("General", 0.05);
 };
};
Boundary("End C1/B3");
Boundary("Start B2");
Phase("B2 Mousterian PN2")
{
 R_F14C("OxA-22120", 0.00448, 0.00102)
 {
  Outlier("General", 0.05);
 };
 R_F14C("OxA-X-2286-10", 0.00832, 0.00101)
 {
  Outlier("General", 0.25);
```

```
      };
      Date("X6717",N(2014-43100,1900))
      {
       Outlier("General", 0.05);
      };
      R_F14C("OxA-21690", 0.0056, 0.00098)
      {
       Outlier("General", 0.25);
      };
     };
     Boundary("End Post-Neronian 2/Start Sterile");
     Boundary("Sterile/B1 Proto-Aurignacian");
     Phase("B1 Proto-Aurignacian")
     {
      R_F14C("OxA-21684", 0.00946, 0.00102)
      {
       Outlier("General", 0.25);
      };
      R_F14C("OxA-2352-51", 0.01651, 0.00138)
      {
       Outlier("General", 0.05);
      };
      R_F14C("OxA-X-2283-11", 0.01259, 0.00105)
      {
       Outlier("General", 0.25);
      };
      R_F14C("OxA-22118", 0.02102, 0.00106)
      {
       Outlier("General", 0.05);
      };
      R_F14C("OxA-X-2286-9", 0.0079, 0.0011)
      {
       Outlier("General", 0.25);
      };
     };
     Boundary("End Proto-Aurignacian");
    };
};
```

Supplementary Note 1. Grotte Mandrin Geographic and Chronostratigraphic Context

Grotte Mandrin is a vaulted rock shelter directly overlooking the middle valley of the Rhône River, one of the largest and most important rivers of Western Europe and the second-most significant freshwater and sediment supplier to the Mediterranean Sea, after the Nile (*144*). The Rhône reaches the current shore of the Mediterranean coastline some 120 km south of the site (Fig. 1). Research conducted since 1990 has allowed the excavation of most of the floor surface from under the vaulted area of the cave. Mandrin provides a reference archaeological succession for it contains all of the phases currently known from the end of the Middle Paleolithic (Layers F to B2; Figs. 2-4 & S5-S6) up to the early Protoaurignacian (Layer B1; Fig. S6b), a culture marking the advent of the full Upper Paleolithic in Western Europe at around 42 ka (*5, 10, 20, 21*). Each archaeological unit has yielded a rich lithic industry (~60,000 lithics) associated with numerous paleontological materials (~70,000 faunal specimens). Faunal remains are almost exclusively related to human activities in the cave, as shown by their high frequency of anthropogenic modifications.

Geoarchaeological study has shown that the overall preservation of the stratigraphic units is good (Layers B to D) to excellent (Layers E-F; Figs. S2-S4). This Pleistocene sequence is covered by recent Holocene sediments (Layer A) recording different phases of human cremations from the late Neolithic (*20*). While Layers B1 to F are known from a large surface of excavation (ranging from 50 to 100 m^2) and concerning most of the area of the cave, the lower part of the sequence, Layers G to J, is only known from ~5 m^2 exposures of different test-pits at the site. The lithic industries from these oldest layers are also rich and allow detailed documentation of these technologies based on 7,687 lithic artifacts. These layers are attributed to Marine Oxygen-Isotope Stage 5 (MIS 5) based on the multiple-grain quartz OSL and flint TL ages obtained, as well as the presence of warm-adapted faunal communities. The bulk of the Pleistocene deposits were formed by sedimentation of windblown local sands and silts entering the cave. Carnivore activity in the shelter is limited to a few traces of wolf and fox activity represented by rare coprolites and gnawing marks on bones initially abandoned by hominins. Layers B to E have yielded several anthropogenic combustion areas.

Supplementary Note 2. Sedimentary History of the Cave and Micromorphology of Layer E.

The sedimentary history of Grotte Mandrin is characterized by major episodes of cornice retreat and back wall disaggregation. The stratified sequence can be classified into three main depositional stages:

-Stage 1: Layers J to G, featuring a large rock shelter opening towards the east instead of the north as it is today.

-Stage 2: Layers F to D, corresponding to a larger opening to the north due to cornice retreat, which allowed the northern Mistral wind to bring large amounts of aeolian sand into the cave from the paleo-Rhône valley below.

-Stage 3: Layer C and especially Layer B, when the retreat of the porch by 5 to 6 m led appreciably to the current configuration and encompassed strong cryoclastism of the roof and walls and ensuing surface reworking and deposition of cryoclasts. In Layer B, these cyroclastic deposits are arranged as two cones: one sloping towards the interior, and the other towards the exterior of the cave.

Layers E and F comprise a cold phase sedimentary deposit characterized by blocks, sometimes larger than the thickness of the layer, surrounded by aeolian sands. This cold phase unit is bracketed by Layers G and D, both of which are characterized by temperate phase signals and contain small cubic blocks. Layers E and F are sealed disconformably by Layer C, of a cold nature, whose hardened matrix protected the underlying layers. F and E are deposits from a single sedimentary environment, bound by a diffuse contact. They were divided into two separate units based on the higher dispersed organic matter content in the fine matrix of Layer E, whereas organic matter is rare in Layer F. Fuliginochronology (*48*) shows that the frequency of occupations is greater in Layer E than in F (an average of ~0.79 occupations per year in F and ~1.10 occupations per year in E), which may explain the higher amounts of charcoal in Layer E.

Throughout the stratigraphic sequence at Mandrin the omnipresence and abundance of fresh, angular roof spall (*47, 145*), together with the lithological homogeneity of the silt-sand fraction and scarcity of clay suggest a single style of sedimentation through time, consisting of a combination of aeolian sand input and *in situ* roof spall, possibly under dry environmental conditions. Layer D seems to represent a massive roof spall episode. There are few cases of Paleolithic cave deposits recording aeolian sedimentation (*146*). At Mandrin, the dry conditions hampered bioturbation and cryoturbation. The state of preservation of the sedimentary deposits is very good, with little to no diagenesis, which affects many Paleolithic cave deposits.

Formation of the Layer E Deposit

A microstratigraphic study of the entire sequence has provided detailed information regarding the formation of Layer E. Four undisturbed sediment samples (MAN-06-2, -3, -4 and -8) were collected from Layer E during the 2006 and 2007 excavation seasons as part of a general microstratigraphic investigation of the Mandrin archaeological sequence.

Sample Preparation and Method

The oriented blocks were oven-dried at 60°C for two days and subsequently impregnated in a mix of polyester resin, styrene and a catalyzer (MEKP) in a 7:3:0.1 ratio at the CERP Institute, CNRS UMR 5198, Tautavel, France. After curing for two weeks, the hardened blocks were cut into 1 cm-thick slabs, which were then shipped to Spectrum Petrographics Inc. (Vancouver, US) for medium sized (7 cm x 5 cm x 30 μm) thin section manufacture. Micromorphological

descriptions follow standard guidelines (*147*). The thin sections were observed with a microfiche viewer at a magnification of about 15 x and with a petrographic microscope at magnifications between 20 and 400 x under plane polarized (PPL) and crossed-polarized (XPL) light. Descriptive criteria are based on standard terminology.

Results

The sediment is predominantly sandy. It is composed of massive, subrounded, moderately sorted (20% medium sand and 40% fine sand) quartz sand (Fig. S2A,C). Besides quartz, there are common sand-sized rounded limestone grains from the bedrock (20%) and minor proportions of burnt and unburnt bone fragments (10%), flint fragments (5%), black particles likely representing char residues (10%) and phosphatic coprolite fragments containing quartz and bone (5%) (Figs. S2-S4). Other rare components of the sand fraction are glauconite grains (2%) and charcoal fragments (2%). There is very little interstitial clay, which is often dusty from the presence of minuscule charcoal and other organic debris (Fig. S4A-C). Overall, the sand grains are loosely packed. The Layer F sediment shows the same lithology as Layer E, with notably lower amounts (<2%) of charcoal, char, burnt bone and dispersed organic dust (Fig S3G).

The basic composition of the Layers F-E sediment, consisting of loose, sandy sediment indicates windblown deposition in a dry environment. A possible source of wind-transported quartz and glauconite sand could be the nearby Miocene marine calcarenites of the floodplain and terraces of the Rhône River, which presently lie at a 100 m altitude below the site, 5 km west. Mandrin rock shelter is a relatively small cavity (12 x 8 m) opening to the north in a very open landscape, hence exposed to the northerly winds, especially to the Mistral, a cool to cold, dry wind that blows from northwestern Europe through the valley of the Rhône River towards the Mediterranean (*148*). This wind is particularly strong in the Rhône River valley.

As for the limestone and bone sand fraction of the sediment, both components were incorporated into the sediment as rounded or subrounded grains. The limestone fragments derived from breakdown of the fossiliferous bedrock, which in fact is composed of sand-sized oolites (Fig. S2D). The rounded bone fragments are most likely associated with the larger bone remains of the Layer E assemblage and derive from penecontemporaneous sandblasting by wind, although given the presence of coprolites, rounding from digestion cannot be ruled out. Nevertheless, the lack of microscopic clay coatings, films, fine bedding, or any other evidence of sheetflow or other water depositional mechanisms indicates that the limestone and bone sand derives from surface rolling and grinding of material accumulated on the sandy paleosurface. The microscopic coprolite fragments, which are also sand-sized, are possibly derived from the same process. They represent carnivore coprolites based on their content of bone and quartz grains (*149*).

Layers F and E sediment is diagenetically stable and exhibits good states of preservation for all of its components. All instances of bone exhibit good states of preservation. Despite the high frequency of phosphatic grains, most of which are coprolite fragments, the sediment from Layer E contains fresh secondary micritic calcite (Fig. S2G) and overall, the calcareous components (bedrock fragments) are fresh and bone is structurally well preserved. Neither other precipitates nor oxidation-reduction features were identified (iron/manganese staining or impregnation). Very few domains of amorphous organic matter around quartz grains were identified randomly throughout the samples (Fig. S2H), possibly derived from degradation of anthropogenic remains. No signs of bioturbation, such as channel porosity, roots, root casts or fecal pellets were identified, excepting sub-recent bioturbation by rootlets towards the top of the layer. However,

the sandy nature of the sediment is not conducive to the preservation of such features, so the possibility of some degree of bioturbation in the past cannot be ruled out. The anthropogenic components are embedded in the sandy sediment throughout a thickness of 5-7 cm, particularly burnt and unburnt bone fragments (Fig. S3). Some of these fragments are vertically positioned, although overall there is no preferential orientation. Similar massive anthropogenic sandy microfacies have been previously described and interpreted as a result of imbedding of anthropogenic debris into an unconsolidated sandy substrate by wind redistribution and trampling, which would bury the small (millimeter) elements lying on the surface (*146, 150*).

This microstratigraphic information, derived from partial sampling of Layers F and E, shows *in situ* deposition of anthropogenic remains and minor diagenetic alteration of the deposit, which indicates that the associated archeological assemblages are found in primary position and may be reliably analyzed from an archaeostratigraphic perspective.

Supplementary Note 3. Technical and Cultural Successions at Grotte Mandrin

Table S11 shows the main technical features of the archaeological layers of Mandrin. All archaeological units are separated by thin sterile layers free of any archaeological material. A total of 59,338 lithics were recovered from all the archaeological layers combined. The lithics are well preserved. The good preservation of the thin edges of the lithic artifacts show rare or no taphonomic movement, in agreement with their rapid covering by aeolian deposits (*26*). Letters A to J refer to sedimentological layers while numbers 1 to 12 refer to archaeological levels as some layers like B have several archaeological levels: B3, B2 and B1.

In the upper part of the Pleistocene sequence eight archaeological units (B1 to F) have been unearthed and divided into five cultural phases (from base to top): 1) Layer F, Rhodanian Quina Mousterian, 2) Layer E, Neronian (*20, 25, 151*), 3) Layer D, Post-Neronian I Mousterian, 4) Layers C2, C1, B3, and B2, Post-Neronian II Mousterian, and 5) Layer B1, Protoaurignacian (*151-153*). These 8 stratified layers encompass ~15 millennia and provided most of the lithic collections of Mandrin with 51,650 artifacts including 13,440 that are ≥2 cm in maximum size (Table S11). The technical features of these lithic industries are easily distinguishable by cultural phases and the lithics below and above the Neronian record clear-cut technical differences:

1) Layer F, Rhodanian Quina Mousterian, provided 1,917 lithics that are ≥2 cm in maximum size. This Mousterian industry is based on flake productions retouched to obtain heavy Quina scrapers (Fig. S5). A total of 138 scrapers were found in Layer F forming 14% of the blanks, the highest proportion from the entire sequence. These proportions of tools are in other layers clustered between 5 and 9%. Quina retouch is only present in Layer F at Mandrin, representing 26% of the scrapers. Some Levallois flakes (n=29) were obtained by preferential methods. Laminar blanks are rare and obtained by classic Levallois flaking, technically well distinct from the blade technologies from overlying Layer E;

2) Layer E, Neronian, provided 2,477 lithics ≥ 2 cm. This industry is focused on the production of blades, bladelets and categories of points (Figs. 2-3, 9) that represent a bit more than 75% of the blanks from this level. The general term ‘point’ strictly refers to a specifically sought after triangular (and pointed) shape of a particular lithic. These points are obtained using technical systems specifically organized around their obtention. It has long been recognized that pointed flakes, Levallois points, and Mousterian points are technologically different (*20*). ‘Points’ must be clearly distinguished from flakes with a pointed morphology, the latter representing one potential (and possibly accidental) by-product of any given system of lithic production. Levallois points, by contrast, are perfectly symmetrical triangular and acute blanks produced only through a specific series of prior blank removals that shape a core to dictate the morphology of the resulting point. Mousterian points are flakes of any technical kind or shape whose morphology is produced by secondary shaping (‘retouching’) that produces the pointed end(s) of the piece. Here the notion and term ‘point’ refers to the strict definition of symmetrical Levallois and Levallois-like points whose shape is the deliberate outcome of flaking technologies geared towards their production. The points found in the Layer E at Grotte Mandrin were obtained from the same cores as the laminar products and were used mainly unretouched or occasionally transformed by thin ventral or direct retouches that resharpened their acute extremity. A total of 882 points (and point fragments), 346 blades and 415 bladelets were found in Layer E; more than the total number of all Middle Paleolithic Levallois points in Europe. More important, the Neronian points are much more regular, thin and light and present degrees of standardization unknown from any

Middle Paleolithic industries. Besides the Protoaurignacian from Layer B1, attributed to modern humans (*20*), the distribution of blades, bladelets and points among the 10 main archaeological layers show that the Neronian industries represent a clear technical anomaly in the Mandrin sequence (Figs. 2-3, S5-S6, S22). While their technologies are radically different, raw materials used in layer F and E are identical, including a noticeable proportion of nonlocal flints coming from the opposite bank of the river. After the Neronian, during the Post-Neronian occupations of the site from layers D to B2 circulations from the western bank of the Rhône are no longer recorded. Fauna exploited from Layers B to F are identical and in the same proportions, layer by layer. This means that the technical particularities of the Neronian cannot be attributed to economic issues (similar raw materials for very distinct technologies between layers F and E) nor to functional facies (categories of hunted fauna for example). The rare points and blades from the other layers of the sequence, from B2 to I, are obtained by very distinct technological processes and represent large and heavy points that share no technical comparisons with the Neronian points. The largest Neronian points are smaller and lighter than the tiniest points from the different Mousterian layers of Mandrin and as many as 30% of Mandrin E points are strictly microlithic, from 10 to 30 mm maximum length. Microlithic points from Mandrin E are made from the same categories of flints as the huge and heavy Quina scrapers from Layer F. Microlithic and standardized points are only known in Mandrin E, where they represent mainly projectiles associated with mechanical propulsion technologies (*27*).

The Neronian shares sharp technical affinities with the Initial Upper Paleolithic (IUP) from the Levantine area (*20*), like those from layers XXV to XX from Ksar Akil, Lebanon (*36-40*). These Levantine IUP industries are focused on similar technical systems to obtain the same points as in the Neronian from Mandrin. The direct analysis of the Ksar Akil IUP show identical technical features as Mandrin E, focused on the production of triangular points showing rare secondary retouches. Technically, these points are like in Mandrin E: a- extracted by direct hard hammer percussion; b- obtained by unipolar convergent flaking; c- point flaking alternates with laminar debitages; d- the beginning of these flakings are initiated by the extraction of crested blades; e- the size and morphology of these points are identical to those from Mandrin (Fig. 9); f- tiny microlithic points of ~30 mm maximum length and below were also sought; and g- functional analyses of these points show that a large part of them were also used as projectiles.

The Initial Upper Paleolithic (IUP) describes the lithic industries of the first Upper Paleolithic levels of the Levantine sites Ksar Akil and Boker Tachtit. Later, it was proposed as a term to embrace any of earliest Upper Paleolithic industries, from China to Spain, irrespective of their technical features (see ref. *61* for recent synthesis). Following this it was proposed to restrict the IUP term to early Upper Paleolithic assemblages, from anywhere in the world, with features of Levallois methods in blank production and essentially Upper Paleolithic retouched tool inventories (*61*), a definition that though it remains generic can be proposed as a definition of the “IUP *sensu lato*”. While this definition allows us to define a large set of the first phase of the Upper Paleolithic in Eurasia, this definition remains technically coarse and not precise enough to define cultural groups or true historical human societies. Concerning Mandrin E, the Neronian lithic industries do not represent here a "IUP *sensu lato*", but rather an IUP *sensu stricto* or Ksar Akil like IUP.

The comparisons between the Neronian and the Levantine IUP can be widened to other aspects than lithic technologies, such as early adornments and symbolic uses of hard animal materials. Some hypotheses propose interpreting the presence of colorants (*154*), feathers (*155-158*), or eagle claws (*159-160*), in archaeological assemblages as indicators of early body adornment and/or symbolic behavior among both *H. sapiens* and Neanderthal groups. However,

in the Eurasian Middle Paleolithic, in spite of very rich archaeological evidence, none of these objects present any indication of deliberate hominin modification; they represent only the collection of natural uncrafted objects. The symbolic interpretation of unmodified raptor claws and feathers has been debated and considered by some as inconclusive (*159, 161-163*). Ochre and other colorants can be related to a large variety of technical activities (*164*), such as the tanning of skins (*165*) and glues (*166*), making their symbolic interpretation speculative.

The Neronian from Mandrin E has provided some worked elements that can be directly linked to the transformation of hard animal materials and possibly the symbolic sphere (Fig. 4): a cut-marked raptor claw (*159*), the distal part of a bone point with lateral notches, a deer canine with lateral scrapping traces, and an ovoid pebble with a deeply engraved line on one side separating the face into two subequal parts. The presence of a cut-marked raptor claw does not have a straightforward symbolic meaning; as underlined in ref. *159*, raptor claws found in the Eurasian Middle Paleolithic show no deliberate anthropic modifications. On the contrary, the deer canine, the bone point, and the pebble are manufactured elements, their structure or their surface being deliberately modified by the craftsmen. The absence of mollusk shells in Mandrin E, while being numerous in the IUP at Ksar Akil, does not allow us to contrast these two industries, seeing that the shells in the IUP, pierced or not, are almost exclusively recognized from coastal sites (*35, 167*). The associations of these manufactured elements (deliberately anthropically modified) from hard animal materials (shown in Fig. 4) that have no clear functional goals are exceptional, or even unique, at such an age in Europe.

3) Layer D, Post-Neronian I Mousterian, provided 1,743 lithics ≥2 cm. Both raw materials and technologies differ from Layer E and F. Whereas in all other Mandrin layers the flints used are mainly local (*20*), coming from 2 to 25 km of the cave, ~50% the distinctive flints used in Mandrin D come from 70 to 90 km north-east of the site. Points and blades make up 3.5% of the Mandrin D assemblage, one of the lowest proportions of all the sequence. These rare points and blades are comparatively thick and irregular in morphology. The technologies involved in their production are not comparable with those of the Neronian. Mandrin D rare points and blades are extracted from classic Levallois cores, both blades and points are respectively obtained from two categories of cores whereas they are extracted from the same cores in the Neronian. The most distinctive trait of this Mandrin D industry is its high proportion of Pseudo-Levallois points. Pseudo-Levallois points generally represent by-products of discoid and Levallois flakes (*153*). They are in Mandrin D specifically produced from the secondary flaking of the ventral surface of flakes (*20*). These very distinctive blanks, numerous in the Post-Neronian I are strictly unknown in the Neronian and represent as many as ~25% of all lithics from Mandrin D. These blanks present a large variability in size and morphologies. Most of the blanks are quite thick at ~10 mm. The Pseudo-Levallois points are interestingly associated with secondary retouch making true truncations of their natural technical back (*20*) (Fig. 3).

4) Layers C2, C1, B3 and B2, Post-Neronian II Mousterian, provided 7,853 lithics ≥2cm. Respectively Layer C2 provided 3,410; Layer C1 provided 1,567; Layer B3 provided 1,653; and Layer B2 provided 1,223 lithics ≥2cm. These four layers, well distinguished by spatial distribution analyses and by their chronologies encompassing ~4 ka, are attributed to the Post-Neronian II Mousterian culture. These 4 Mousterian layers are technically identical to one another, based on the production of flakes mainly obtained by Discoid flaking. These flakes are retouched in a large variety of Mousterian scrapers (Fig. S6a). Altogether, a total of 497 Mousterian scrapers were found dominated by lateral convex scrapers and transversal scrapers.

None of these 497 scrapers present Quina retouch, categories of retouches that concern more than a quarter of the scrapers in Layer F. Some rare points (generally less than 1% of the blanks; Table S11) are attested in these Post-Neronian II layers. They are much larger than the Neronian points and produced from classical Levallois cores that represent distinct technologies than those used to produce the numerous Neronian points. Some Levallois flakes are produced, obtained mainly by recurrent unipolar and preferential methods (Fig. S6a).

5) Layer B1, Protoaurignacian, provided 382 lithics ≥2cm. The Protoaurignacian Layer B1 records the lowest density of archaeological material of all the sequence, with an average of only 8 artifacts by m². Below Layer B1, the lowest density of lithics recorded in the sequence is in B2 with a density 3 times higher than in B1 with 24 artifacts by m². The B1 industry is essentially composed of bladelets and blades, representing more than 90% of all blanks ≥2cm with 247 bladelets and 100 blades. Flaking is unipolar convergent as in other Protoaurignacian industries in Europe (*11, 12*). All the blanks are exclusively produced by soft hammer percussion (using antlers and/or dense vegetal wood) to knap the lithic raw materials. This technique of soft percussion is classic of the Protoaurignacian (*151-153*) and unknown from the rich layers below B1. Blanks, from Layer B2 to I, were obtained by hard percussion employing categories of pebbles to knap the lithic raw materials. Only 13 bladelets are retouched in B1 (Fig. S6b) to produce long and rectilinear Dufour bladelets, a diagnostic tool of the Protoaurignacian, and some pointed bladelets (*153*). The by-products of these laminar productions are rare (12 flakes) as are the cores with only 1 long bladelet core and 8 tiny bladelet cores. Altogether, this small lithic collection, low density of material, rare by-products and cores, low frequency of tiny flakes <2cm (Table S11), make a clear indication that this Protoaurignacian group came to the cave with blades and bladelets that were previously knapped elsewhere and stayed in Mandrin for a very short time. This little lithic collection closes the Pleistocene sequence of the cave. Such Protoaurignacian industries have long been considered as representing one of, if not the very first wave of modern human migration in Europe (*10, 11, 21, 151*). This Protoaurignacian industry is in Mandrin ~10 millennia more recent than the Neronian and separated by 5 geological units recording 5 rich Mousterian layers.

Among the 10 archaeological layers from B2 to I preceding the B1 Protoaurignacian, the Neronian technologies represent a clear technical anomaly that cannot be explained by differing categories of installations or activities. This upper part of the sequence gave the same categories of fauna exploited, in comparable proportions, in every layer. Various layers using the exact same raw materials, and in the same proportions, like Mandrin F and E, show radically distinct technologies. Finally, with 50 lithics per m², Layer E presents the same average density as all other layers that range from 24 to 66 lithics per m². Out of these 8 archaeological layers from the upper part of the Mandrin sequence (B1 to F), the 5 technically distinct industries recognized likely represent different cultural traditions where modern humans (Layers E and B1) alternate with Neanderthals (Layers F, D, C and probably B). These 5 clear-cut technical differences along the stratigraphy are also a demonstration of the very good taphonomic preservation of this sequence, the cave being regularly infilled by aeolian sands. Out of 59,338 lithics, there is for example not a single artifact in Layer E that could be technically interpreted as removed from the surrounding layers D and F, like there is not a single Neronian point in F or D, even though the lithics of layers D, E and F are technically easily recognizable.

On the origins of the Neronian

In 2004 a plausible local origin for the Neronian was proposed (*151*). This hypothesis was abandoned in 2017 (*22*). The original hypothesis of 2004 was precisely quantified and represented at that time the most parsimonious interpretation. Figures S7-S10 present four of the numerous indicators used to evaluate the origin of the Neronian at that time. All data are extracted from ref. *151*. We review here why it was decided, at that stage, to abandon the hypothesis in more recent studies (*20, 22*).

Various indicators were also tested in the studies made in the early 2000's (*151*), all showing a gradual evolution from the local Quina Mousterian from Néron layers III and II to the Neronian layer I. At that time the local origin hypothesis was the most parsimonious theory. However, in 2017, Slimak proposed to abandon his own hypothesis because these apparently gradual technical transformations, from the Quina to the Neronian, were only visible in Grotte de Néron, in the 1950 collections from Jean Combier and Max Veyrier (*22*). In the last decade excavations not in Néron, but in Mandrin's Layer F, of a pristine layer of Rhodanian Quina Mousterian, revealed a rich and very homogenous lithic collection, technically strictly identical with those of Néron III and II. Surprisingly, these very well-preserved collections from Mandrin F did not provide any of the indicators of potential evolution seen in Néron layers III and II. The only plausible conclusion then was that the integrity of the Néron collections, excavated in 1950-51, had to be reevaluated. The Néron collections came from only a few square meters, and from an area along the lateral northern wall of the cave. It then appeared as a reasonable conclusion that the Neronian components of the Quina layers from Grotte de Néron came from mixing from the overlying Neronian layer (Néron I). The gradual effects, well visible in all the graphs presented above, being very likely an effect of a gradient of pollution from layer I to layer II and then layer III. This is not the case in Mandrin, where the meticulous excavations conducted over the last 30 years and on Mandrin Layer F in the last 15 years revealed that there is absolutely no mixing between Layers F and E, a fact also attested by the geological study that gives evidence of the integrity of the layers.

The Mandrin F excavations these last years provided a rich and very well-preserved lithic industry of about 3000 lithics, providing the richest collection of the Rhodanian Quina industry, and, more importantly, the only collection obtained with the state-of-the-art methods of field archaeology. The recovery at Mandrin of rich new data, with lithic industries showing precise technical peculiarities and the absence of blades, bladelets and points, were the demonstration that the Grotte de Néron presumably presented serious stratigraphic problems. Finally, these results obtained from the field of lithic technology agreed with new data we reached from the other scientific approaches, from the radiometry and from the micro-chronology of Mandrin F (Quina) *vs* Mandrin E (Neronian) for example. These data were documenting a very short time, likely less than 1 year, between the Quina and the Neronian, making impossible any technical continuity from the Quina traditions to the Neronian. Thus these 3 distinct scientific approaches provided convergent evidence that a local evolution from the Quina to the Neronian was no longer feasible as a parsimonious interpretation. Based on such evidence, in 2017 Slimak published a paper (*22*) that expressed doubts about the 2004 hypothesis.

Supplementary Note 4. Spatial Distributions within the Archaeological Layers

Spatial distribution in Layers E to B1

The projections of the archaeological material from Grotte Mandrin show high densities of artifacts separated by thin sterile layers with no archaeological material. The north-south projection (Fig. S1B-E) was built using the 3D coordinates from archaeological material of Layers B1 to E. Each archaeological unit has been first tested by histogram frequencies for their altitudes to highlight the statistical densities distribution of material and their precise vertical distributions. The regular slopes of the layers (NW/SE inside the shelter and SW/NE outside the shelter) make impossible a visual Y/Z or a X/Z integrating all the material. This north south projection is realized in the center of the shelter, from the back of the cave, 3.59 meters long (in Y/Z). The projection presented is done on 81 cm width (in X/Z). This central Y/Z projection concerns 585 plotted artifacts from that central area. Fieldwork and all spatial projections and statistical distributions show a clear continuity of all the archaeological layers inside and outside the shelter and a very good preservation of the layers and their archaeological material. This remarkable preservation concerns all the excavated area, inside and outside the shelter.

Spatial distribution of the material directly surrounding the Man12 E 1300 tooth

The Man12 E 1300 modern human tooth was found in square N3 in the northwestern quarter of the excavation (Fig. S1A). A X/Z projection of all the material spatially associated with Man12 E 1300 shows the position of this tooth at the base of Layer E (Fig. S1B, D). This X/Z projection is focused on the 3D plotted archaeological material in direct spatial contact with Man12 E 1300, in squares M-N/3-4. The Man12 E 1300 tooth is directly covered by 207 archaeological remains from Layers B, C, D and E, and itself overlies 378 archaeological remains from Layers F and G, below it. This archaeological material includes 146 fauna remains and 439 lithic elements. The lithic material from Layers B-C, D, E, F and G are very distinct technically and easily recognizable from one another and there is no mix of archaeological material that could be documented in that area, nor in any other part of the excavated surface. The Protoaurignacian Layer B1 does not appear in that projection as this layer is spatially clustered in the eastern and southern part of the site, far from the north-west quarter where Man12 E 1300 was found. An analysis of the distribution of diagnostic lithic elements from Layer E (blades, bladelets and points) demonstrates that the proportion of these diagnostic elements show no statistical difference between the central part of the cave and the area where Man12 E 1300 was found (Fig. S1).

Supplementary Note 5. What is the Initial Upper Paleolithic?

The direct study of the Ksar Akil collections, concentrating on the 1947-1948 excavations, deposited at the Peabody Museum in Cambridge, Massachusetts, took place over three visits from 2016 to 2019, culminating in a bit more than 6 months of analysis on these industries. This research focused on 31 units, levels XXXVI to XIII, ranging from the Middle Paleolithic to the first Upper Paleolithic. A total of 17,809 lithic pieces were analyzed and integrated into a database distinguishing 138 distinct technical and typological categories to account for the main peculiarities of these industries. At the same time, these collections were the subject of a series of photographs, technical drawings, and functional analyses carried out by Laure Metz (UMR LAMPEA). The aim of presenting the elements here is to put the data in Figs. 9 & S21 into qualitative perspective with what has been proposed regarding relations between Europe/Levant, essentially on bibliographic bases, concerning the first moments of the Upper Paleolithic. We focus here on the salient features of the different industries of Ksar Akil simply allowing us to highlight, or exclude, the possible relations that may exist between Europe and the Middle East. The IUP may have emerged in a large geographic area between the Mediterranean Levant and Central Asia (*61*). The use of the term IUP groups together collections from varied origins recognized over a vast territory ranging from North Africa to the highlands of Central Asia. In this sense, the name would therefore encompass quite diverse technical realities. It is necessary to differentiate the generic term IUP, which does not have a precise techno-cultural value (for this statement see the proposals in ref. *61*), from the IUP of Ksar Akil which refers to a very precise technical reality and, because of Ksar Akil's place in the history of research, should be used as a type sequence for the determination of an IUP *sensu stricto*, which can then be compared to a IUP *sensu lato* (a name therefore grouping together a large fraction of the first Upper Paleolithic industries of the Old World with no suggestion of a precise technical or cultural connection). The use of the term IUP hereafter refers to such a IUP *sensu stricto* as it is documented in the Ksar Akil sequence.

Salient features of the technical structures of the IUP of Ksar Akil

The Ksar Akil IUP concerns units XXV to XXI. When exploring the historiography of the research on Ksar Akil, units XX and XIX were also attributed to this first phase of the Upper Paleolithic by Father Ewing in 1947 (*168*) and then by Azoury and Hodson in 1973 (*169*). A rich body of literature on these IUP and EUP industries, including numerous illustrations, can be found in the syntheses by Azoury (*33*) or Ohnuma (*170*).

In the 1947-1948 Harvard collections, our recent analyses counted 4231 lithic pieces from units XXV to XXI. These industries are essentially made up of laminar production, blades and bladelets, corresponding to the first phases in the process of obtaining Levallois-type points. These units include 677 points and micropoints (*sensu* Levallois and generally unretouched) versus 1226 blades and bladelets.

The debitages are initiated by a single or double sloped crest (84 blades and ridge bladelets of different categories are attested), the extraction of which is followed by a laminar phase directed towards the extraction of typologically Levallois points. These debitages are strictly unipolar convergent. No points with opposite negatives are recorded in these units. The geometry of the cores is commonly pyramidal, linked to a semi-rotating exploitation of the blocks. The extraction of technically highly invested points is inserted between these laminar phases, ensuring the classic predetermined character of Levallois debitage, but here associated with cores whose geometry and volumes do not, in any way, coincide with the classic definition

of Levallois debitage (*152*). Only the notion of predetermination then recalls, or rather a form of technical continuity with, the classic productions of the Middle Paleolithic.

Small-sized points and micropoints *sensu stricto*, are well represented in these units representing 23-40% of all points. Their maximum dimensions are on average around 30 mm. Analysis of the last removal from the micropoints cores shows that a large fraction of the smallest points- with widths between 30 mm and 10 mm- are underrepresented in the collections compared to their original proportion in these technical systems. In the meantime, the collection also shows a rarity of microflakes among these units. We count among that collection only 1 microflake of less than 2cm of maximal length out of these 4231 lithic elements. That rarity of little flakes and a too low representation of micropoints of less than 30 mm (compared to the high representation of micropoints cores (273 micropoint cores for 200 micropoints) likely was caused by the excavation methods employed at the time.

The techniques are based exclusively on direct hard stone percussion. The vast majority of these points have a finely faceted butt. The points are rarely retouched and, in general, typological tools occupy a relatively discreet place in these units.

The IUP from Mandrin E does not only fit with the Levantine IUP in terms of the technology and morphology of its small points. The entire technical system that is virtually identical, including the production phases of the larger points and the blades and bladelets.

Some very precise and technically highly invested technical solutions like the “schéma croisé” characterize both the Ksar Akil and Mandrin IUP industries. The “schéma croisé” was first defined in 2004 (*151*) and is one of the more culturally invested technical solutions found in the Neronian. This technical solution allows the obtention of points from a blank (flake or blade) with the goal that these points (or micropoints) have one of their lateral edges (generally the left side) composed of the ventral surface of the core/flake. To do so, the craftsman needs to pass through several technical phases that will allow the extraction of a perfectly symmetric point that possesses one of its lateral flanks composed of the positive surface (the ventral surface) from the core/flake. This is one of the most culturally and technically invested schéma opératoire one can document. The “schémas croisés” are part of the IUP technologies of both Ksar Akil and Mandrin E (Fig. S21). There is low probability that the exact same technical traditions with their culturally highly invested solutions would appear on both sides of the Mediterranean Sea in roughly the same chronology purely randomly.

Linking the Levantine IUP sensu stricto and the Neronian Rhodanian IUP

The Neronian thus technically represents a perfect decal of the Ksar Akil IUP. The technical systems, the production objectives, the morphology, and even the morphometry of the sought-after points are strictly identical. In parallel, the function of the points, determined via functional analysis, shows that the points of Ksar Akil XXV-XXI and those of Mandrin E fall strictly within the same functional categories (*27*, *171*). In both cases, they are mainly weapons correlated with the development of mechanical propulsion systems -spearthrower and/or bow and arrow. Through measurements with millimetric precision, morphometric width/thickness analysis of these points shows that no differentiation can be made between Neronian and IUP points (Fig. 9). While TCSA is a simple morphometric index based on width/thickness ratio, the identity of this index in between Mandrin E and Ksar Akil XXV-XX can have several explanations as strictly morphological convergences can result of ballistic realities; the use of bow and arrow in both IUP sequences for example. However, a bow can propel very tiny or far larger points and showing distinct TCSA values (*27*). More important, the TCSA is simply here used as a morphological index and these morphological identities affect points for which no distinction can be made here

between the precise technical systems put in place to obtain them, even though they are located at both ends of the Mediterranean. A parsimonious interpretation is that their strict connection, associated with the exact same technical choices and solutions, have all chance to be of cultural value.

Although radiometric approaches in the Levant still provide disputable results, there is every reason to believe that the beginnings of the Levantine IUP should be roughly contemporary with the Neronian of Mandrin. These data allow us to deduce that the two cultural groups, the Levantine IUP *sensu stricto* (as recognized in Ksar Akil) and the Neronian, actually are one. It is important to note that radiometric dating of Ksar Akil's IUP is affected by collagen preservation issues that alter certainly most if not all IUP Levantine sites, resulting in several clearly divergent chronological models. The data presented here would be rather compatible with the model proposed by Bosch (*30, 59-60*) who concludes that the radiometric dates obtained from the IUP represent minimum ages. The actual age of the beginnings of the IUP at Ksar Akil is still unknown, but based on the technological features discussed above being present in layer XXII of Ksar Akil, and beginning as early as layer XXV, the IUP *sensu stricto* began here well before the 46th millennium. If we widen the focus to other levels, the presence of shells for example, numerous at Ksar Akil but absent in Mandrin E, does not allow us to individualize the Neronian from the IUP, seeing that the mollusk shells in the IUP, pierced or not, are almost exclusively recognized at coastal and near coastal sites (*35, 167*).

It is important to underline that the ornaments from Bacho Kiro and the Levantine IUP are well differentiated, with the presence of perforated shells in the Levant absent from Bacho Kiro where pierced teeth are employed (*13*). And it is true that these two categories of ornaments represent particularly distinct solutions. However, the presence or absence of shells may not necessarily represent a true distinction between the Neronian IUP and the Levantine IUP. If the presence of shells is numerous at Ksar Akil or Üçağızlı, it has been largely underlined that the shells of mollusks in the IUP, pierced or not, are in fact characteristic of coastal sites (*35, 167*). In their recent synthesis Kadowaki et al. underline "*There is currently no clear record of marine shells from inland areas in the IUP. A candidate is "a possible marine shell bead" mentioned in a report of Mughr el-Hamamah that yielded radiocarbon dates and lithic assemblages corresponding to an early phase of the UP (Stutz et al. 2015). The site is located in northwest Jordan, more than 80 km from the Mediterranean coast*".

In non-coastal sites, and for all the Eurasian IUP, it has been reported only 1 fragment of *Pecten* shell in Tor Fawaz sequence (Jordan; ref. *167*). However, it is unsure if this *Pecten* comes from the red sea (located 55 km south) or from the Mediterranean Sea (if this shell was a *Pecten* sp. cf. *jacobaeus*, it would come from 188 km away). This potential IUP shell inland remains isolated and ambiguous in terms of interpretations (this shell presents no evidence of modification to use it as a bead). We should then underline following ref. *167* that out of this isolated and unclear occurrence, there is not a single IUP site far from the coast (more than 55 km) that has provided shell beads. This global context of the IUP remains true for IUP layers providing a very rich archeological material like in Umm El Tlel sequence (Syria) for example. Shells are no more attested in more eastern IUP sequences of Northern and Central Asia.

Mandrin is more than 100 km from the current Mediterranean coast and presents a similar context as Levantine non-coastal sites where shells beads are not attested. Finally, the transformation of categories of bones or teeth to produce objects of symbolic value, while very distinct between Bacho Kiro and the Levantine IUP, is also well attested in the Neronian and some of them are presented in this paper including bone point with lateral notches or modified deer canine. These elements strongly distinguish the Neronian from the preceding and succeeding

Mousterian layers in the Grotte Mandrin sequence. Among the IUP, the divergence between Bacho Kiro and Levantine ornaments suggest that among this early phase of the IUP the production of manufactured objects of symbolic value may be constrained by the locally available material (presence/absence of shells for example) and/or by local (in time and space) traditions. It is noteworthy that these singularities from the symbolic sphere and in the ways to express them do not affect the precise technical unity of the lithics traditions in the first phases of the IUP.

The Üçağızlı site in the Turkish Hatay could also provide a second comparative site to Mandrin E IUP, and likely the best one after Ksar Akil. The many studies directed by Steve Kuhn precisely underline very close technical relations or even technical identities between the IUP industries of Ksar Akil and Üçağızlı (*62, 172-173*). Various key elements coming from Üçağızlı are also of great interest and can also highlight the oldest phases of the IUP like the fact that in Üçağızlı "*Interestingly, the frequency of burins is actually inversely correlated with that of bone tools, in that burins are common only in the lowest layers where bone/antler artifacts are rare. Preliminary micro-wear results suggest that burins from the lower levels were indeed used to work materials other than bone or antler, most notably hides*" (*172*). These data underline that in the early phases of the IUP bone tools are rare, but not absent, and like in Mandrin E, the early phases of the IUP of Üçağızlı show high representations of burins. The highest representation of burins in the beginning of the IUP of Üçağızlı is layer H where those tools represent almost 20% of all tools, compared with Mandrin where these UP categories of tools represent more than 27% of all tools. That correlation between burins and the earliest phases of the IUP fits particularly well with the early chronology of the IUP in Grotte Mandrin. This also opens various topics that go far beyond the scope of this paper like the fact that a part of these burins found in the earliest phases of the IUP may be in fact (at least for a part of them) bladelets and micropoints cores. This leads to questions on the technical structure of the beginning of the IUP and the place, in the technical system of these tiny and light micropoints, that should be an important technical particularity defining the earliest phases of the IUP *sensu stricto*.

Supplementary Note 6. Hominin Specimens from Grotte Mandrin

We describe below the Late Pleistocene hominin remains from Grotte Mandrin's Layers C to G (see also Table 1).

Human remains from Layer C

Man02 C 983 (LRM3). This is an isolated permanent lower right third molar (LRM3) preserving the complete crown and root. The crown exhibits advanced wear, with the metaconid and the buccal cusps being flattened and large patches of connecting dentine outcropping at the occlusal level (stage 6 of ref. *174*). No occlusal morphological feature is left, even if the position of the five main cusps is still recognizable. A large mesial ICF is present, but no distal one is visible. At the enamel-dentine junction (EDJ) level, the microtomographic (µCT) record shows that the only remaining intact dentine horn of the entoconid is low. A faintly expressed crest running from the entoconid toward the occlusal basin is visible. The protostylid is expressed as a deep groove separating the protoconid and hypoconid, with two crest-like features running down vertically from the protoconid and from the hypoconid and ending at the base of the cusps (*175*). The root displays three branches, the two buccal branches being fused together and the mesiolingual branch bifurcating at mid-root, giving a C-like shape section in the cervical half of the root. The branches are separated by a deep lingual groove starting only at mid-root height, resulting in a taurodont morphology (see also Table S19). Taurodontism, and in particular hypertaurodontism, is commonly found in Neanderthals and is less frequent in Pleistocene and recent humans (*82*). The pulp cavity is partially filled by secondary dentine deposits, reducing its volume and affecting the shape of the pulp chamber and canals.

Man11 C 204 (LLdm2). This is an isolated deciduous lower left second molar (LLdm2) crown with only 0.5 to 5 mm of the root preserved. Occlusal wear is very advanced, with large patches of dentine linking all the cusps except the metaconid that only shows a smaller dentine island (stage 6 of ref. *174*). Apart from the remnant of the anterior fovea, no occlusal feature is discernible anymore at the external level. A large ICF occupying most of the mesial aspect is visible, while the enamel in the occlusal-most portion of the distal aspect is chipped, preventing from assessing the possible presence/absence of a small distal ICF. The deep and mesiodistally compressed anterior fovea is well expressed at the EDJ level, enclosed by the low but uninterrupted mesial marginal ridge and mid-trigonid crest. Remnants of crests are also visible in the talonid, with a crest running down the hypoconid toward the center of the occlusal basin and a bifurcated crest similarly lying on the entoconid. On the buccal aspect of the EDJ, a vertical crest-like feature runs down from the protoconid and ends at the cusp base. The pulp chamber is filled with sediment and secondary dentine deposits are discernible on the microCT record.

Human remains from Layer D

Man04 D 395 (URdm2). This is a deciduous upper right second molar (URdm2) crown with the root broken immediately below distally and preserving between 1 and 3 mm of the root on the other aspects. The occlusal wear is advanced, with large dentine patches linking the four main cusps and a flattened occlusal surface (stage 6 of ref. *174*). Only traces of the grooves on each side of the oblique crest remain on the occlusal surface. Large mesial and distal ICF are present. At the EDJ level, the oblique crest is high and uninterrupted. A Carabelli trait expressed as a fossa enclosed by a low crest is visible mesially to the protocone. The pulp chamber displays four well-expressed horns corresponding to the cusps. It is noteworthy that there is a twinned paracone

pulp horn while the pulp horns of the other cusps are single. If the pulp chamber shape reflects the original EDJ shape, then it suggests the presence of a twinned dentine horn, as it has been recently observed in nine Neanderthal upper molars (*176*), but not recorded in modern human molars so far.

Man04 D 679 (URdm2). This deciduous upper right second molar (URdm2) crown preserves the root broken immediately below distally and between 1 and 3 mm of the root on the other aspects. The occlusal wear is advanced, with large dentine patches linking the paracone, protocone and metacone, and a dentine island visible on the hypocone (stage 6 of ref. *174*). The occlusal surface is flattened. Only traces of the grooves on each side of the oblique crest remain on the occlusal surface. Large mesial and distal ICF are present. At the EDJ level, the oblique crest is high and uninterrupted. A Carabelli trait expressed as a fossa enclosed by a low and buccally interrupted crest is visible mesially to the protocone. The pulp chamber displays four well-expressed and single horns corresponding to the four cusps.

Man03 D 2734. This buccal or lingual fragment of a post-canine tooth preserves an almost complete cusp and half of a second cusp and between 1 and 4 mm of the root. The occlusal wear degree is low or absent, but the smoothed external surface of the enamel likely due to taphonomic alterations prevents recording the eventual presence of small wear facet(s). The cervical margin shows a small enamel extension. The EDJ shows a higher (likely mesial) and a lower (likely distal) dentine horn. A crest runs from the lower dentine horn in the occlusal basin. Remnants of two pulp horns are distinguishable. The preserved morphology suggests that it could represent a buccal fragment of a lower deciduous or permanent molar.

Human remains from Layer E

Man12 E 1300 (URdm2). This represents a deciduous upper second molar (URdm2) crown with a 3 mm-long portion of the root on the lingual and distal aspects. The specimen is broken longitudinally in a mesiodistal axis along the external part of the buccal marginal ridge and a part of the paracone is missing. Only small patches of enamel remain on the crown and the dentine is smoothed, the dentine horns and crests being lowered and rounded, likely due to taphonomic alterations. In its present state of preservation, it is not possible to assess the presence/absence of occlusal wear. The root gets thinner toward the apical part, either since it was still growing or because it was at an advanced resorption stage. Three of the main pulp horns are well visible, while that of the paracone is broken.

Human remains from Layer F

Man98 F 811 (LLM1). This permanent lower left first molar (LLM1) preserves its crown (apart from a chip of enamel at the distobuccal corner) and most of the root (the apex of the branches being broken). Occlusal wear is moderate, with small dentine islands on the protoconid, metaconid and hypoconid, and a narrow band of dentine linking the entoconid to the hypoconulid (stage 3 of ref. *176*). No occlusal feature is preserved externally. At the dentine level, a low but uninterrupted mid-trigonid crest is visible, delineating a large anterior fovea. An almost uninterrupted crest runs from the metaconid to the hypoconid (type 6 of ref. *175*). This type of talonid crest pattern is recorded in Neanderthal molars but not reported so far in modern humans (*177*). Shorter crests are running from the hypoconid and hypoconulid toward the middle of the occlusal basin. The root, slightly eroded externally, shows a single root stem for c. 4.5 mm below the crown, before plate-like mesial and distal branches diverge, exhibiting clear taurodont morphology. The pulp cavity is partially filled with secondary dentine, but five horns are still

visible on top of the pulp chamber and three root canals are distinguished, two mesial and one distal.

Human remains from Layer G

Man15 G 2851 (LRdm1). This deciduous lower right first molar (LRdm1) preserves the lingual two-thirds of the crown and the roots are broken below the crown. The occlusal surface is moderately worn, with large areas of dentine exposure still visible on the three broken buccal cusps and smaller patches on the two lingual ones (stage 4 of ref. *174*). The anterior fovea is well delimited by the mesial marginal ridge anteriorly and by a high and thick complete mid-trigonid crest distally. At the dentine level, a small tuberculum intermedium lies at the distal end of the postmetacristid. This feature, even if located in an unworn area of the crown, is barely visible at the outer enamel surface, detectable as a small relief on the crest. The pulp chamber is broken and damaged, only the position of the two lingual horns remains visible.

Man15 G 2852. Preserving only a small portion of the crown, this fragment likely represents a piece of deciduous maxillary or mandibular molar, but no diagnostic feature enables any secure attribution. A faint vertical digitation in the mesial part could suggest that it is either a buccal fragment of a deciduous lower right molar or a lingual portion of a deciduous upper left molar. Occlusal wear is likely moderate to advanced as the preserved occlusal part of the cusps shows mesiodistally extended dentine exposure. The broken and damaged surface of the pulp chamber shows two to three pulp horns.

Supplementary Note 7. Proteomic Analysis of Hominin Specimens from Grotte Mandrin

Proteomes were recovered from nine Grotte Mandrin specimens (1265, 2583, 1275, 3299, 1597, 2855b, 2854, 1587b, and 1596) confirmed by ZooMS (*178,179*) as deriving from hominin skeletal material to attempt to retrieve the COLX signatures reportedly capable of distinguishing between anatomically modern human, Neanderthal and Denisovan (*17*). All were treated with 0.6 M hydrochloric acid (HCl) overnight (~18 hours), centrifuged at 12,400 rpm, and the supernatant removed. The acid-insoluble residue was then incubated with 6 M guanidine hydrochloride (GuHCl) overnight prior to being ultrafiltered into ammonium bicarbonate (ABC). In each case, reduction was carried out with 100 mM dithiothreitol in 50 mM ABC (4.2 µL in 100 µL sample) at 60 ºC for 10 minutes, allowed to cool, and acetylated with 100 mM iodoacetamide (8.4 µL in 100 µL sample) in the dark at room temperature for 45 minutes. The samples were further quenched with the same amount of DTT prior to digestion with 2 µg sequencing grade trypsin (Promega, UK) overnight (~18 hours) at 37 ºC.

Sample digests (including one blank that included HCl, GuHCl and ABC) were then purified with C18 Solid Phase Extraction clean-up and dried to completion in a centrifugal evaporator prior to resuspension with 5% ACN + 0.1% formic acid (FA) and then analyzed using LC-MS/MS (Waters nanoAcquity UPLC system coupled to a Thermo Scientific Orbitrap Elite MS) at the Biological Mass Spectrometry Core Research Facility (University of Manchester) similar to methods described in ref. *180*. In brief, samples were concentrated on a 20 mm x 180 µm pre-column prior to being separated on a 1.7 µM Waters nanoAcquity Ethylene Bridged Hybrid (BEH) C18 analytical column of (75 mm × 250 µm i.d.) and fractionation was achieved using a gradient beginning at 99% buffer A/1% buffer B and finishing at 75% buffer A/25% buffer B, whereby buffer A = 0.1% FA in H_2O and buffer B = 0.1% FA in ACN.

Mascot searches were carried out against the public SwissProt database with an added local database containing the COLX sequences for modern human and Neanderthal (*17*), using a tryptic (trypsin/P) search (carbamidomethyl C fixed modification and variable oxidations of M, K and P, deamidation of N/Q, 5 ppm precursor tolerance and 0.5 Da MS/MS tolerance allowing for 1 missed cleavage).

The results indicated that even without the use of an ion score cut-off (such as the peptide homology score of 38), COLX could not be observed in any of the samples (Table S23). As expected, the specimens were dominated by type 1 collagen, and all specimens also yielded peptides observed from types III and V, the two main collagen types that associate with type I collagen (*181,182*). Therefore, distinction between human species was not possible. Given the notable lack of non-collagenous proteins in the specimens from this layer reduces the likelihood of observing the COLX signatures in older specimens from this site.

Supplementary Note 8. Fuliginochronological study of the transition between Layers F and E at Grotte Mandrin

Here we demonstrate thanks to a pioneering method (fuliginochronology; Fig. S23) that the succession between Neanderthals of Layer F and modern humans of Layer E took place in a very short time (~one year) at Grotte Mandrin (Fig. S23, S24).

Soot marks provide invaluable evidence of past human activities, and can sometimes be noticed in carbonated deposits formed in caves and rock shelters. In previous work (*47*) we have demonstrated that these deposits, generally ignored in archaeological studies, turn out to be a perfectly suitable material for micro-chronological studies of hominin occupations in a site. At Grotte Mandrin thousands of clastic fragments from the rock shelter's walls were found in every archaeological layer of the site, some having sooty carbonated deposits on their surface. Microscopic observation of thin and/or polished sections made in the growth axis of these sooty speleothems shows that what might appear as a single black lamina to the naked eye or at low magnification usually resolves into a multitude of thin soot films a few micrometers thick (Fig. S23a). These fuliginous speleothems record human occupations successions, and because the crumbling of the rock shelter's vault and walls doesn't occur everywhere at the same pace, each clast bears a specific sequence of soot films that is documented in measurement tables and represented as barcodes (Fig. S23b). Barcode diagrams represent successions of soot films from oldest (bottom) to youngest (top). Black lines represent soot films, dashed lines represent probable soot films, and the spaces between them correspond to the carbonated deposits that crystallized in the absence of human occupation. The raw data collection is made thanks to software (LnSeq module, DataWald platform, G.L Conception) initially developed for dendrochronology and adapted to our object of study: sooty speleothems. The position of each soot film is recorded from a transect drawn on high magnification photographs of the samples: the origin of the parietal carbonated crust is marked with a red dot, which corresponds to the base of the grey vertical bar on the diagram. Once the entire sequence has been documented, this bar represents the total thickness of the sooty speleothem. The inventoried data are then matched statistically and graphically to reconstruct the chronicle of human occupations at the site from synchronization of the different barcodes obtained on each sample. This matching process is detailed in refs. *48* and *145*.

Soot films combination sequences have been obtained for each layer of Grotte Mandrin. It is important to note that at Grotte Mandrin it is usually impossible to match the individual sequences of soot films documented on clasts from different archaeological layers (except for the fringes of combination sequences from adjacent layers). It is possible to achieve this with samples from the same layer, which indicates a relatively fast rate of wall and vault disintegration and syndepositional accumulation of sooty roofspall throughout the formation of the archaeological deposit (*47*; Figs. S24-S25). The Layer F and E combination sequences have been obtained by matching nine and eight individual sequences, respectively. The two combination sequences overlap at their fringes (Fig. S24), meaning that Layer E contains soot films formed during Layer F times and fallen and deposited during the formation of Layer E. Coupled fuliginochronological and stratigraphic analysis allows to reassign the soot films to the archaeological units corresponding to the time of their formation and thus reconstruct the occupation chronicles both for the Layer F Mousterian group (highlighted in orange in Figs. S24-S25) and the Layer E Neronian group (highlighted in green in Figs. S24-S25).

The thickness of the carbonated deposit that formed between the last Mousterian and the first Neronian occupations is thin, and possibly represents a very short time, meaning that there is no large temporal gap (at a human lifetime scale) between the last Mousterian (Layer F) and first Neronian (Layer E) occupations. In other words, the fuliginochronological study detailed in ref. *47* shows that these two distinctive groups succeeded each other at the site within less than a single human lifetime (*47*).

Research over the past few years allowed to demonstrate the annual nature of the calcite doublets observed in Grotte Mandrin's parietal carbonated crusts (*48*). These doublets (Fig. S23c) are composed of a microsparitic laminae (DCL – Dark Compact Laminae), which are formed during periods of hydric excess, and a micritic laminae (WPL – White Porous Laminae), formed under drier conditions. Micrite/sparite alternation is a seasonal marker related to hydric conditions (*183*). These WPL/DCL doublets are generally annual (Fig. S23e) but not always (*184*). In order to demonstrate that this change in crystalline fabric occurs at an annual scale, it must be synchronized with another seasonal marker that is not solely dependent on hydric conditions, such as variation in the concentration of certain minor or trace elements. According to several studies (see for example: *185-192*) the analysis of high-resolution variations in Sr can be a way to highlight annual cycles. The study of Sr concentration fluctuations in the carbonated crusts of Grotte Mandrin by µLIBS (Laser-Induced Breakdown Spectroscopy) and the comparison of Sr fluctuations with the crystalline fabric alternations (micrite *vs* sparite) thus made it possible to establish the annual character of the WPL/DCL doublets at this site, since the two signals were synchronized (*48, 193*).

Therefore, the joint study of soot films and calcite doublets allows the chronicles to be set on a micro-chronological time scale with annual resolution: the annual calendar of carbonates precipitation (Fig. S23c-f). This joint study can be done from thin section microscopic observations that allow seeing both the soot films and the calcite doublets (Fig. S23c). The indexation of the occupations chronicles is done by recording the position of each soot film in relation to the calcite doublets and shown in Figs. S23 and S25 in blue (dark blue for DCL and light blue for WPL).

We documented the position of the soot films *vis-à-vis* the annual calcite doublets for the critical transition period between Layers F and E. At some locations, carbonates did not form as legible calcite doublets but rather as White Porous Calcite (WCC, dominated by micrite) or as Dark Compact Calcite (DCC, dominated by microsparite) represented in Fig. S25 in two other shades of blue. For locations where there was some uncertainty regarding the exact position of soot films *vis-à-vis* the calcite doublets, a grey bar was added to the calcite doublets drawn in blue. The joint study of soot films and calcite doublets is done on each sample and the indexed chronicles reflect a synthesis of data for each layer. Layers F and E occupations chronicle indexing was therefore made by matching of Layers F and E combination sequences. Confident information (without grey bar) is privileged (the grey bar is therefore removed) and the remaining uncertainties are reported on the chronicle (grey bar is conserved). The indexed chronicle of occupations shows reliably that a single doublet formed between the last occupation of chronicle F and the first occupation of chronicle E.

Thus, the fuliginochronological analysis revealed that a single calcite doublet separates the last soot film attributed to Layer F from the first soot film attributed to Layer E (Fig. S25). In other words, the reconstruction of the occupations' chronicles allowed us to establish that a short time that can be estimated to one year separated the last Neanderthal (Rhodanian Quina type Mousterian – Layer F) and the first *H. sapiens* (Neronian – Layer E) occupations. *H. sapiens* thus succeeded the Neanderthals who preceded them at the site in a very short time (much less than a human lifetime and estimated to one year) and were thus strictly penecontemporaneous in the same territory surrounding Grotte Mandrin.

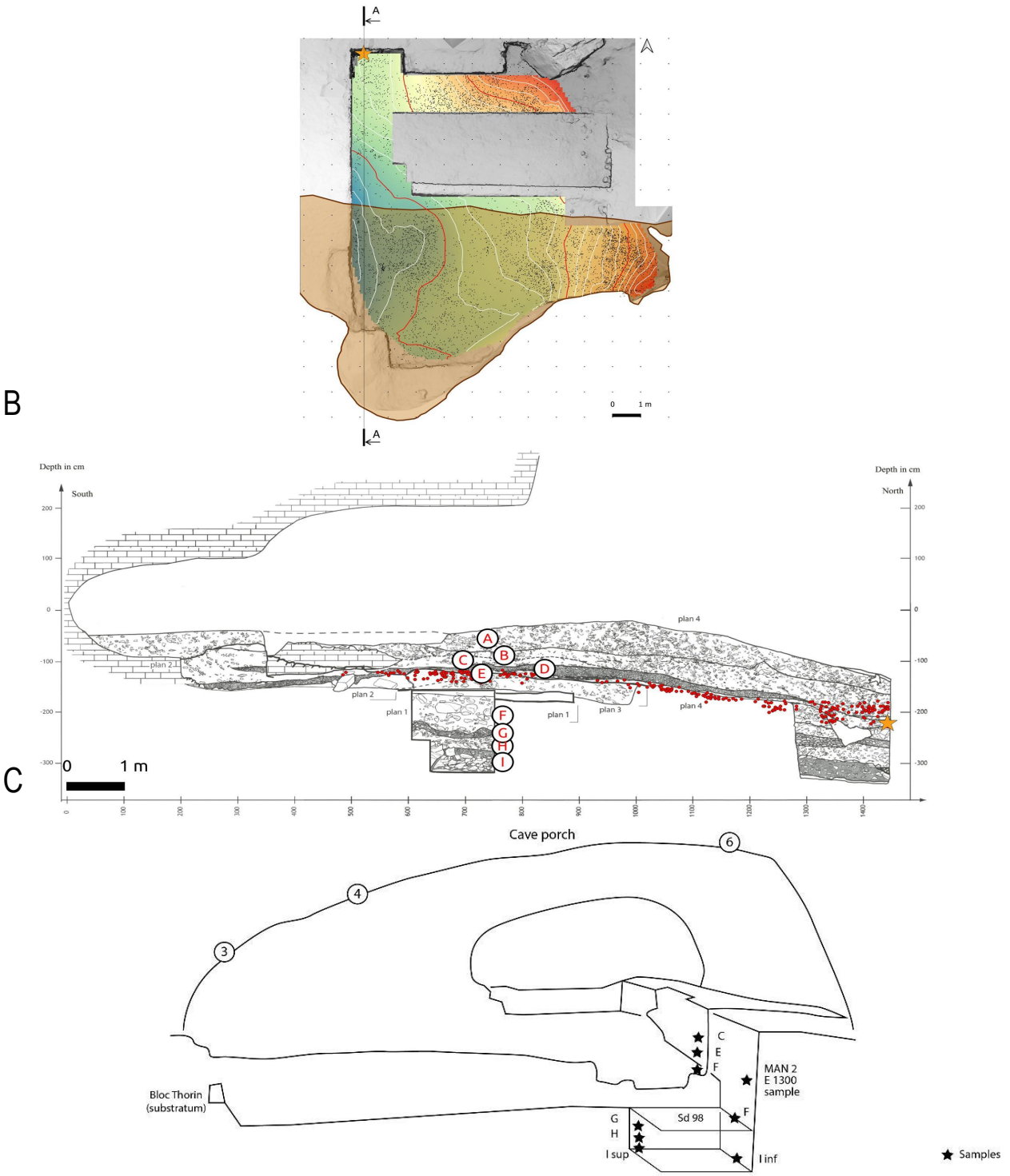

Fig. S1A. Spatial Projections of the Archaeological Material from Mandrin. A) 3D map and transversal section of the Grotte Mandrin showing the position of the modern human tooth (Man 12 E 1300; orange star) in Layer E. The hillshaded background is extracted from the current 3D digitizing of the site, integrating the modeled upper interface of Layer E constructed out of all 3D plotted elements from Layer E. The altimetric step of the contours is 10 cm, this surface is interpolated from the upper remains (built with QGIS 3.8.1). B) North-south profile of the cave. The section is in close contact with Man12 E 1300 *Homo sapiens* tooth. Red dots represent projection of Layer E archeological material. C) Location of the luminescence samples (stars) in relation to the Man 12 E 1300 tooth.

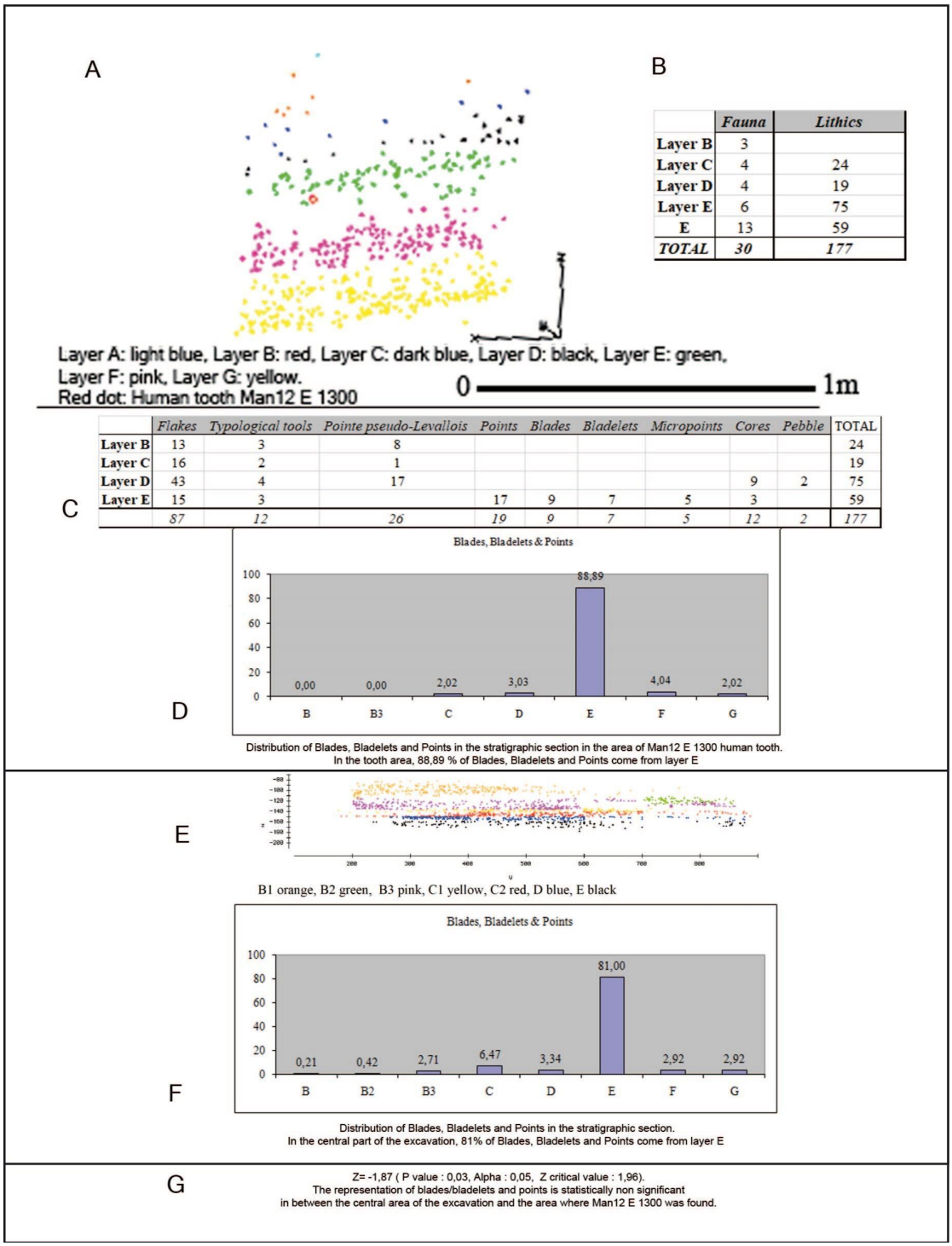

Fig. S1B. Spatial Projections and technical compositions of the Archaeological Material surrounding Man12 E 1300 *Homo sapiens* tooth
A: Projection of the 3D coordinates from archaeological material of Layers B to G in direct contact with Man 12 E 1300 tooth. B: Archeological composition of the 207 plotted archeological material above Man12 E 1300. These elements are mainly lithics (177 lithics vs 30 fauna remains). C: Technical composition of the 177 lithics above Man12 E 1300 tooth.
The histograms D show the distribution in the Man12 E 1300 area of the blades, bladelets and points, representing the most distinctive technical elements of the Neronian. E: Projection of the 3D coordinates from archaeological material of Layers B1 to E in the central part of the cave. The histograms in F show the distribution in that central area of the blades, bladelets and points, representing the most distinctive technical elements of the Neronian. Histograms D and F show the exact same technical components of the lithic industry in both the central part of the cave and around the Man12 E 1300 tooth, with a very high representation of blades, bladelets and points in the Neronian, in any area of the layer E. G: statistical Z-test. Comparison of the representation of Layer E blades, bladelets, and points in between the central part of the excavation and the area where Man 12 E 1300 tooth was. The test shows that there are no significant differences in proportions between these different areas.

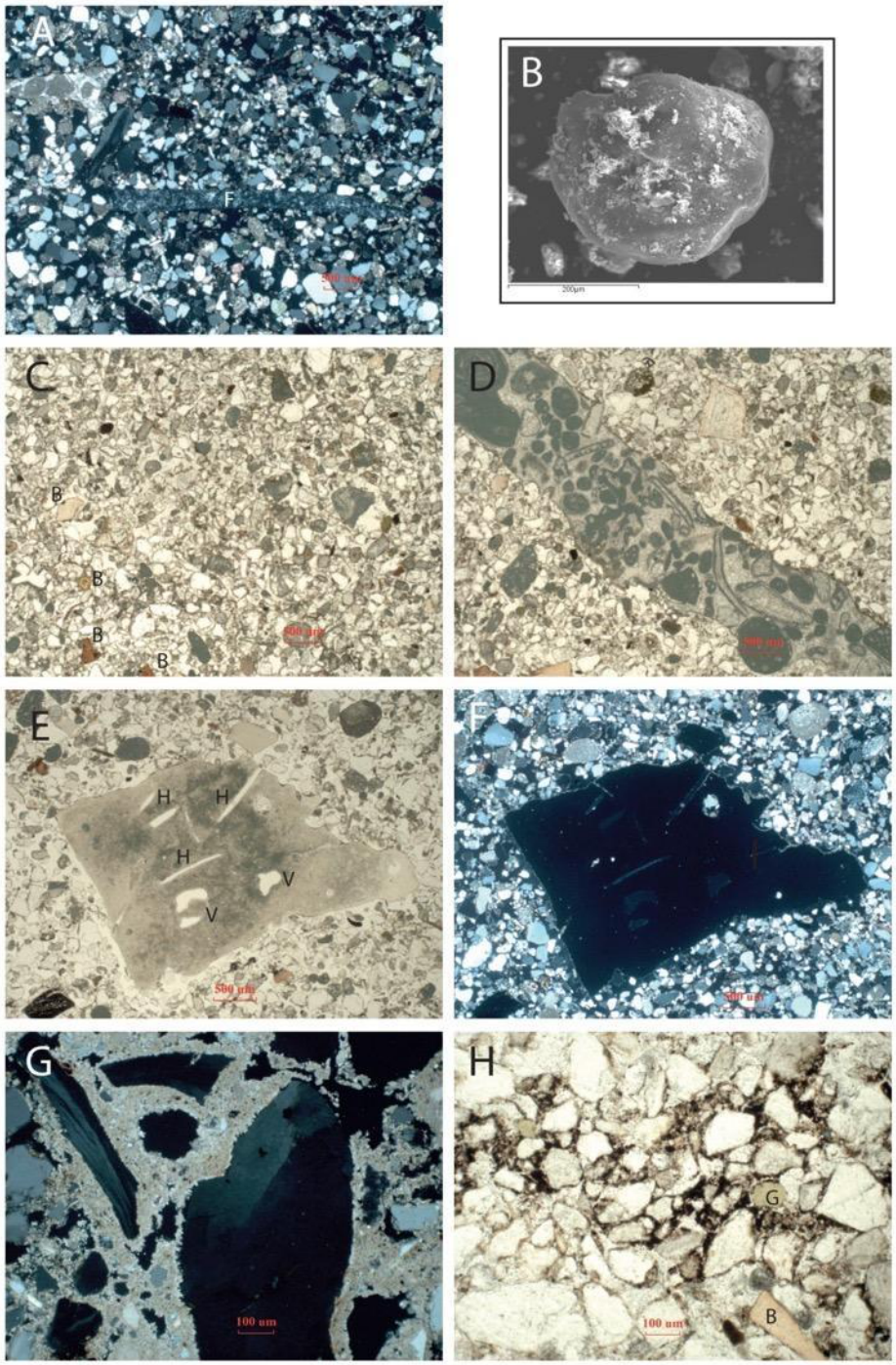

Fig. S2. A) Loose, sandy Layer E sediment composed mostly of quartz sand. Note the presence of a horizontally positioned flint flake (F). Sample MAN.11.14, Crossed Polarized Light (XPL). B) SEM image of a rounded quartz grain from Layer E. C) Plane polarized light (PPL) view of Layer E sediment (Sample MAN-10-2078). Note the presence of sand-sized bone fragments (B). D) PPL view of a fresh angular fossiliferous limestone fragment in Layer E (Sample MAN-10-2078). Note that the rounded dark grey sand grains scattered throughout the sediment here and in the previous image (C) correspond to the oolitic inclusions within the limestone. E-F) Coprolite fragment in sample MAN-11-13 (E in PPL and F in XPL). Note the vesicles (V) and voids after hair follicles (H). G) Micrite cement in sample MAN-11-17 (XPL). H) Concentration of organic matter in sample MAN-07-8 (PPL). Note the presence of a glauconite grain (G), which is common in Layer E.

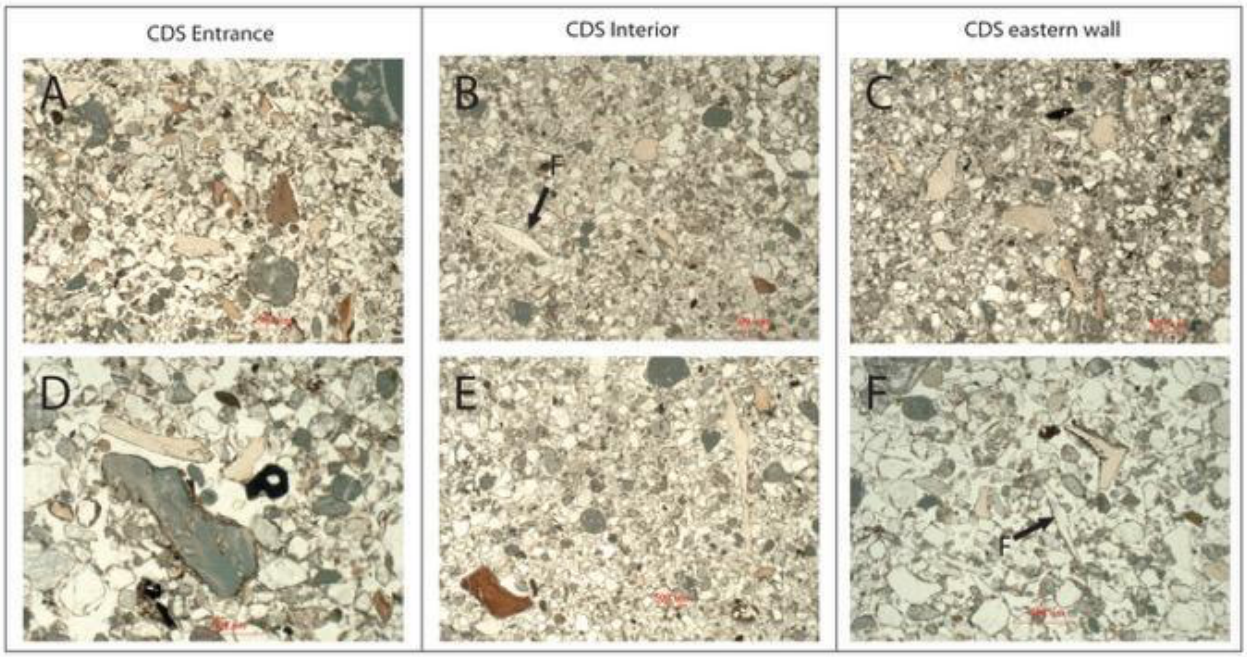

Fig. S3. Plane polarized light (PPL) images of sediment from Layer E from the shelter's entrance (Sample MAN-06-4), interior (Sample MAN-10-2078) and Eastern wall (Samples MAN-07-8 and MAN-11-18). There are no significant differences in composition and microstructure among these zones. They all exhibit mixed anthropogenic material embedded in sand. Note the coexistence of burnt bone (strong brown) and unburnt or slightly burnt (pale brown) bone (A and E), calcined (light grey color) and unburnt bone (D), the presence of flint knapping debris ("F" in B and F) and char (black particle in D). G) Plane polarized light (PPL) image of sediment from Layer F.

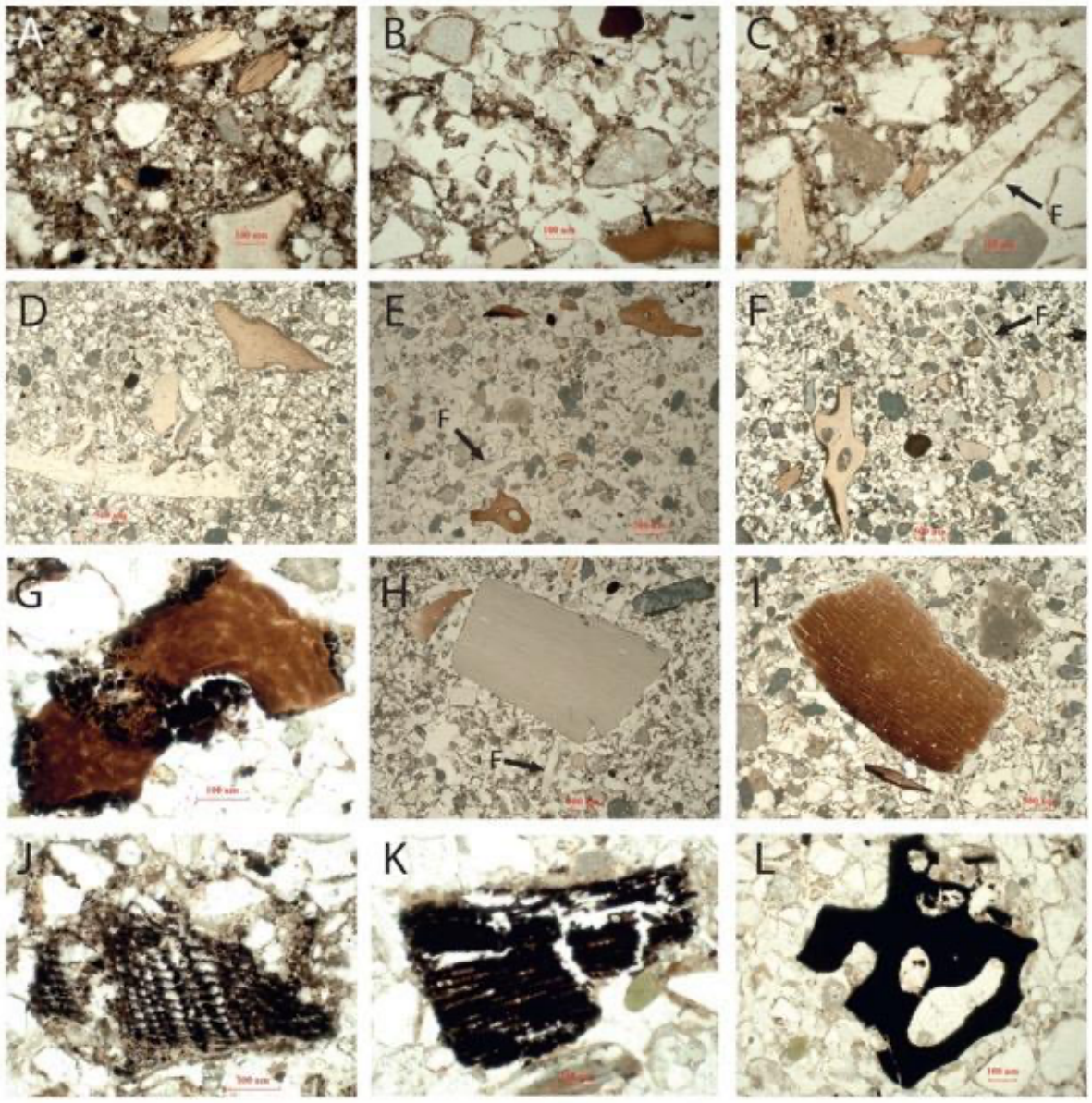

Fig. S4. Plane polarized light (PPL) images of a combustion feature in Layer E from the near shelter's entrance (Samples MAN-10-2040, MAN-08-4e, MAN-11-14 and MAN-11-15). A, B and C show the upper part, with a black dusty matrix. Note the presence of burnt bone fragments (brown) and a flint flake (F) in C. Views D, E and F show the underlying sediment, which is not significantly different from other zones of Layer E. Note the presence of burnt bone and flint knapping debris (F). G) Burnt bone fragment with charred organic matter attached to it. H) Calcined bone fragment and flint flake (F). I) Burnt bone fragment. J, K) Reworked charcoal fragments. L) Char fragment.

Fig. S5. Mandrin Layer F lithic industry. Rhodanian Quina. Mousterian. Scraper with Quina retouch.

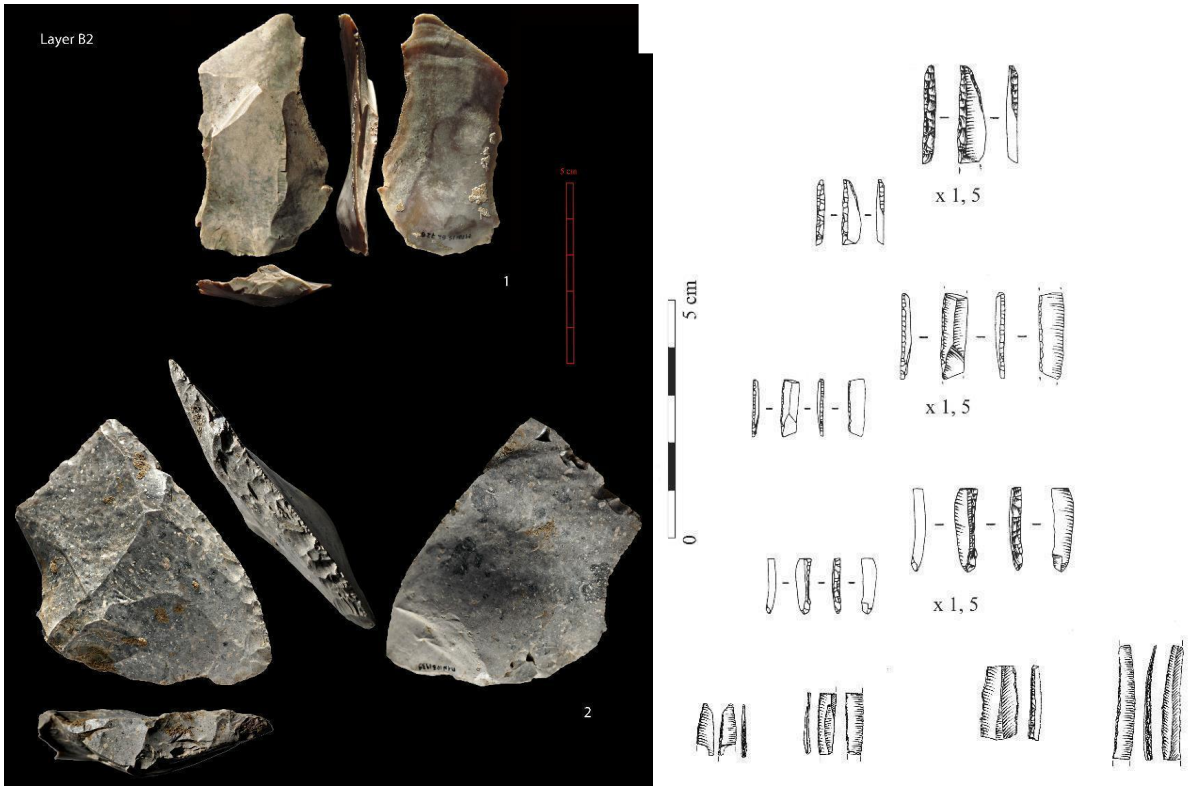

Fig. S6. Post-Neronian Layer B2 and B1 lithic industries. a, Mandrin Layer B2 lithic industry. Post-Neronian II. Mousterian. 1, Levallois flake. 2, Mousterian scraper on Levallois flake. **b,** Mandrin Layer B1 lithic industry. Protoaurignacian retouched bladelets.

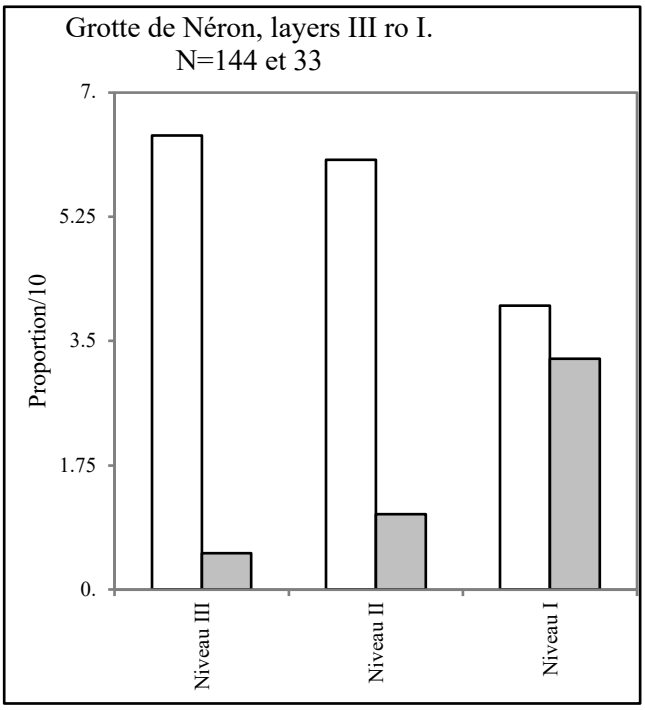

Fig. S7. Evolution of typological groups at Grotte de Néron from Layers III to I. The Mousterian group in white progressively decreases and the Upper Paleolithic group grows gradually from Layers III (left) to I (right), with Layer I being attributed to the Neronian (*151*).

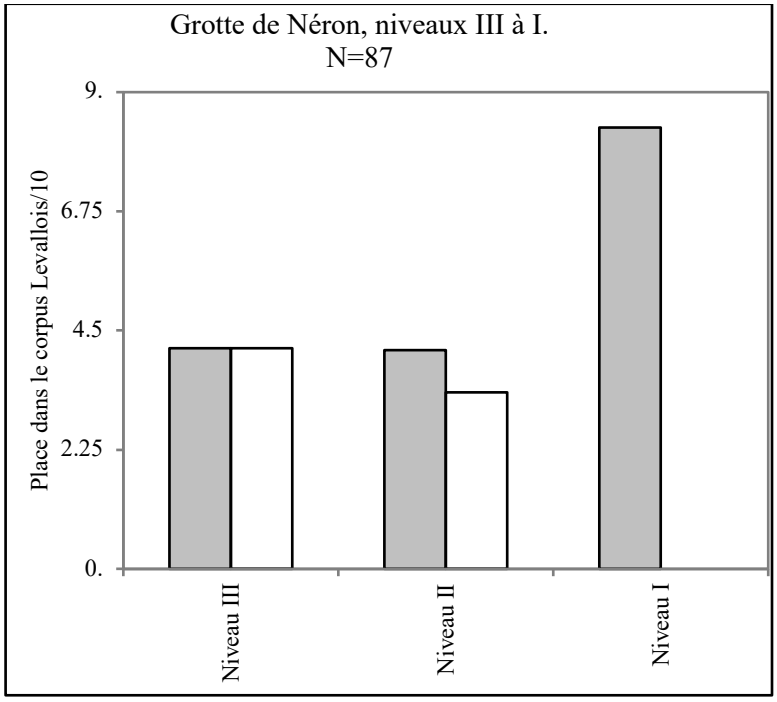

Fig. S8. Grotte de Néron, layers III to I. Proportions of flakes and points among Levallois production. Layers III and II show a decrease of Levallois flake (white) proportions and their full disappearance in the Neronian Layer I, and their replacement by Levallois points (grey) (*151*).

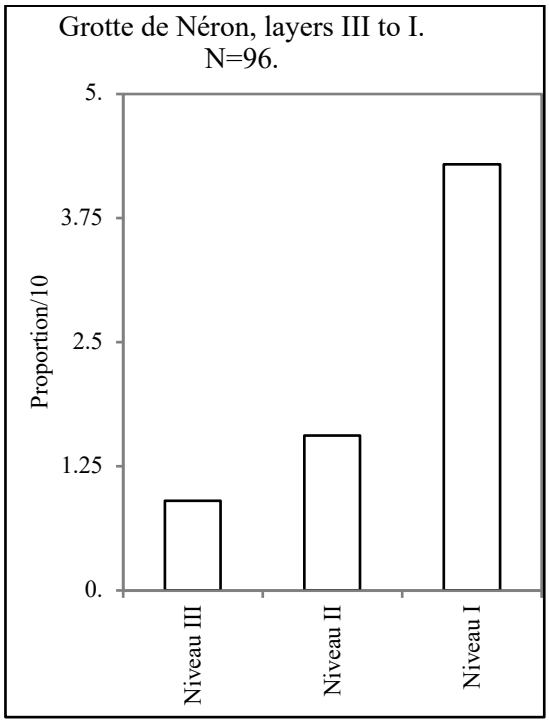

Fig. S9. Grotte de Néron, layers III to I. Proportion of Levallois blanks integrated in the typological corpus, showing a gradual increase from Layers III to I (I=Neronian) (*151*).

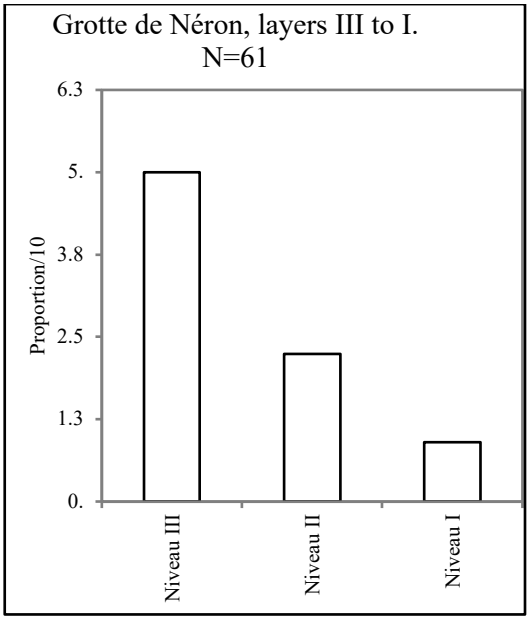

Fig. S10. Grotte de Néron, layers III to I. Proportion of pseudo-Levallois points integrated in the tool kit, showing their gradual disappearance (*151*). Pseudo-Levallois points are diagnostic of Mousterian technologies.

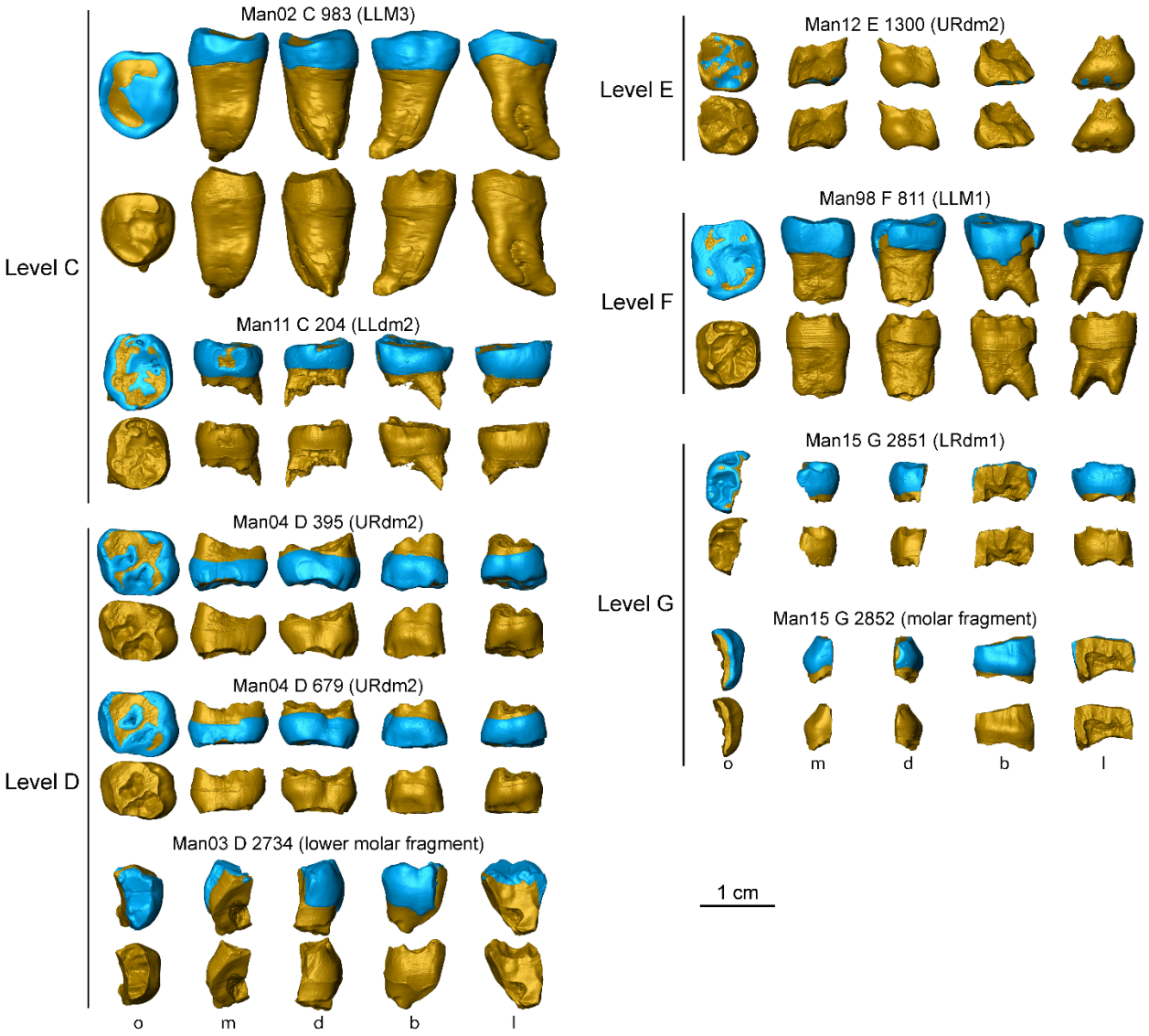

Fig. S11. Virtual renderings of the hominin dental specimens from the Layers G to C from Mandrin. For each specimen, the external surface (upper raw) and the dentine morphology (lower raw) are shown. LLdm2, deciduous lower left second molar; LLM1, permanent lower left first molar; LRM3, permanent lower right third molar; URdm2, deciduous upper right second molar; b, buccal; d, distal; l, lingual; m, mesial; o, occlusal; buccal; l, lingual; o, occlusal.

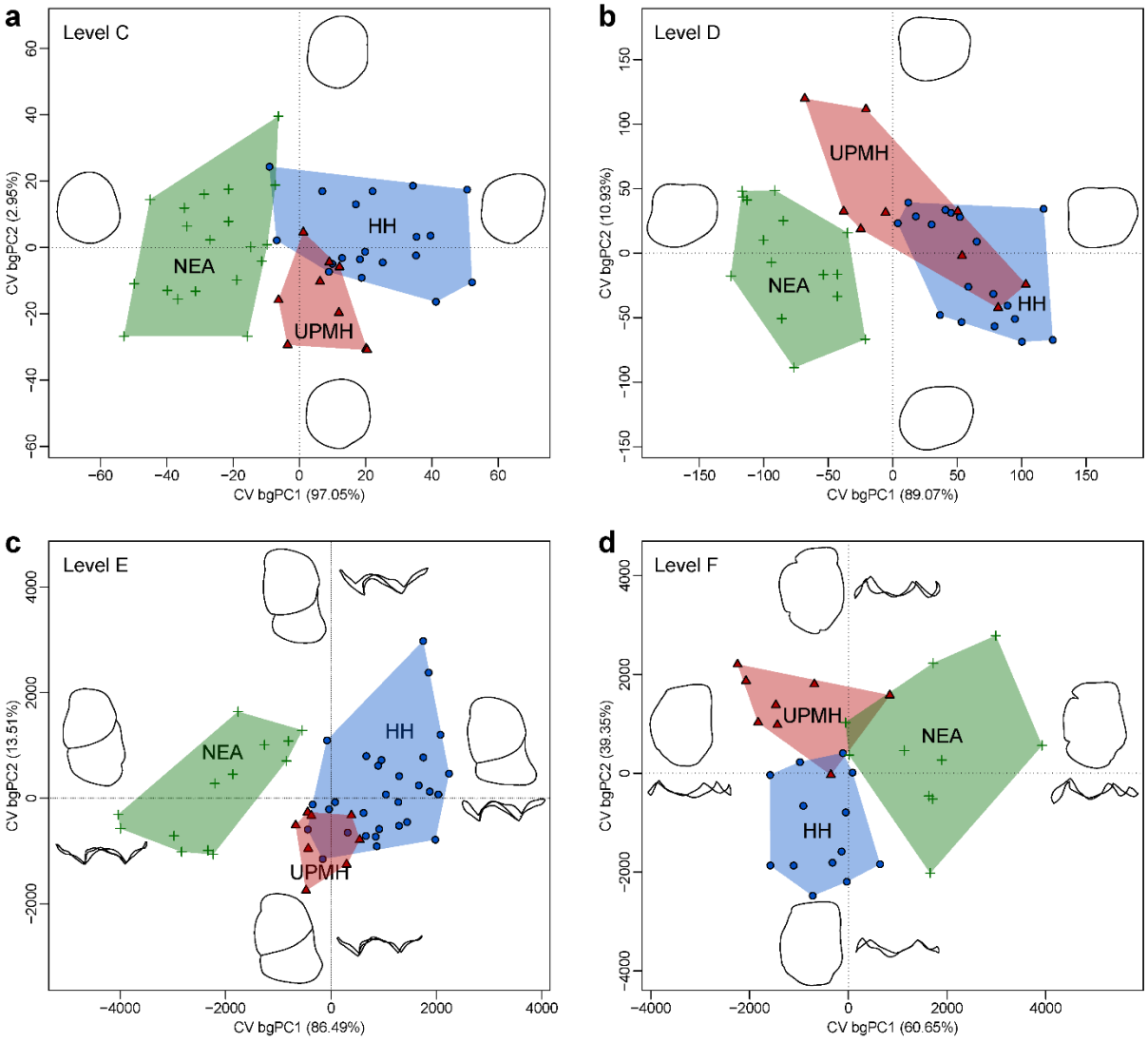

Fig. S12. Geometric morphometric analyses of the crown outline and EDJ shape. a, b, Cross-validated between-group principal component analyses (bgPCA) based on the 2D landmarks Procrustes-registered shape coordinates of the crown outline of the deciduous lower second molar (Ldm2; **a**) and of the deciduous upper second molar (Udm2; **b**) of the comparative fossil and extant hominin groups. **c, d,** Cross-validated bgPCA based on the 3D landmarks Procrustes-registered shape coordinates of the enamel-dentine junction of the Udm2 (**c**) and of the permanent lower first molar (LM1; **d**) of the comparative fossil and extant hominin groups. NEA, Neanderthals; UPMH, Upper Pleistocene modern humans; HH, Holocene humans; MAN_geom, geometric-based reconstruction of the Mandrin specimens; MAN_MH, modern human-based reconstruction of the Mandrin specimens; MAN_NEA, Neanderthal-based reconstruction of the Mandrin specimens (Table S14).

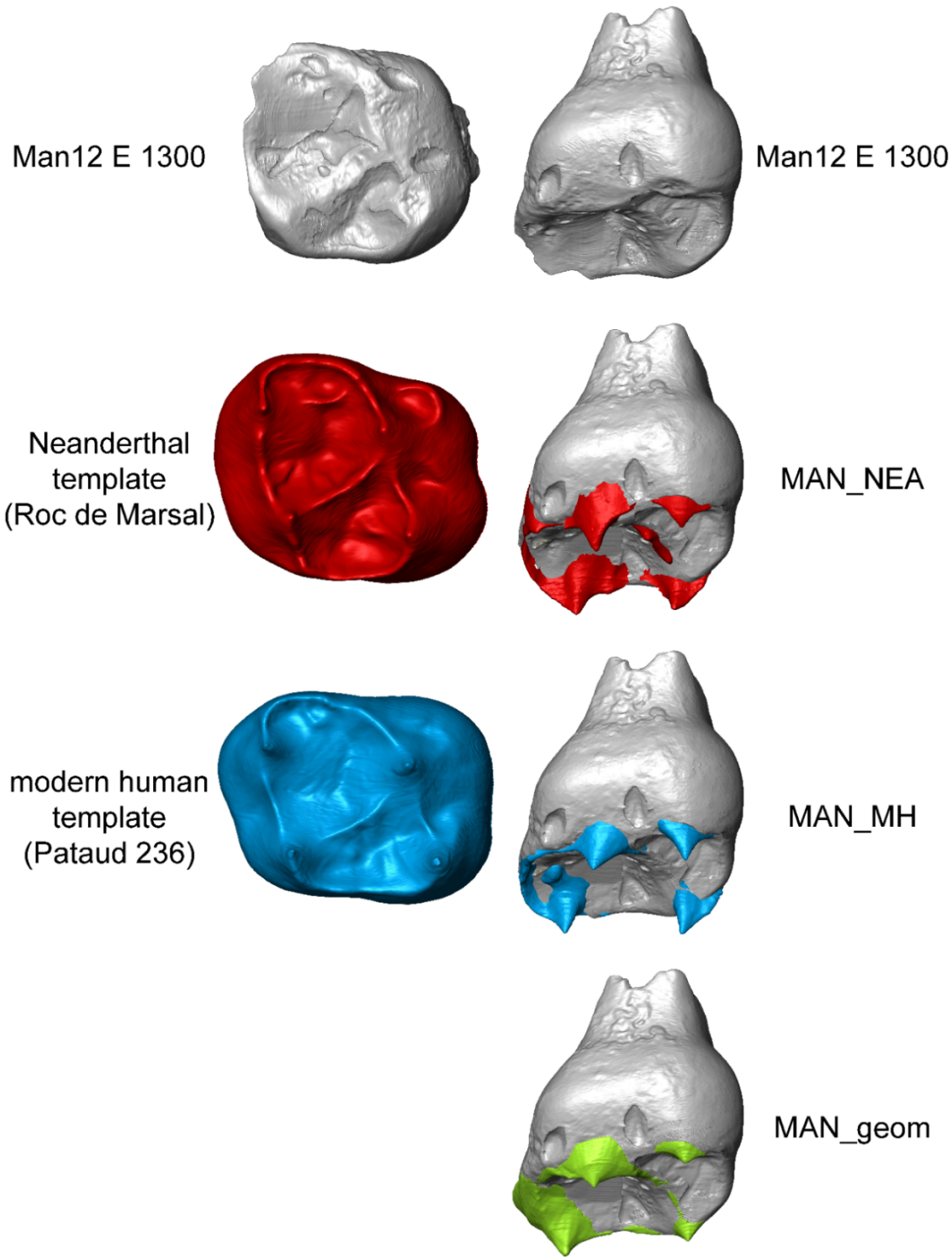

Fig. S13. Virtual reconstructions of the Man12 E 1300 specimen using two different methods. The first reconstruction method is based on the superimposition of a Neanderthal (MAN_NEA) and of a modern human EDJ template (MAN_MH) on the Mandrin specimen, and the second approach is based on the geometry of the preserved EDJ of Man12 E 1300 (MAN_geom). The specimens are showed in occlusal view on the left and in lingual view on the right

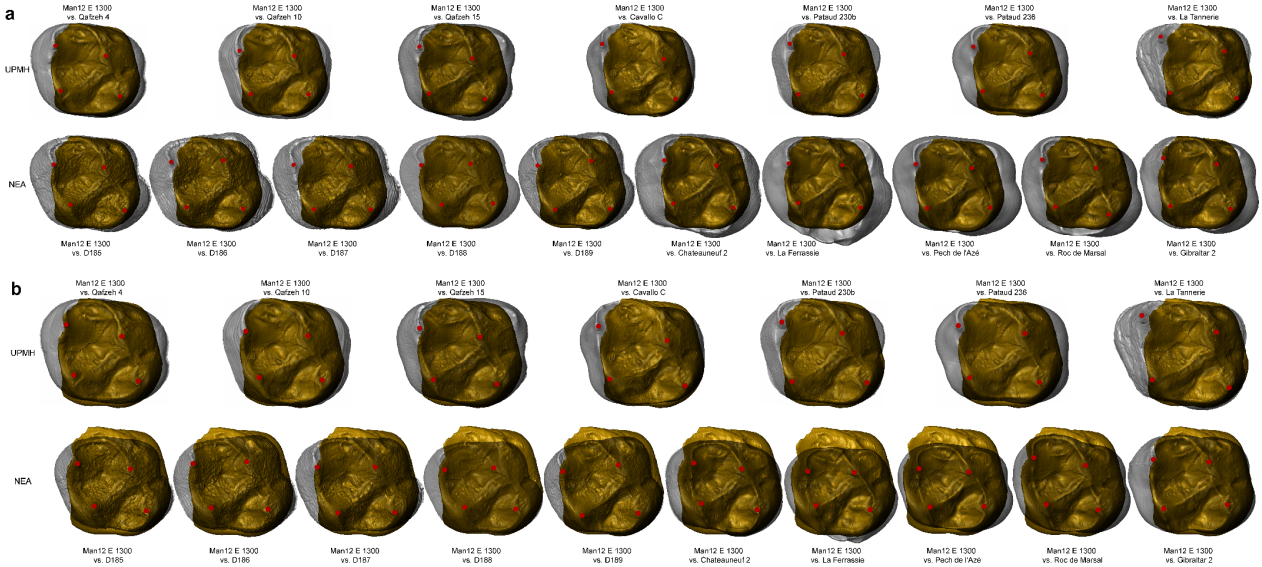

Fig. S14. Superimposition of the Man12 E 1300 EDJ (yellow) with that of Upper Pleistocene modern humans (UPMH) and Neanderthals (NEA). The EDJ Man12 E 1300 was aligned with other specimens following two methods: using the preserved parts of the trigon of the Layer E specimen (**a**; based the preserved portion of the mesial marginal crest, the position of the protocone dentine horn, of the oblique crest and of the metacone dentine horn) and using the trigon (**b**, aligning the EDJs based on the position of the protocone, metacone and hypocone dentine horns, as well as of the oblique crest, distal marginal crest and lingual crest). The position of the comparative specimens' dentine horns are highlighted by red dots.

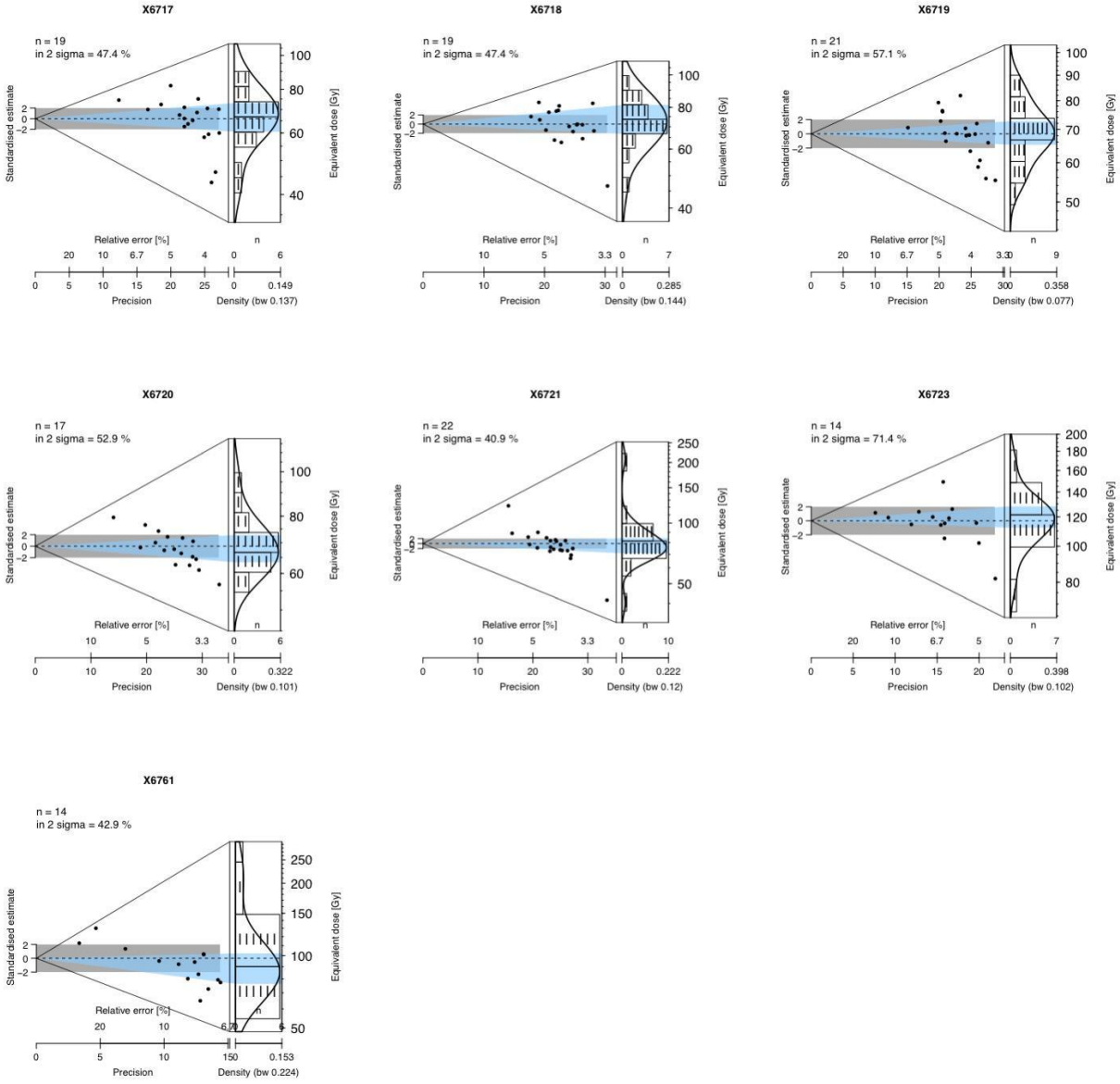

Fig. S15. Abanicoplots displaying the distribution of multiple-grain quartz equivalent dose measurements and their associated data precision and error scatter (*104*). The plot combines a radial plot (bivariate plot on the left side) with a histogram and kernel density estimate curve (univariate plots on the right side) using the default function tool developed within the package 'Luminescence' (*105*) for the statistical programming language 'R' (*90*). The 2σ dispersion range is shown in grey and the light blue polygon characterizes the 1σ frequency distribution of the primary data.

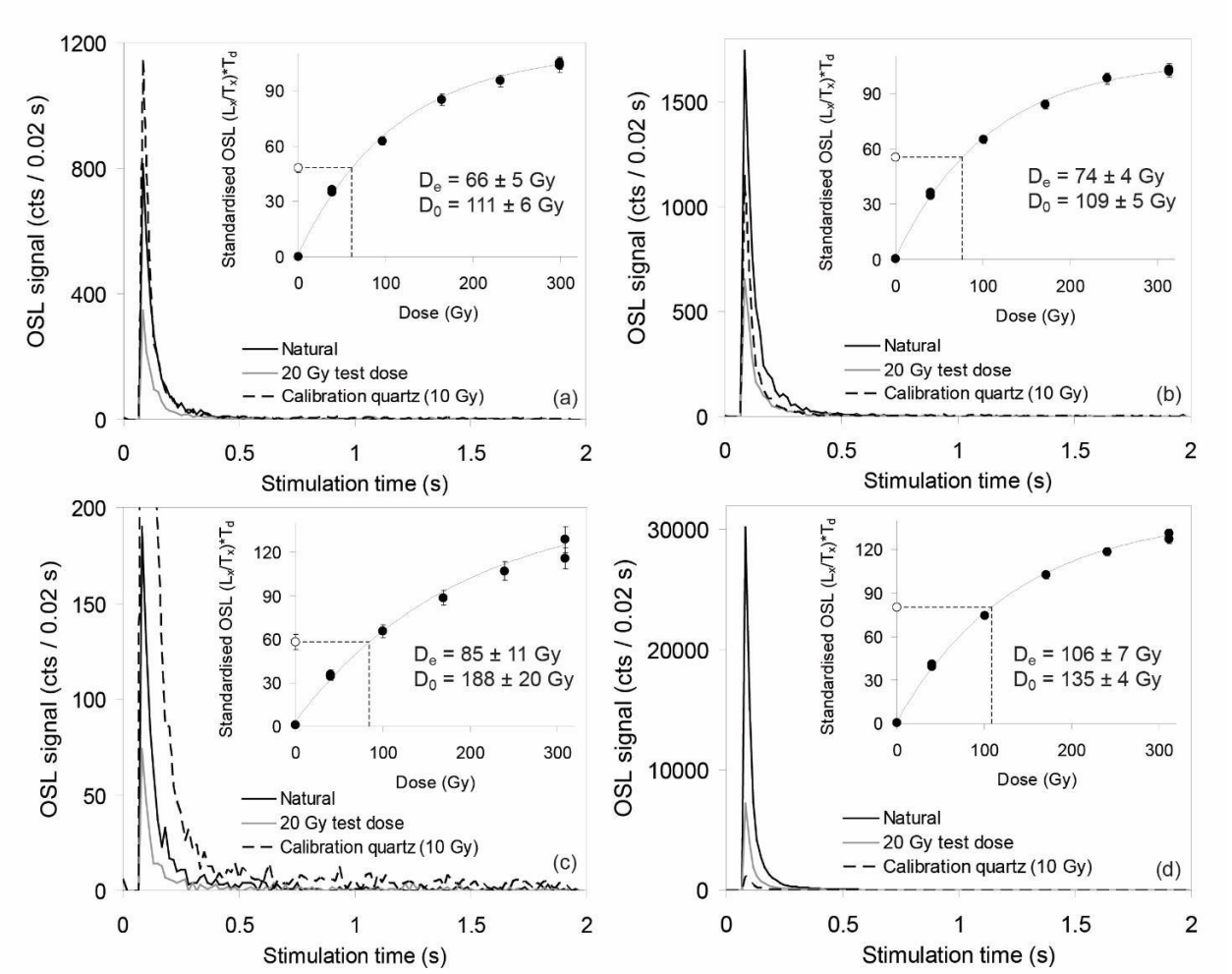

Figure S16. Representative single-grain OSL decay and dose-response curves for quartz grains from sample MAN19-5. The decay curve of a fast-component dominated calibration quartz grain is shown for comparison (Risø calibration quartz standard from Rømø, batch #98; ref. *133*. In the insets, the open circle denotes the sensitivity-corrected natural OSL signal, and filled circles denote the sensitivity-corrected regenerated OSL signals. The D_0 value characterizes the rate of signal saturation with respect to administered dose and equates to the dose value for which the saturating exponential dose-response curve slope is $1/e$ (or ~ 0.37) of its initial value. (a) grain with moderate OSL signal brightness (T_n intensity = 100–1,000 counts / 0.08 s). (b) grain with bright OSL signal (T_n intensity = ~1,000–10,000 counts / 0.08 s). (c) grain with relatively dim OSL signal (T_n intensity = <100 counts / 0.08 s). (d) grain with very bright OSL signal (T_n intensity = >10,000 counts / 0.08 s).

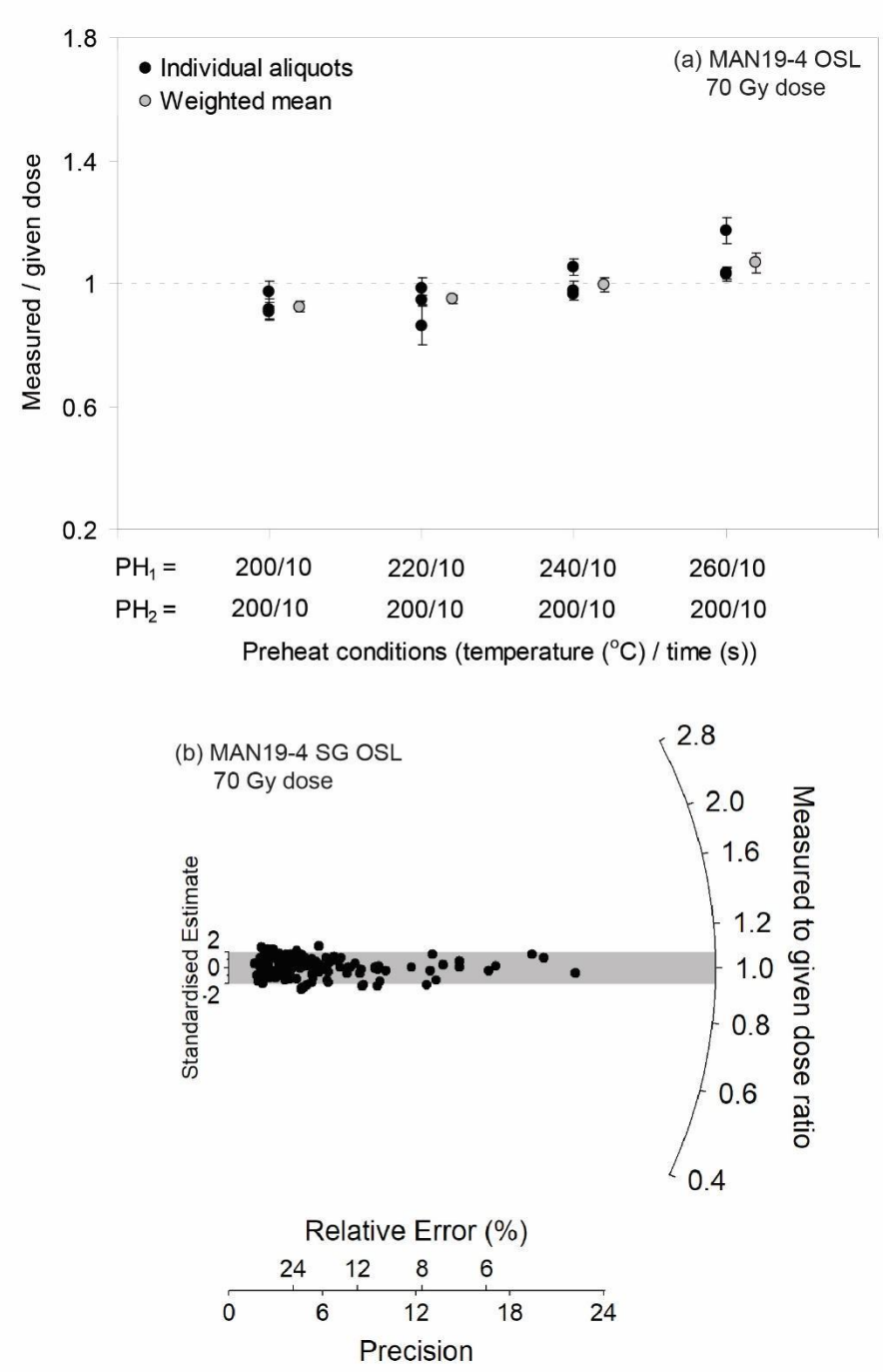

Figure S17. Dose-recovery test results for sample MAN19-4. (a) Measured-to-given dose OSL ratios versus regenerative dose preheat (PH_1) and test dose preheat (PH_2) temperature (held for 10 s) for ~180-grain aliquots of sample MAN19-4. (b) Radial plot showing the measured-to-given dose OSL ratios obtained for individual quartz grains of sample MAN19-4 in the single-grain SAR dose-recovery test. The grey shaded region is centered on the administered dose for each grain (sample average = 70 Gy).

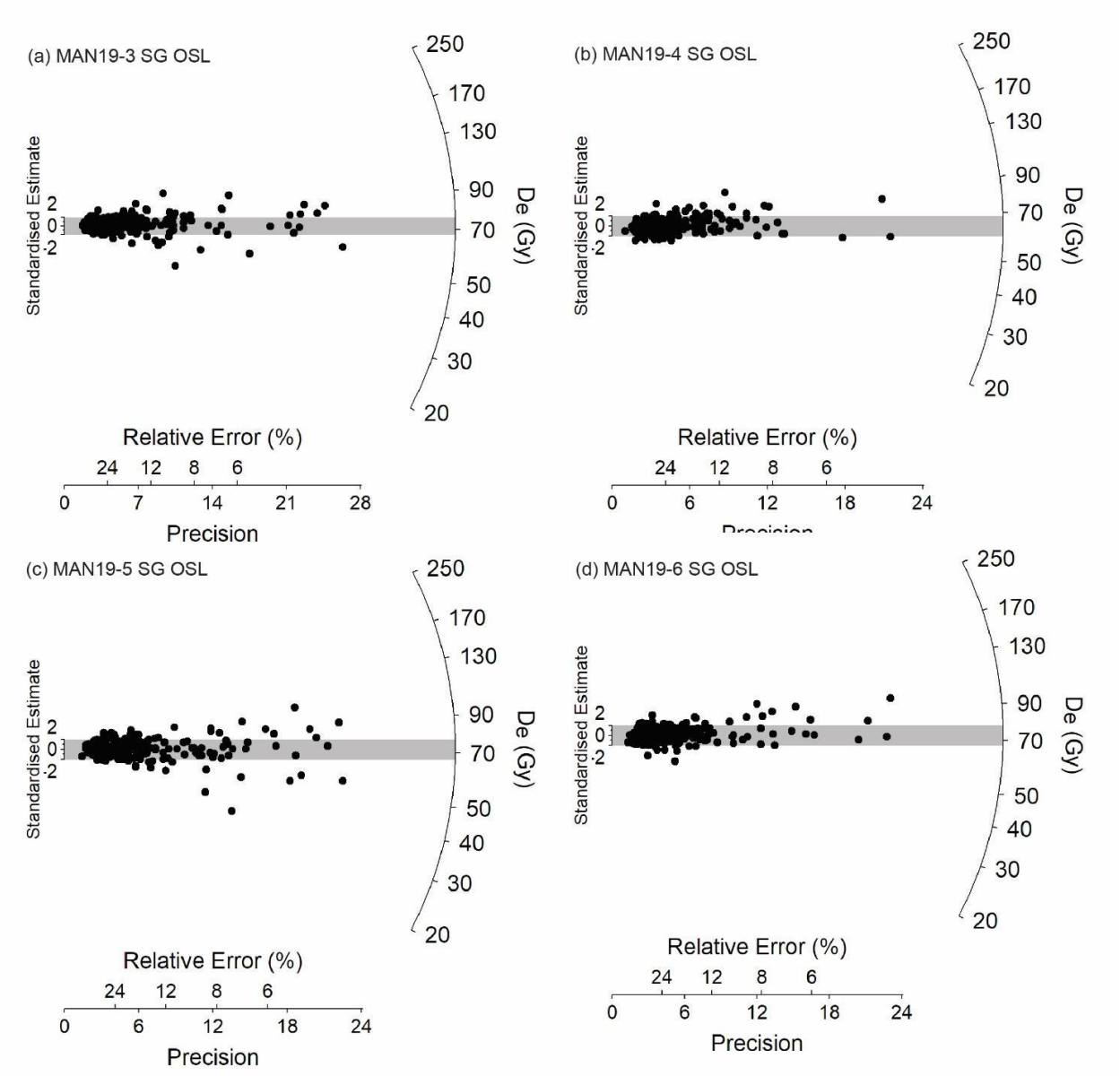

Figure S18. Single-grain OSL D_e distributions for the 2019 luminescence samples, shown as radial plots. The grey bands are centered on the D_e values used for the age calculations, which were derived using the central age model (CAM).

a.

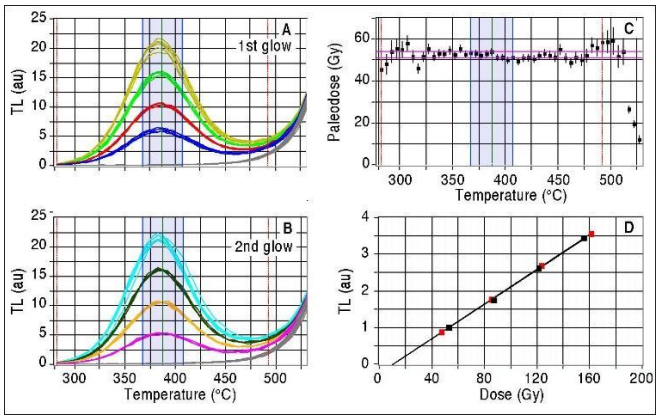

b.

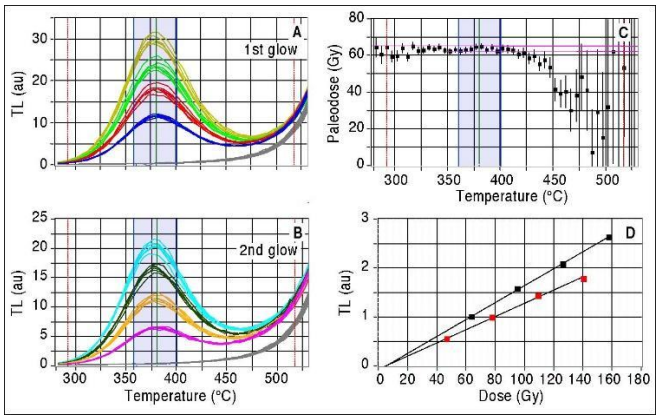

c.

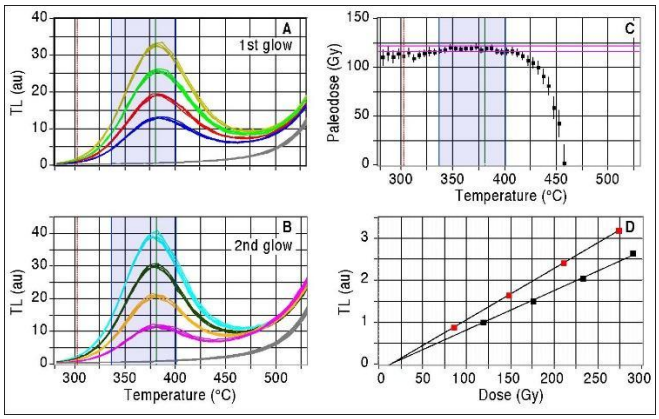

Fig S19. Thermoluminescence dating of flint samples X1736 (a), X6713 (b), and X6714 (c). (A) first glow thermoluminescence curves of the natural sample (in blue) and for added doses; (B) second glow curves obtained after bleaching (350°C, 1.5 hr) and re-irradiations. All measurements are done on six aliquots at 5°C/s with a preheat at 320°C for 10 s. The plateau test (C) is plotted after correction of linearity deviations at each temperature. Growth curves (D) and best fit straight lines are plotted taking into account the paleodose value on the X axis; 1st glow curve (black squares) and 2nd glow curve (red squares) are plotted by integrating the blue shaded zone of the luminescence signal.

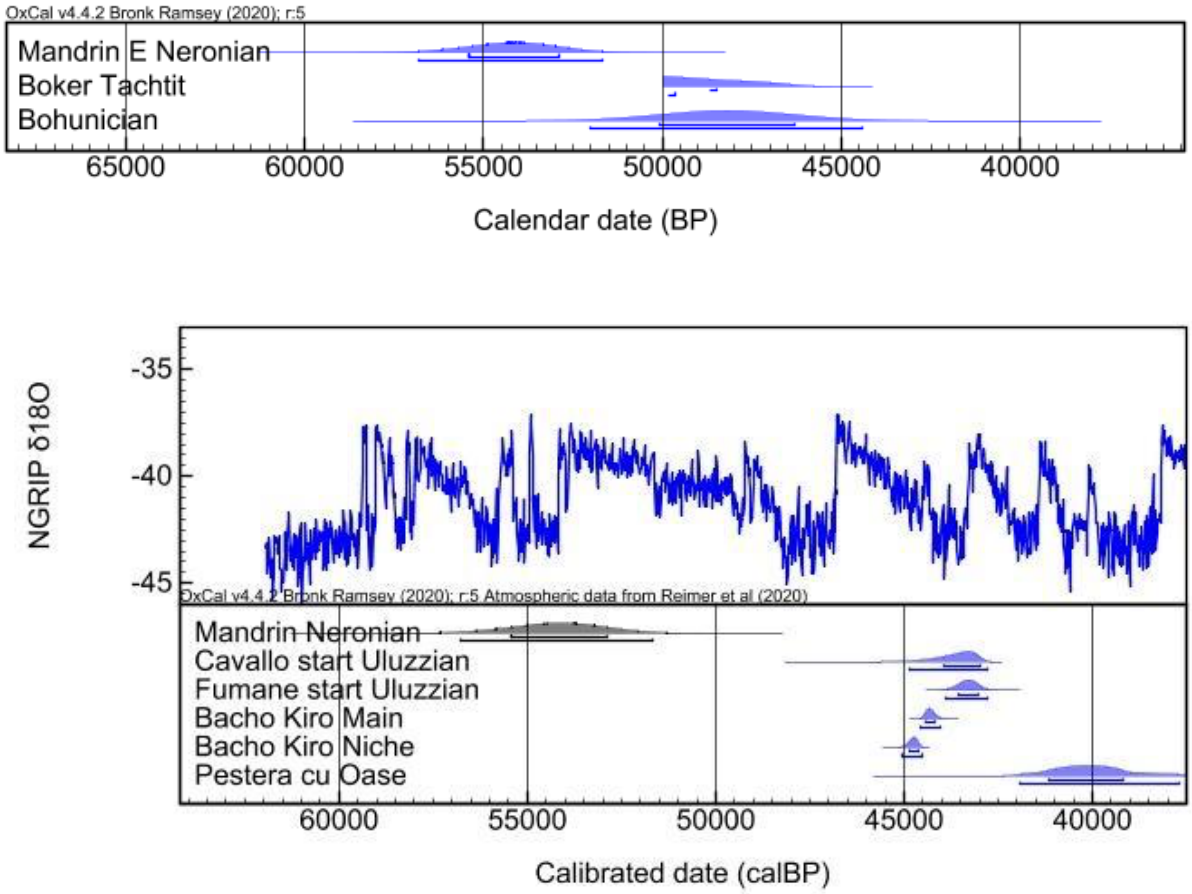

Fig. S20. Comparisons of the Mandrin Neronian date with: ***top***, the Boker Tachtit IUP and the Bohunician at Brno-Bohunice (*61, 62*) and ***bottom***, with other earliest Modern human remains from Europe.

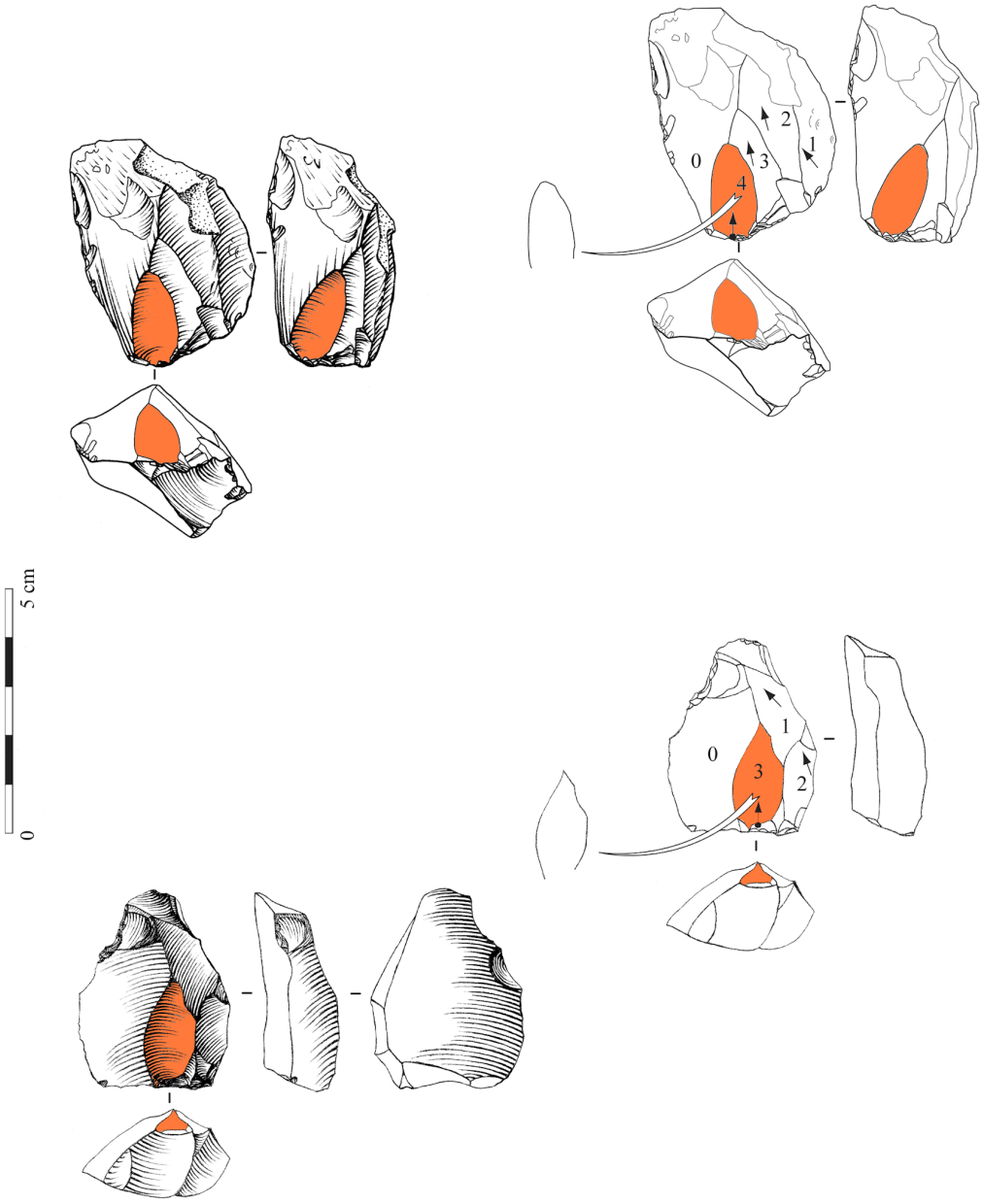

Fig. S21. Cores from Mandrin Layer E (top) and Ksar Akil Unit XXIV (bottom). These cores result from "schéma croisé" flaking, a very specific method first described in the Neronian from Mandrin E (*152*). The left part of the core is a ventral surface. The extraction of the micropoint (orange) is precisely located in between the flaking surface of the right and the ventral surface of the left of the core. This "schéma croisé" allows the obtention of a (micro)point showing perfect axial and transversal symmetry and having one of its flanks composed of a positive surface. This very specific schéma is well attested in both IUP industries of Mandrin E and Ksar Akil.

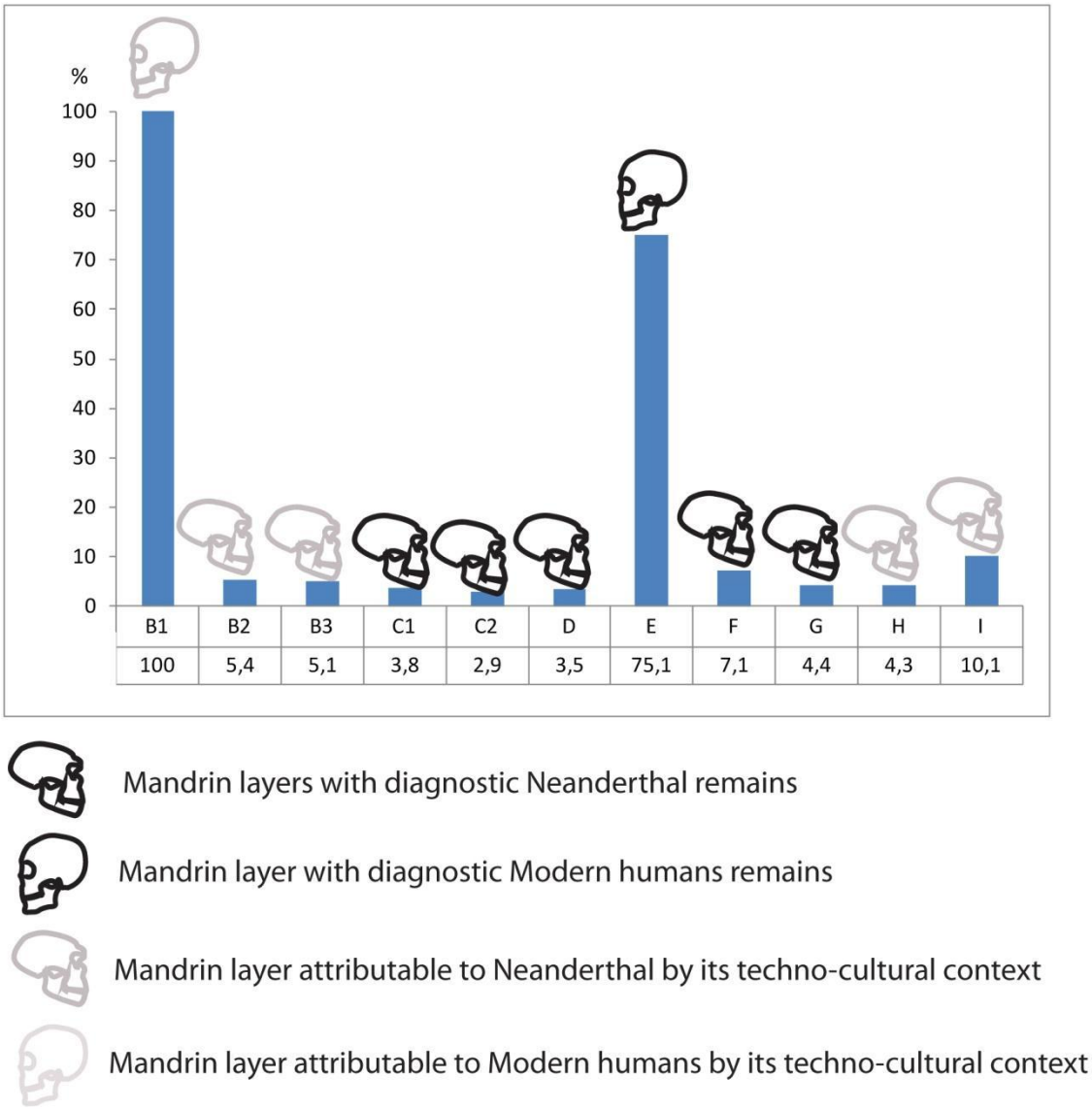

Fig. S22. Association between hominin species and distribution of blades, bladelets and points by archaeological Layer at Grotte Mandrin. The proportions of artefacts are represented by blue bars for each layer. The layers preserving human remains (mostly teeth that are taxonomically diagnostic) are indicated by dark skull drawings while for the layers delivering only lithic industries, the likely identity of the makers is indicated by semi-transparent skulls. Layer E represents a clear-cut technical anomaly. Layers B2 through D and F through I represent classic Middle Paleolithic technologies attributed to Neanderthals in Europe.

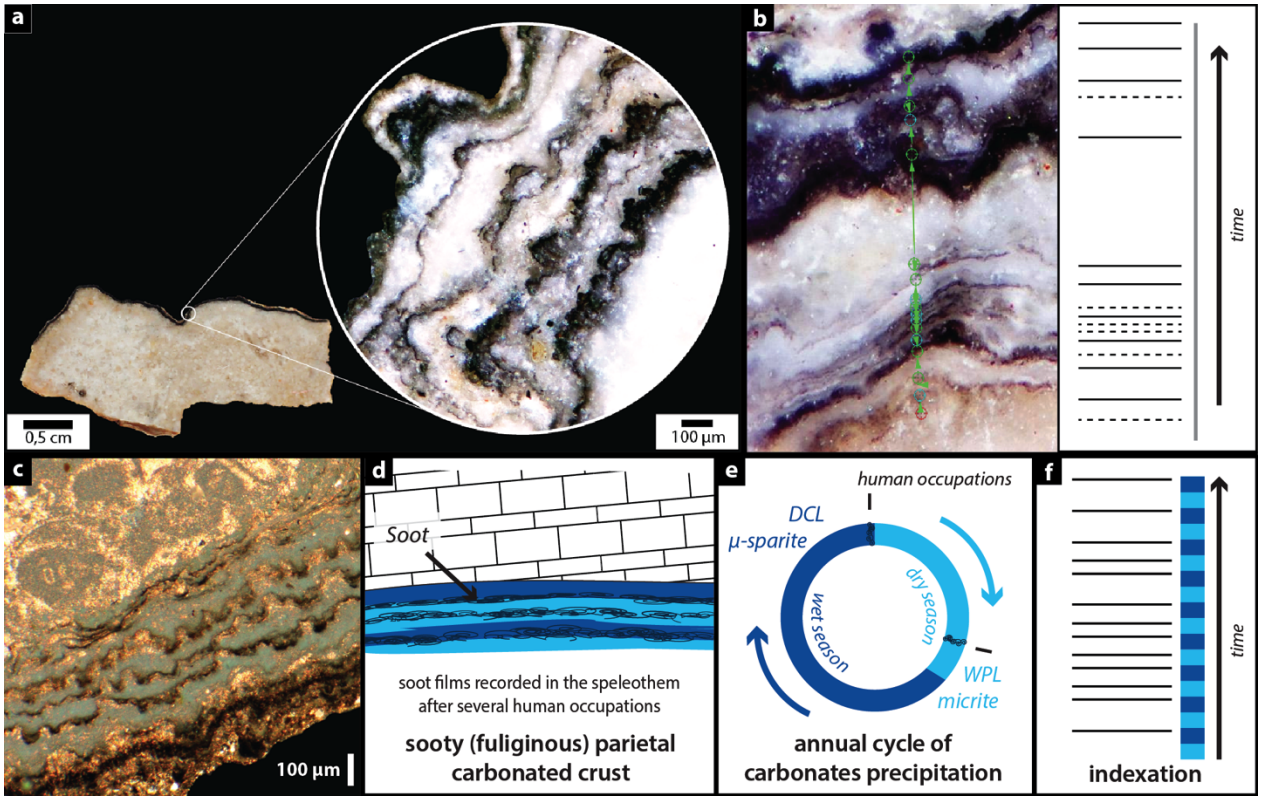

Fig. S23. Overview of fuliginochronology. a: Microscopic observation of a sooty parietal crust from Grotte Mandrin. A single soot film observable with the naked eye is resolved into a multitude of soot films under the microscope (x100, RL). b: Raw data collection under process using the LnSeq module of the Datawald platform (GL Conception). Soot films succession in carbonates is represented as barcode diagrams. Bars represent soot films and dashed lines represent probable soot films. Once the entire sequence has been documented on the sample the long grey line next to the barcode represents speleothem total thickness. c: Photograph of C-MAN34 thin section where soot films are associated with both DCL and WPL. Combination of RL and XPL light enhance the perception of crystalline fabrics (micrite appears opaque and white, microsparite appears translucent) and soot (black films). This lighting allows to document the position of the soot films in relation to the calcite doublets. d: Schematic representation of c. On this theoretical simplified example, soot films are associated both to the end of DCL and to WPL but not exactly in the same way as in C-MAN34 sample (*c*). e: Annual cycle of carbonates precipitation. Two seasons (wet and dry) can be recognized through observation of crystalline fabrics. These two seasons may not last the same length, which is why they are represented in different sizes in this theoretical chart. WPL and DCL may not correspond to 6 months each but DCL+WPL = 1 year at Grotte Mandrin (*188*). Human occupations (marked by soot deposits) are here located as in d. f: Indexation of occupations chronicle on the annual calendar of carbonates precipitation. In this theoretical example (derived from d and e) the soot films are always at the top of the micro-sparite laminae and sometimes in the micritic laminae. There are here one to two occupations per year that are recorded in the parietal carbonated deposit.

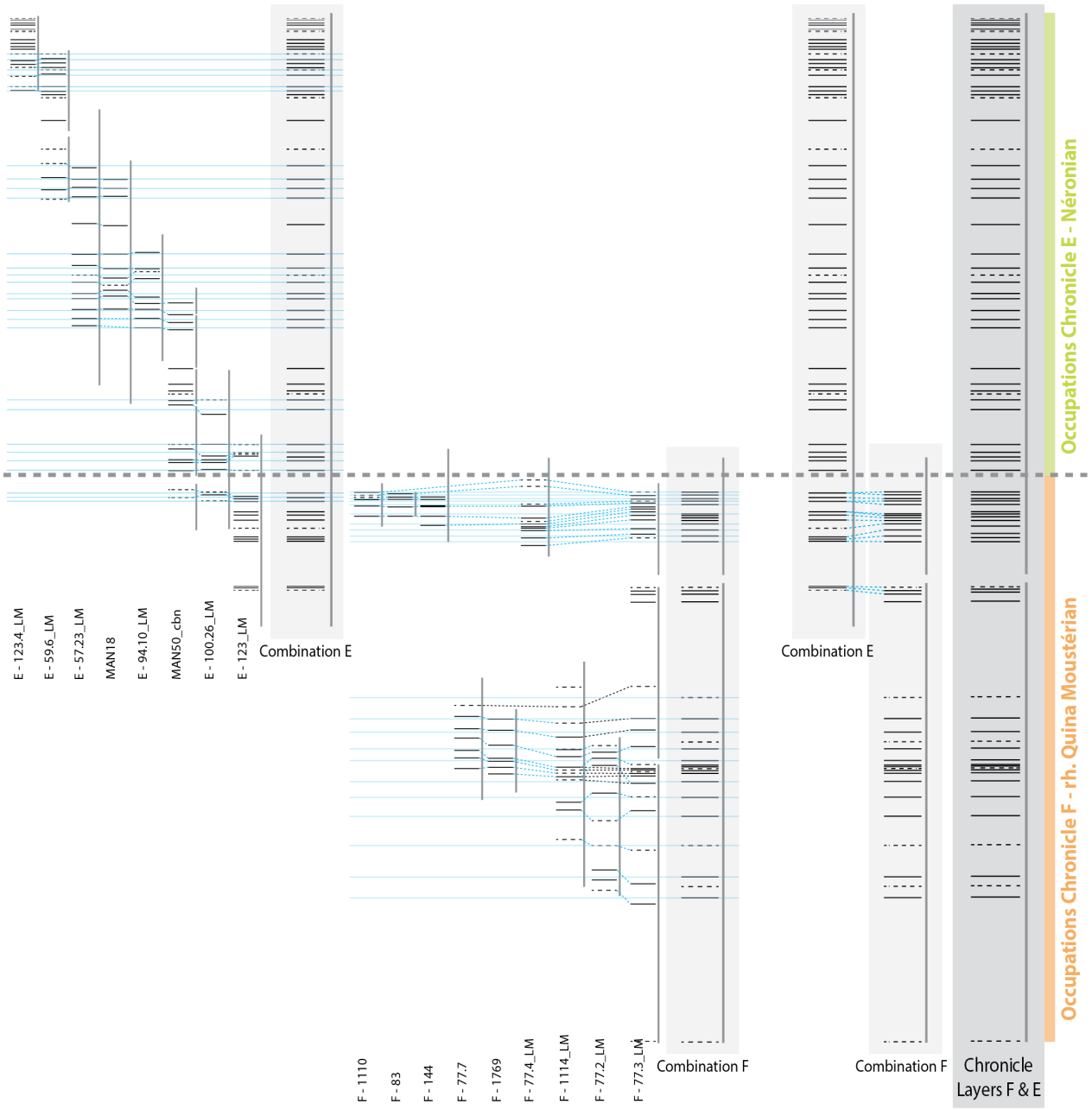

Fig. S24. Construction of Occupations Chronicles for Mandrin Layers F and E. Synchronization of 8 individual sequences from Layer E samples in order to build a combination sequence for layer E. Synchronization of 9 individual sequences from Layer F samples in order to build a combination sequence for Layer F. Because samples found in F cannot have recorded soot films deposited on the shelter's walls during occupations that occurred in Layer E, the beginning of E combination sequence belongs to F. Synchronization of F and E combination sequences, while taking into account the stratigraphic information, makes it possible to reconstruct the chronicles of occupations for Layer F (orange) and for Layer E (green).

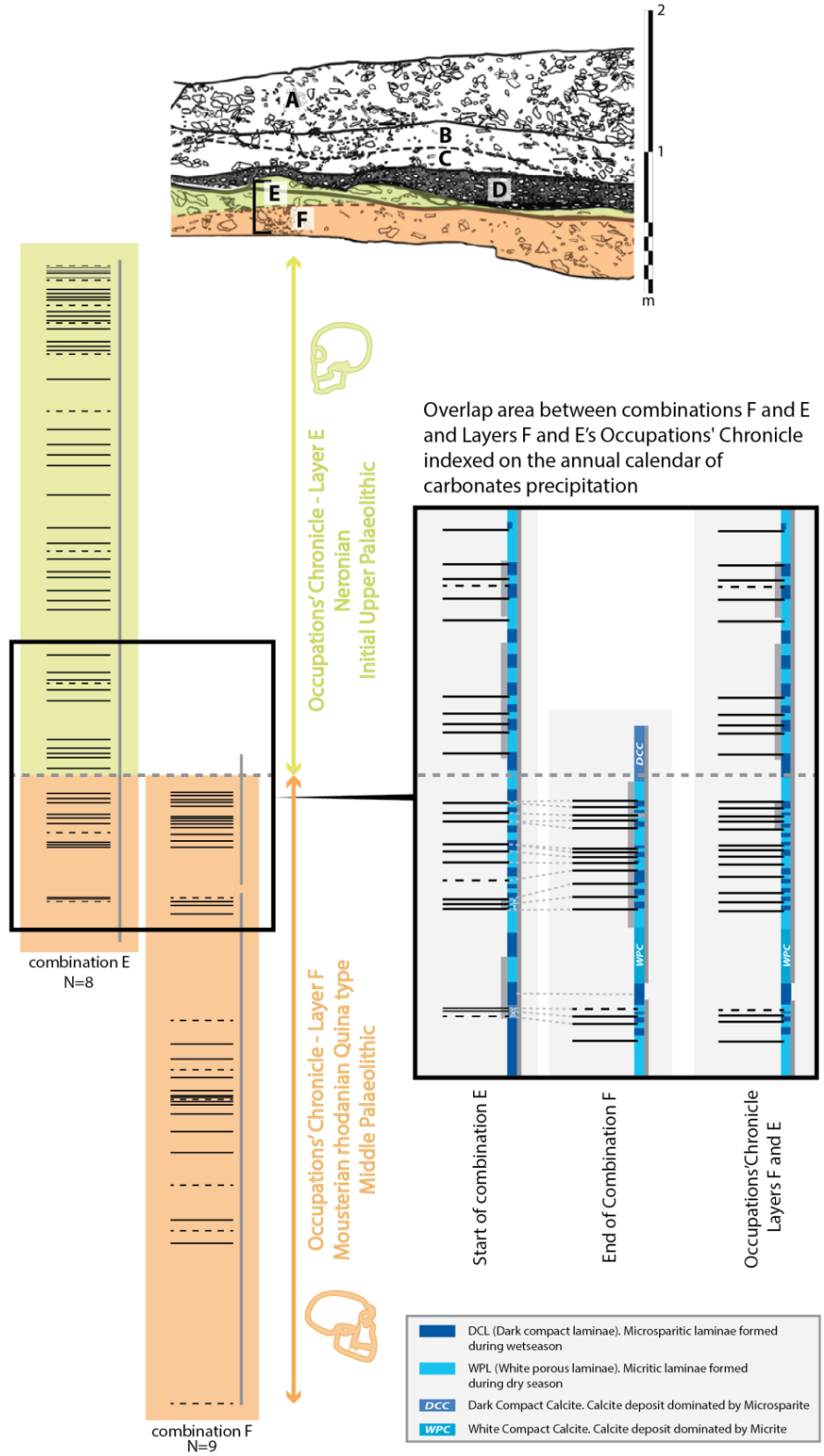

Fig. S25. Transition between Layers F and E at Grotte Mandrin. ***Top:*** **Focus on the upper part of the Mandrin's stratigraphy (Layers F to A)**, with the critical period of replacement of the Rhodanian Quina Mousterian group (Layer F, orange) by the Neronian group (Layer E, green).

Left: **Combination sequences of Layers F and E** constructed by matching of respectively 9 and 8 individual sequences. Barcodes represent succession of soot film from the oldest (bottom) to youngest (top). Bars represent soot films and dashed lines represent probable soot films. The long grey shading under the barcodes represents speleothem thickness. Soot films at the beginning of E combination sequence overlap with the end of F combination sequence. E can bear soot films recorded during F period because of the progressive crumbling of walls but E occupations can't be recorded in F sequence because the clasts have already fallen before the Neronian (Layer E) occupations. Therefore, the overlaid soot films in E combination can be attributed to F. The occupations chronicle of Layer E is highlighted in green and occupations chronicle of layer F in orange.

Right: **Zoom on the transition period and indexation on the annual calendar of carbonate precipitation**. Thin section observations allowed the indexing of the sequences by recording each soot film's position *vis-à-vis* the calcite doublets represented here in blue (dark blue for DCL and light blue for WPL). In some locations carbonates didn't deposit as legible calcite doublets but rather as White Porous Calcite (WCC, dominated by micrite) or as Dark Compact Calcite (DCC, dominated by microsparite), represented here in two other shades of blue. For locations where there is some uncertainty regarding the exact position of soot films a grey bar is added to the calcite doublets drawn in blue. Layers F and E Occupations Chronicle indexing was made by matching of Layers F and E Combination sequences. Confident information (without grey bar) is privileged (the grey bar is therefore removed) and the remaining uncertainties are reported on the chronicle (grey bar is conserved). The indexed chronicle of occupations shows reliably that a single doublet formed between the last occupation of chronicle F and the first occupation of chronicle E.

Table S1. Radiocarbon dates from Grotte Mandrin. ** Not used in the Bayesian model due to uncertainties about precise context and sample coordinates. * Some doubt regarding precise context, outlier probability in model increased to 0.25. ¶ sample coming from the edge of the wall, outlier probability increased to 0.25. # coordinated sample but presence of burrows, outlier probability increased to 0.25.

OxA/OxA-X	Context	Material and comments	^{14}C age BP	± value	fM	± value
2286-9#	B1	Bone fragment (cut)	38900	1100	0.0079	0.0011
22118	B1	Artiodactyl	31050	400	0.02102	0.00106
2352-51	B1	Unidentified bone	32950	650	0.01651	0.00138
21684*	B1	Bovid metatarsal with cutmarks	37400	900	0.00946	0.00102
2283-11#	B1	Unidentified bone	35150	650	0.01259	0.00105
22120	B2 PN2	Cut bone fragment	43400	1800	0.00448	0.00102
2286-10¶	B2 PN2	Humeral shaft fragment, small bovid size. Cutmarks.	38500	1000	0.00832	0.00101
21690¶	B2 PN2	Cut and scraped bone fragment	41700	1400	0.0056	0.00098
22121	B3 PN2	Cut bone fragment	40300	1200	0.00666	0.00098
21685**	B	Cut diaphyseal fragment	39000	1000	0.00781	0.001
21691¶	C1 PN2	Horse tooth fractured by human activity Upper cheek tooth	45300	2200	0.00354	0.00096
2286-13	C1 PN2	Retoucher cf. bovid limb metatarsal fragment	43200	2000	0.00463	0.00113
2286-14	C2	Retoucher artiodactyl limb fragment	42800	1800	0.00485	0.00108
21698	D Niv.5	Bone with cutmarks	47000	2700	0.00288	0.00097
21694	D test pit	Retoucher cf. reindeer femur	>47100		0.00097	0.00094
2286-15	E Niv. 6	*Cervus elaphus* mandibular ascending ramus with cutmarks	>49000		0.00029	0.00097
21692	E. Niv.6	Retoucher on horse tibia	>47300		0.00088	0.00095
21693	E. Niv.6	Retoucher on horse tibia, cut and smashed	>48600		0.00048	0.00094
21695	F test pit	Retoucher with cutmarks and impact (ascending ramus fragment of a bovid or horse sized animal?)	>48200		0.00061	0.00093
21696	F test pit	Cut bone small artiodactyl small radius	>49900		0.00015	0.00093
2287-24	G test pit	Broken horse tooth humanly fractured	>48000		0	0.00126
21697	G test pit	Cut bone distal femoral articulation horse/bovid sized	>45400		0.00163	0.00094
21701	G test pit	Bone with cutmarks	>45200		0.00172	0.00095

Table S2. Analytical data for the radiocarbon dates from the Mousterian, Neronian and post-Neronian levels at Grotte Mandrin. Stable isotope ratios of carbon and nitrogen are shown in ‰ relative to VPDB and AIR with a mass spectrometric precision of ±0.2‰ and ±0.3‰ respectively. Yield represents the weight of ion-exchanged gelatin in milligrams. %Yld is the percent yield of extracted gelatin as a function of the starting weight of the bone analyzed. Used is the weight of bone used (in mg). %C is the carbon present in the combusted gelatin and ought to be ~40-43%.

OxA	P	Pretreat Code	Used (mg)	Yield (mg)	%Yld	%C	$\delta^{13}C$ (‰)	$\delta^{15}N$ (‰)	C/N atomic ratio
22118	26554	AF	880	7.3	0.8	44.4	-19.1	4.3	3.2
2352-51	26555	AF	490	2.7	0.6	44.7	-19.9	3.5	3.3
21684	22272	AF	1120	38.7	3.5	41.1	-20.5	4.5	3.3
2283-11	22270	AF	880	5.48	0.6	41.0	-19.5	3.4	3.3
22120	26558	AF	510	5.9	1.2	44.8	-20.9	1.5	3.2
2286-10	22278	AF	830	5.34	0.6	44.5	-19.5	0.0	3.3
21690	22279	AF	840	33.2	4	43.5	-20.5	0.0	3.3
2286-9	22277	AF	560	4.09	0.7	42.6	-20.7	0.0	3.3
2286-14	22286	AF	620	4.16	0.7	43.4	-18.9	3.7	3.3
22121	26559	AF	704	26.9	3.8	45.1	-21.3	3.4	3.2
21685	22273	AF	540	9.52	1.8	41.8	-19.8	2.3	3.3
21691	22283	AF	640	9.1	1.4	47.1	-20.3	5.1	3.3
2286-13	22285	AF	610	3.71	0.6	44.1	-20.1	3.9	3.2
21698	22302	AF	620	7.68	1.2	46.1	-19.5	3.4	3.3
21694	22294	AF	600	12.57	2.1	46.3	-19.5	6.6	3.4
2286-15	22289	AF	610	5.5	0.9	45.5	-18.1	3.8	3.4

21692	22290	AF	700	8.58	1.2	47.4	-19.2	4.7	3.3
21693	22291	AF	620	10.35	1.7	47.1	-19.8	3.3	3.3
21695	22295	AF	610	20.91	3.4	46.6	-19.7	4.8	3.3
21696	22296	AF	610	19.71	3.2	47.7	-18.5	4.1	3.4
2287-24	22301	AF	600	3.02	0.5	41.4	-20.0	2.9	3.2
21697	22300	AF	520	18.94	3.6	45.7	-19.9	2.0	3.4
21701	22300	AF	620	20.66	3.3	45	-19.9	2.3	3.3

Table S3. Output of the Bayesian model. The results are rounded to 50 years.

Name	Unmodelled (BP)						Modelled (BP)						Indices Amodel 41.6 Aoverall 49.9		
	from	to	%	from	to	%	from	to	%	from	to	%	Acomb	A	C
End Proto-Aurignacian							35940	33920	68.3	36750	31030	95.4			95.4
OxA-X-2286-9	43780	42100	68.3	44620	41650	95.4	42880	41870	68.3	43650	40140	95.4		101.6	98.5
OxA-22118	35930	34920	68.3	36200	34610	95.4	36130	35200	68.3	37000	34450	95.4		92	98.7
OxA-X-2283-11	40940	39680	68.3	41650	39130	95.4	40990	39610	68.3	41870	38880	95.4		101.1	98.9
OxA-2352-51	38660	36720	68.3	39450	36180	95.4	38950	36740	68.3	39570	36150	95.4		99.2	98.9
OxA-21684	42410	41460	68.3	42900	40880	95.4	42360	41370	68.3	42930	40420	95.4		102.1	98.7
B1 Proto-Aurignacian															
Sterile/B1 Proto-Aurignacian							43320	42250	68.3	44060	41570	95.4			99.8
End Post-Neronian 2/Start Sterile							43970	42830	68.3	44580	42300	95.4			99.3

OxA-21690	45650	43220	68.3	47790	42670	95.4	44290	43170	68.3	44970	42820	95.4		116	99.7
X6717	45000	41070	68.3	46840	39230	95.4	44300	43130	68.3	45040	42650	95.4		127.1	99.9
OxA-X-2286-10	43040	41980	68.3	44150	41470	95.4	44220	43110	68.3	44770	42570	95.4		38.9	99.7
OxA-22120	48230	44470	68.3	52090	43170	95.4	44360	43170	68.3	45100	42870	95.4		45.7	99.7
B2 Mousterian PN2															
Start B2							44680	43350	68.3	45530	43000	95.4			99.3
End C1/B3							45440	43840	68.3	46580	43340	95.4			99.6
OxA-22121	44360	42760	68.3	45580	42300	95.4	45880	44210	68.3	47020	43650	95.4		43.3	99.6
B3 Mousterian PN2															
End C1/Start B3							47080	44820	68.3	48340	44080	95.4			99.3
X6718	50100	46380	68.3	51840	44630	95.4	48360	46160	68.3	49590	45220	95.4		110.4	100
OxA-21691	50780	45630	68.3	55000	44920	95.4	48270	46020	68.3	49600	45190	95.4		126.1	99.6
OxA-X-2286-13	48330	44220	68.3	52330	42930	95.4	48080	45810	68.3	49370	44900	95.4		113.9	99.6
C1 PN2															
End C2/Start C1							49620	46930	68.3	50880	45860	95.4			99.2

MAN19-3	53580	50280	68.3	55140	48730	95.4	50920	48520	68.3	52050	47450	95.4		62.1	100
OxA-X-2286-14	47740	44100	68.3	51280	42860	95.4	50300	47700	68.3	51700	46670	95.4		41.9	99.5
C2															
Start C2 Post Neronian							51720	49120	68.3	52890	47870	95.4			99.2
End of D/Sterile boundary							52970	50440	68.3	54100	49180	95.4			99.1
							48010	47990	68.3	48010	47990	95.4			100
	...	-46050	68.3	…	-46050	95.4	-98050	-46050	68.3	-98050	-46050	95.4		100	
							1E+05	99990	68.3	1E+05	99990	95.4			100
	-98050	…	68.3	-98050	...	95.4	-98050	-46050	68.3	-98050	-46050	95.4		100	
	100000	48000	68.3	100000	48000	95.4	53690	51260	68.3	54870	50080	95.4	100		98.3
X6719	53090	49990	68.3	54540	48530	95.4	53490	51250	68.3	54540	50170	95.4		104.1	100
D Niv 5															
D Niv 5/E Niv 6							54520	52010	68.3	55850	50810	95.4			99.2
							49010	48990	68.3	49010	48990	95.4			100
	...	0	68.3	...	-47050	95.4	-98050	-47050	68.3	-98050	-47050	95.4		100	

							1E+05	99990	68.3	1E+05	99990	95.4			100
	-98050	...	68.3	-98050	...	95.4	-98050	-47050	68.3	-98050	-47050	95.4		100	
	100000	49000	68.3	100000	49000	95.4	55450	52880	68.3	56760	51730	95.4	100		98.3
MAN19-4	56600	53060	68.3	58270	51400	95.4	55410	53040	68.3	56630	51970	95.4		113.5	100
Neronian E							55430	52870	68.3	56800	51700	95.4			99.6
E Niv 6 Neronian															
OSL date to E Niv 6							56430	53670	68.3	57880	52490	95.4			99
X6720 base E	56500	52570	68.3	58340	50730	95.4	57380	54710	68.3	58810	53490	95.4		93.2	100
End F to OSL date							59940	55890	68.3	61780	54370	95.4			98.8
MAN19-6	63770	59890	68.3	65600	58070	95.4	62960	59620	68.3	64740	58150	95.4		104.6	100
MAN19-5	62480	58580	68.3	64320	56750	95.4	62290	59070	68.3	63930	57520	95.4		108.8	100
X6721	62000	51280	68.3	67040	46230	95.4	62670	58030	68.3	65640	55800	95.4		102.2	100
F Quina Mousterian															
F/G							67570	60190	68.3	74370	59370	95.4			96
X7381	77190	73270	68.3	79040	71430	95.4	76440	72890	68.3	78110	71050	95.4		101.6	100

G Ferrassie Mousterian															
EndH/Start G Ferrassie Mousterian							79770	75310	68.3	81650	73230	95.4			97.7
X6723	89860	81810	68.3	93640	78030	95.4	81000	77130	68.3	82680	75260	95.4		36.6	99.9
X6761	98080	74790	68.3	109040	63830	95.4	80900	76710	68.3	82820	74570	95.4		111.3	99.9
H															
End I/Start H							81800	78050	68.3	83430	76210	95.4			98.7
End J/Start I							83010	79750	68.3	84510	78080	95.4			98.6
X6714	84900	80360	68.3	87040	78230	95.4	83720	80630	68.3	85370	79110	95.4		114.8	99.7
X6713	82800	78260	68.3	84940	76130	95.4	83570	80480	68.3	85110	79000	95.4		99.6	99.8
J															
Start J							84840	80980	68.3	87150	79400	95.4			81.8
Grotte Mandrin sequence															

Table S4. Chemistry of sediment samples and dose rates to quartz grains used in the multiple-grain OSL analyses.

Sample ID	Year	Lyr	Grain size (µm)	Chemical concentrations			Dose rate (Gy.ka^{-1}) [a]			
				U (eq. ppm)	Th (eq. ppm)	K (%)	Beta	Gamma [b]	Cosmic [c]	Total [d]
X 6717	2014	B2	90-250	2.2 ± 0.1	6.2 ± 0.3	0.84 ± 0.04	0.89 ± 0.06	0.50 ± 0.07	0.13 ± 0.02	1.56 ± 0.10
X 6718	2014	C	125-250	2.3 ± 0.1	6.9 ± 0.4	0.78 ± 0.04	0.87 ± 0.06	0.47 ± 0.07	0.13 ± 0.01	1.49 ± 0.09
X 6719	2014	D	180-250	2.2 ± 0.1	4.9 ± 0.3	0.63 ± 0.03	0.72 ± 0.05	0.48 ± 0.08	0.12 ± 0.02	1.34 ± 0.09
X 6720	2014	E(/F)	180-250	1.6 ± 0.1	4.3 ± 0.2	0.67 ± 0.03	0.67 ± 0.04	0.49 ± 0.04	0.11 ± 0.01	1.29 ± 0.05
X 6721	2014	F top	180-250	1.6 ± 0.1	4.8 ± 0.2	0.69 ± 0.03	0.69 ± 0.04	0.47 ± 0.09	0.10 ± 0.01	1.29 ± 0.10
X 6723	2014	H	125-250	2.8 ± 0.1	5.9 ± 0.3	0.58 ± 0.03	0.78 ± 0.05	0.51 ± 0.06	0.10 ± 0.01	1.42 ± 0.08
X 6761	2015	H	125-250	1.6 ± 0.1	4.8 ± 0.2	0.57 ± 0.03	0.62 ± 0.04	0.46± 0.07	0.10 ± 0.01	1.22 ± 0.09
X 6760	2015	I	180-250	2.6 ± 0.1	2.5 ± 0.1	0.28 ± 0.01	0.49 ± 0.03	0.23 ± 0.06	0.10 ± 0.01	0.85 ± 0.07

[a] Dose rates were calculated using DRAC v.1.2 (*194*) with the following parameters: conversion factors from ref. *92* and beta-dose attenuation from ref. *93*. The internal dose rate is 0.03 ± 0.02 Gy.ka^{-1}, and external dose rates include adjustments for the water content (12 ± 5%).

[b] Gamma dose rate were determined from the dose recorded by in situ dosimeters buried for 396 days at the sample location, except for sample X6720, for which the gamma dose rates was calculated from the concentrations of potassium (K), uranium (U) and thorium (Th) within the sediment.

[c] Cosmic-ray dose rates were calculated using the approach of refs. *96 & 118* and assigned a relative uncertainty of ±10%.

[d] Mean ± total uncertainty (1σ) calculated as the quadratic sum of the random and systematic uncertainties.

Table S5. Multiple-grain OSL measurements, doses and ages of the sediment samples collected in 2014-2015.

Sample ID	Layer	n [a]	D_e (Gy) [b]	OD (%) [c]	OSL age (ka) [d]
X 6717	B2	19(20)	67.0 ± 2.8	18 ± 3	43.1 ± 3.2 (1.9)
X 6718	C	19(22)	72.1 ± 2.5	15 ± 3	48.3 ± 3.5 (1.8)
X 6719	D	21(27)	69.1 ± 1.9	12 ± 2	51.6 ± 3.9 (1.5)
X 6720	E(/F)	17(18)	70.5 ± 2.4	11 ± 2	54.6 ± 2.9 (1.9)
X 6721	F top	22(22)	73.4 ± 6.7	27 ± 4	56.7 ± 6.9 (5.2)
X 6723	H	14(14)	122 ± 5.3	15 ± 4	85.9 ± 6.3 (3.9)
X 6761	H	14(17)	106 ± 13.7	26 ± 6	86.5 ± 12.8 (11.3)
X 6760	I	0(7)	-	-	-

[a] 'n' is the number of aliquots that passed the selection criteria (recuperation, recycling, IR depletion) and used for the calculation of the average dose; the total number of aliquots tested is in brackets.
[b] Equivalent dose (D_e) is expressed as an unweighted mean with a standard error.
[c] Overdispersion (OD) was calculated using the central age model (*137*).
[d] Ages are reported in 10^3 years (ka) and the uncertainty shown after the ± symbol is the quadratic sum of the random and systematic uncertainties at 1σ; values shown in brackets are the random-only errors (used for Bayesian modelling purposes).

Table S6. Single-aliquot regenerative-dose (SAR) procedures used to measure single-grain OSL D_e values for the 2019 luminescence samples. Each of these SAR measurement cycles was repeated for the natural dose, 5 different sized regenerative doses and a 0 Gy regenerative-dose (to measure OSL signal recuperation). Both the smallest and largest non-zero regenerative-dose cycles were repeated at the end of the SAR procedure to assess the suitability of the test-dose sensitivity correction. The smallest regenerative-dose cycle was also repeated a second time with the inclusion of step 2 to check for the presence of feldspar contaminants using the OSL IR depletion ratio of ref. *88*. L_x = regenerative dose signal response; L_n = natural dose signal response; T_x = test dose signal response for a laboratory dose cycle T_n = test dose signal response for the natural dose cycle.

Single-grain OSL SAR procedure 2019 samples		
Step	**Treatment**	**Symbol**
1	Dose (Natural or laboratory)	N or D
2 [a]	IRSL stimulation (50ºC for 60 s)	
3	Preheat 1 (240ºC for 10 s)	PH_1
4	Single-grain OSL stimulation (125ºC for 2 s)	L_n or L_x
5	Test dose (20 Gy)	T_d
6	Preheat 2 (240ºC for 10 s)	PH_2
7	Single-grain OSL stimulation (125ºC for 2 s)	T_n or T_x
8	Repeat measurement cycle for different sized regenerative doses	

[a] Step 2 is only included in the single-grain SAR procedure when measuring the OSL IR depletion ratio (*102*).

Table S7. Single-grain OSL classification statistics for the dose recovery and natural D_e measurements of the 2019 luminescence samples. The proportion of grains that were rejected from final D_e estimation after applying the various SAR quality assurance criteria are shown in rows 5-13. These criteria were applied to each single-grain measurement in the order listed. T_n = natural test dose signal response; L_n/T_n = sensitivity-corrected natural signal response; L_x/T_x = sensitivity-corrected regenerative-dose signal response; I_{max} = saturation OSL intensity of the fitted dose response curve.

Sample name	**MAN19-3**	**MAN19-4**	**MAN19-4**	**MAN19-5**	**MAN19-6**
SAR measurement type	OSL D_e	OSL D_e	OSL dose-recovery	OSL D_e	OSL D_e
Total measured grains (*n*)	2100	2300	1300	2300	2300
Grains rejected for failing SAR quality assurance criteria (%)					
T_n <3σ background	59	52	55	58	54
Low−dose recycling ratio ≠ 1 at ±2σ	4	5	4	4	4
High−dose recycling ratio ≠ 1 at ±2σ	3	4	3	3	4
OSL-IR depletion ratio <1 at ±2σ	5	5	4	5	4
0 Gy L_x/T_x >5% L_n/T_n	<1	<1	<1	<1	<1
Non-intersecting grains (L_n/T_n > dose response curve saturation)	<1	<1	<1	0	<1
Saturated grains (L_n/T_n ≥ dose response curve I_{max} at ±2σ)	<1	<1	<1	<1	<1
Extrapolated grains (L_n/T_n values >2σ beyond largest L_x/T_x value)	0	0	0	0	<1
Anomalous dose response / unable to perform Monte Carlo fit	16	21	22	17	20
Sum of rejected grains (%)	87	86	89	87	87
Sum of accepted grains (%)	13	14	11	13	13

Table S8. Single-grain OSL dating results for the 2019 luminescence samples.

Sample name	Layer	Grain size (μm)	Water content [a]	Environmental dose rate (Gy/ka)				D_e (Gy) [f,h]	OSL age (ka) [f,i]
				Beta dose rate [b,c]	Gamma dose rate [c,d]	Cosmic dose rate [e]	Total dose rate [c,f,g]		
MAN19-3	C	212 – 250	2 / 9	0.78 ± 0.04	0.45 ± 0.02	0.12 ± 0.01	1.39 ± 0.07	72.5 ± 1.4	52.0 ± 2.9 (1.6)
MAN19-4	E	212 – 250	3 / 10	0.63 ± 0.03	0.39 ± 0.02	0.11 ± 0.01	1.16 ± 0.06	63.9 ± 1.2	54.9 ± 3.1 (1.7)
MAN19-5	F	212 – 250	2 / 10	0.64 ± 0.03	0.41 ± 0.02	0.10 ± 0.01	1.18 ± 0.06	71.6 ± 1.3	60.6 ± 3.5 (1.9)
MAN19-6	F	212 – 250	2 / 12	0.62 ± 0.03	0.40 ± 0.02	0.14 ± 0.01	1.19 ± 0.06	73.5 ± 1.4	61.9 ± 3.7 (1.9)

[a] Present-day water content / long-term estimated water content, expressed as % of dry mass of mineral fraction, with an assigned relative uncertainty of ±25%. The long-term water content of these samples is taken as 50% of the saturated water content estimate based on a range of proportional saturation water content assessments made on analogous sediments in the site surroundings.
[b] Beta dose rates were calculated on dried and powdered sediment samples using a Risø GM-25-5 low-level beta counter (*114*), after making allowance for beta dose attenuation due to grain-size effects and HF etching (*116*).
[c] Specific activities and radionuclide concentrations have been converted to dose rates using the conversion factors given in ref. *92*, making allowance for beta-dose attenuation (*116, 126*).
[d] Gamma dose rates were calculated from in situ measurements made at each sample position with a NaI:Tl detector, using the 'energy windows' approach (*113*).
[e] Cosmic-ray dose rates were calculated using the approach of refs. *96* & *118* and assigned a relative uncertainty of ±10%.
[f] Mean ± total uncertainty (68% confidence interval), calculated as the quadratic sum of the random and systematic uncertainties.
[g] Includes an internal dose rate of 0.03 Gy/ka with an assigned relative uncertainty of ±30%, based on intrinsic ^{238}U and ^{232}Th contents published in refs. *119-123*, and an a-value of 0.04 ±0.01 (*124, 125*).
[h] The final De values of these samples have been calculated using the central age model (CAM; *137*). See Table S6 and single-grain quartz OSL dating section for further details.
[i] Total uncertainty includes a systematic component of ±2% associated with laboratory beta-source calibration. The dating uncertainties shown outside parentheses represent the total (random plus systematic) 1σ range for each sample, whereas those shown in parentheses represent the random 1σ dating uncertainties only. The latter have been used for Bayesian modelling purposes.

Table S9. Single-grain OSL D_e summary statistics and age model results for the 2019 luminescence samples.

Sample	Layer	Total dose rate (Gy / ka)	No of D_e values[a]	Over-dispersion (%)[b]	Weighted skewness value[c]	Critical skewness 95% C.I.[c]	Age Model[d,e]	L_{max} score[f]	D_e (Gy)[g]	OSL age (ka)[g,h,i]
MAN19-3	C	1.39 ± 0.07	267 / 2100	22 ± 2	0.19	±0.30	CAM	-70.9	72.5 ± 1.4	**52.0 ± 2.9**
							MAM-3	-70.7	71.0 ± 4.4	51.0 ± 4.2
							MAM-4	-70.7	71.2 ± 6.0	51.1 ± 5.1
MAN19-4	E	1.16 ± 0.06	320 / 2300	20 ± 2	-0.20	±0.27	CAM	-125.8	63.9 ± 1.2	**54.9 ± 3.1**
							MAM-3	-124.5	62.4 ± 1.2	53.5 ± 3.1
							MAM-4	-124.4	62.6 ± 1.6	53.7 ± 3.2
MAN19-5	F	1.18 ± 0.06	308 / 2300	23 ± 2	-0.03	±0.28	CAM	-91.4	71.6 ± 1.3	**60.6 ± 3.5**
							MAM-3	-92.2	64.1 ± 4.6	54.3 ± 4.9
							MAM-4	-90.5	46.2 ± 6.1	39.1 ± 5.6
MAN19-6	F	1.19 ± 0.06	296 / 2300	21 ± 2	-0.13	±0.28	CAM	-111.5	73.5 ± 1.4	**61.9 ± 3.7**
							MAM-3	-111.1	72.6 ± 3.5	61.2 ± 4.6
							MAM-4	-111.1	71.2 ± 4.2	60.0 ± 4.9

[a] Number of D_e measurements that passed the SAR rejection criteria / total number of grains analyzed.
[b] The relative spread in the D_e dataset beyond that associated with the measurement uncertainties of individual D_e values, calculated using the central age model (*137*).

[c] Weighted skewness scores have been calculated on log-transformed D_e values using Eq. 7-8 of ref. *134*. Critical skewness scores have been calculated using Eq. 16 of ref. *135*. Critical skewness values are taken to be equivalent to twice the standard error of skewness score (95% C.I.) for single-grain D_e datasets, following the results of sensitivity analyses performed by refs. *106 & 135*.

[d] CAM = central age model; MAM-3 = 3-parameter minimum age model; MAM-4 = 4-parameter minimum age model (*137*).

[e] MAM-3 and MAM-4 D_e estimates were calculated after adding, in quadrature, a relative error of 20% to each individual D_e measurement error to approximate the underlying dose overdispersion observed in the well-bleached and unmixed sedimentary samples from this site and from global overdispersion datasets (*134*).

[f] Maximum log likelihood score of the CAM, MAM-3, MAM-4 and FMM fit. For a given sample, the L_{max} score of the MAM-3 is expected to be substantially higher (i.e. at least 1.92 greater) than that of the CAM when the addition of the extra model parameter improves the fit to the data. Likewise, the L_{max} score of the MAM-4 is expected to be significantly greater than that of the MAM-3 (by at least 1.92 when compared with the 95% C.I. of a X^2 distribution) when the addition of the extra model parameter improves the fit to the data. If the extra parameter of the MAM-3 (or MAM-4) is not supported by the data, then its L_{max} score will be similar to (i.e. within 1.92 of) the CAM (or MAM-3) L_{max} score, indicating that the simpler age model explains the data equally well (*107*).

[g] Total uncertainty includes a systematic component of ±2% associated with laboratory beta-source calibration.

[h] The preferred final age is shown in bold. For these samples, the final age has been derived using the statistical age model (CAM, MAM-3 or MAM-4) that yielded the optimum L_{max} score, following the criterion outlined in footnote [f] and ref. *107*.

[i] Mean ±total uncertainty (68% confidence interval), calculated as the quadratic sum of the random and systematic uncertainties. Total uncertainty includes a systematic component of ± 2% associated with laboratory beta-source calibration.

Table S10. Radioisotopic contents, dose rates and TL ages for the burnt flint samples.

		Radioisotopic content			S alpha	Dose rate (Gy.ka^{-1}) [a]					D_e (Gy)	TL Age (ka) [b]
Sample ID	**Lyr**	**U (ppm)**	**Th (ppm)**	**K (ppm)**		**Alpha**	**Beta**	**Gamma**	**Cosmic**	**Total**		
X 7381	G	0.65 ± 0.03	0.04 ± 0.01	90 ± 5	2.21E-08 ± 2.21E-09	0.24 ± 0.03	0.10 ± 0.01	0.37± 0.08	0.10 ± 0.01	0.71 ± 0.033	53.0 ± 1.1	75.3 ± 3.8 (1.9)
X 6713	J	0.78 ± 0.04	0.04 ± 0.01	45 ± 2	1.32E-08 ± 1.32E-09	0.174 ± 0.02	0.12 ± 0.01	0.40 ± 0.02	0.10± 0.01	0.80 ± 0.031	63.7 ± 1.5	80.6 ± 3.7 (2.2)
X 6714	J	2.04 ± 0.10	0.03 ± 0.01	276 ± 14	1.82E-08 ± 1.82E-09	0.62 ± 0.07	0.32 ± 0.02	0.40 ± 0.02	0.10 ± 0.01	1.44 ± 0.08	118.9 ± 2.8	82.7 ± 4.7 (2.2)

[a] External dose rates include adjustments for the water content.
[b] Mean ± total uncertainty (68% confidence interval), calculated as the quadratic sum of the random (in brackets) and systematic uncertainties.

Table S11. Technical lithic categories by archaeological layers at Grotte Mandrin. MH, modern humans; Mouster., Mousterian; NEA, Neanderthals; Protoaur., Protoaurignacian.

Geological layer	**I**		**H**		**G**		**F**		**E**		**D**		**C2**		**C1**		**B3**		**B2**		**B1**		**Total by categories**
Cultural attributions	**Levallois Mouster.**		**Mouster.**		**Ferrassie Mouster.**		**Quina Mouster.**		**Neronian**		**P-N I Mouster.**		**P-N II Mouster.**		**P-N II Mouster.**		**P-N II Mouster.**		**P-N II Mouster.**		**Protoa ur.**		
Anthropological remains	**NEA**		**/**		**NEA**		**NEA**		**MH**		**NEA**		**NEA**		**NEA**		**NEA**		**/**		**/**		
Anthropological attributions	**NEA**		**NEA**		**NEA**		**NEA**		MH		**NEA**		**NEA**		**NEA**		**NEA**		**NEA**		MH		
	N	%	N	%	N	%	N	%	N	%	N	%	N	%	N	%	N	%	N	%	N	%	**N**
Flakes	823	75.6	107	65.6	252	67.4	661	67.1	525	21.2	789	45.3	2486	72.9	1059	67.6	1076	65.1	799	65.3	12	1.1	**8589**
Pseudo-Levallois points	16	1.5	20	12.3	16	4.3	32	3.2			433	24.8	263	7.7	183	11.7	238	14.4	132	10.8			**1333**
Kombewa flakes	3	0.3	3	1.8	11	2.9	8	0.8			70	4.0	39	1.1	17	1.1	34	2.1	11	0.9			**196**
Levallois blanks	17	1.6	5	3.1	27	7.2	29	2.9			9	0.5	59	1.7	35	2.2	39	2.4	18	1.5			**238**
Unretouched Points	12	1.1	2	1.2	1	0.3	8	0.8	638	**25.8**	12	0.7	8	0.2	15	1.0	20	1.2	2	0.2			**718**
Unretouched Micropoints	18	1.7			2	0.5	1	0.1	142	**5.7**	4	0.2					2	0.1	2	0.2			**171**
Unretouched Nanopoints					2	0.5			39	**1.6**							1	0.1					**42**

Blades	6	0.6	4	2.5	3	0.8	32	3.2	346	**14.0**	14	0.8	39	1.1	20	1.3	24	1.5	18	1.5	100	9.2	**606**
Bladelets	60	5.5			6	1.6	15	1.5	415	**16.8**	17	1.0	39	1.1	16	1.0	27	1.6	33	2.7	247	22.7	**875**
Retouched tools	65	6.0	12	7.4	43	11.5	138	14.0	162	6.5	141	8.1	174	5.1	145	9.3	99	6.0	79	6.5	13	1.2	**1071**
Cores	25	2.3	9	5.5	9	2.4	38	3.9	182	7.3	134	7.7	115	3.4	55	3.5	58	3.5	24	2.0	9	0.8	**658**
Lithic fragments	44	4.0			2	0.5	16	1.6	7	0.3	101	5.8	164	4.8	15	1.0	24	1.5	97	7.9			**470**
Pebbles			1	0.6			7	0.7	21	0.8	19	1.1	24	0.7	7	0.4	11	0.7	8	0.7	1	0.1	**99**
tiny flakes below 2cm	**4575**		**428**		**1058**		**1917**		**6582**		**4971**		**11187**		**5613**		**4519**		**3276**		**146**		**44272**
Total by level ≥2cm	**1089**	100	**163**	100	**374**	100	**985**	100	**2477**	100	**1743**	100	**3410**	100	**1567**	100	**1653**	100	**1223**	100	**382**	35.1	**15066**
Synthetic data																							
Density lithic ≥2cm by m²	545		82		187		99		50		35		68		31		33		24		8		
All lithic blanks	955		141		320		786		2105		1348		2933		1345		1461		1015		372		
% Blades+bladelets+points	96	10.1	6	4.3	14	4.4	56	7.1	1580	75.1	47	3.5	86	2.9	51	3.8	74	5.1	55	5.4	347	93.3	
% retouched tools		6.4		7.8		11.8		14.8		6.9		9.5		5.6		9.7		6.3		7.2		3.5	

Table S12. Sequencing summary statistics obtained from PALEOMIX after Illumina sequencing of DNA extracted from six equid teeth. The percentage of high-quality unique reads mapping to the horse reference sequence is indicated in the *%HQUniqEndogenous* column.

Lyr	Seq. Lib. ID	mg	Super natar.	#Read Pairs	#Collapsed	Raw Endog.	%Raw Endog.	% Clonality	HQUniq Endog.	%HQUniq Endog.	Covmt DNA	Length MtDNA	ConvnucDNA	Length nucDNA
B	MandrinB1x1644xE1_AMIS_1_00985	60	E1	1828471	1686279	191	0.01%	0.00%	191	0.01%	-	NA	2.08E-06	27.08
	MandrinB1x1644xE2_AMIS_1_00985		E2	904374	830667	111	0.01%	0.00%	111	0.01%	-	NA	1.45E-06	32.43
C	MandrinC1x1193xE1_AMIS_1_00991	70	E1	914529	839527	126	0.01%	0.00%	126	0.01%	-	NA	1.37E-06	27.08
	MandrinC1x1193xE2_AMIS_1_00991		E2	1035011	938041	222	0.02%	0.00%	222	0.02%	-	NA	2.43E-06	27.27
D	MandrinD1x2623xE1_AMIS_1_01000	50	E1	1252580	1159277	282	0.02%	1.06%	279	0.02%	-	NA	4.36E-06	38.86
	MandrinD1x2623xE2_AMIS_1_01000		E2	822705	751505	112	0.01%	0.00%	112	0.01%	-	NA	1.35E-06	30.02
E	Mandrin10xE8x794xE1	60	E1	494831	412001	330	0.07%	0.30%	329	0.07%	0.0026	44	5.22E-06	39.62
	Mandrin10xE8x794xE2_AMIS_1_01015		E2	683796	535809	52	0.01%	0.00%	52	0.01%	-	NA	7.41E-06	35.46
F	MandrinF1x1474xE1_AMIS_1_01016	40	E1	823069	714339	152	0.02%	0.00%	152	0.02%	-	NA	1.86E-06	30.43
	MandrinF1x1474xE2_AMIS_1_01016		E2	743699	635328	124	0.02%	0.00%	124	0.02%	-	NA	1.44E-06	28.92
G	MandrinG2x1742xE1_AMIS_1_01020	60	E1	693582	631237	418	0.06%	0.48%	416	0.06%	-	NA	5.97E-06	35.68
	MandrinG2x1742xE2_AMIS_1_01020		E2	983881	822978	193	0.02%	0.52%	192	0.02%	-	NA	2.65E-06	34.29

Table S13. Pleistocene and Holocene human comparative samples used for the crown mesiodistal and buccolingual measurements (*75, 76, 195, 196*). Ldm2, deciduous lower second molar; LM1, permanent lower first molar; LM3, permanent lower third molar; Udm2, deciduous upper second molar; NEA, Neanderthals; UPMH, Upper Pleistocene modern humans; HH, Holocene humans.

Specimen	Site (Country)	Tooth	Group
Amud 3	Amud (Israel)	Udm2	NEA
Dederiyeh 1	Dederiyeh (Syria)	Udm2	NEA
Dederiyeh 2	Dederiyeh (Syria)	Udm2	NEA
Kebara 1	Kebara (Israel)	Udm2	NEA
Kebara 25	Kebara (Israel)	Udm2	NEA
Shanidar 7	Shanidar (Iraq)	Udm2	NEA
Arcy-Renne 26	Grotte du Renne (France)	Udm2	NEA
Aubesier 7	Bau de l'Aubesier (France)	Udm2	NEA
Carihuela	Carihuela (Spain)	Udm2	NEA
Cavallo C	Cavallo (Italy)	Udm2	NEA
Chateauneuf 2	Chateauneuf (France)	Udm2	NEA
Cova Negra 42175	Cova Negra (Spain)	Udm2	NEA
Devil's Tower	Devil's Tower (UK)	Udm2	NEA
Engis 2	Engis (Belgium)	Udm2	NEA
La Ferrassie 8	La Ferrassie (France)	Udm2	NEA
Kulna 3	Kulna (Czech)	Udm2	NEA
Roc de Marsal	Roc de Marsal (France)	Udm2	NEA
Palomas 36	Palomas (Spain)	Udm2	NEA
Pech-Aze	Pech-de-l'Azé (France)	Udm2	NEA
Quina_18	La Quina (France)	Udm2	NEA
Quina 36	La Quina (France)	Udm2	NEA
Ehringsdorf 7	Ehringsdorf (Germany)	Udm2	NEA
Krapina mxA	Krapina (Croatia)	Udm2	NEA
Krapina mxB	Krapina (Croatia)	Udm2	NEA
Krapina mxC	Krapina (Croatia)	Udm2	NEA
Krapina mxG	Krapina (Croatia)	Udm2	NEA
Krapina mxR	Krapina (Croatia)	Udm2	NEA

Krapina 188	Krapina (Croatia)	Udm2	NEA
Figuier	Figuier (France)	Udm2	UPMH
Laugerie-Basse	Laugerie-Basse (France)	Udm2	UPMH
L-B 903	Laugerie-Basse (France)	Udm2	UPMH
L-B 904	Laugerie-Basse (France)	Udm2	UPMH
La Madeleine 4	La Madeleine (France)	Udm2	UPMH
DV 36	Dolní Vestonice (Czech)	Udm2	UPMH
Grotte des Enfants 6	Grotte des Enfants (France)	Udm2	UPMH
Kostenki 3	Kostenki (Russia)	Udm2	UPMH
Labatut	Labatut (France)	Udm2	UPMH
LV 1	Lagar Velho (Portugal)	Udm2	UPMH
Paglicci 27	Paglicci (Italy)	Udm2	UPMH
Abri Pataud 2	Abri Pataud (France)	Udm2	UPMH
Abri Pataud 3	Abri Pataud (France)	Udm2	UPMH
Abri Pataud 6	Abri Pataud (France)	Udm2	UPMH
Pavlov 6	Pavlov (Czech)	Udm2	UPMH
Pavlov 12	Pavlov (Czech)	Udm2	UPMH
La Rochette 5	La Rochette (France)	Udm2	UPMH
Sunghir 3	Sunghir (Russia)	Udm2	UPMH
Brassempouy 3625	Brassempouy (France)	Udm2	UPMH
Ksar Akil 1	Ksar Akil (Lebanon)	Udm2	UPMH

Qafzeh 4	Qafzeh (Israel)	Udm2	UPMH
Qafzeh 10	Qafzeh (Israel)	Udm2	UPMH
Qafzeh 12	Qafzeh (Israel)	Udm2	UPMH
Qafzeh 15	Qafzeh (Israel)	Udm2	UPMH
Qafzeh 21	Qafzeh (Israel)	Udm2	UPMH
Skhul 1	Skhul (Israel)	Udm2	UPMH
La Chaise 13	La Chaise-de-Vouthon Abri Suard (France)	Ldm2	NEA
La Chaise 14	La Chaise-de-Vouthon Abri Suard (France)	Ldm2	NEA
Krapina 62	Krapina (Croatia)	Ldm2	NEA
Krapina 63	Krapina (Croatia)	Ldm2	NEA
Krapina 64	Krapina (Croatia)	Ldm2	NEA
Krapina 65	Krapina (Croatia)	Ldm2	NEA
Krapina 66	Krapina (Croatia)	Ldm2	NEA
Krapina 68	Krapina (Croatia)	Ldm2	NEA
Krapina C	Krapina (Croatia)	Ldm2	NEA
Couvin	Couvin (Belgium)	Ldm2	NEA
Engis 2	Engis (Belgium)	Ldm2	NEA
Scladina 4A-13	Scladina (Belgium)	Ldm2	NEA
Châteauneuf 2	Châteauneuf (France)	Ldm2	NEA
Châteauneuf 2	Châteauneuf (France)	Ldm2	NEA
Pech de l'Azé	Pech de l'Azé (France)	Ldm2	NEA
Roc de Marsal	Roc de Marsal (France)	Ldm2	NEA
Roc de Marsal	Roc de Marsal (France)	Ldm2	NEA
Combe-Grenal	Combe-Grenal (France)	Ldm2	NEA
Gibraltar 2	Gibraltar (Gibraltar)	Ldm2	NEA
Hortus II	Hortus (France)	Ldm2	NEA
Hortus II	Hortus (France)	Ldm2	NEA
Archi 1	Archi (Italy)	Ldm2	NEA

Archi 1	Archi (Italy)	Ldm2	NEA
Teshik-Tash	Teshik-Tash (Uzbekistan)	Ldm2	NEA
Teshik-Tash	Teshik-Tash (Uzbekistan)	Ldm2	NEA
Cova Negra CN 7755	Cova Negra (Spain)	Ldm2	NEA
Salemas	Salemas (Portugal)	Ldm2	NEA
Ehringsdorf	Ehringsdorf (Germany)	Ldm2	NEA
La Ferrassie 4 bis	La Ferrassie (France)	Ldm2	NEA
La Ferrassie 8	La Ferrassie (France)	Ldm2	NEA
Cavallo A	Grotta Cavallo (Italy)	Ldm2	NEA
Zaskalnaya	Zaskalnaya (Crimea)	Ldm2	NEA
Arcy-sur-Cure 29	Arcy-sur-Cure (France)	Ldm2	NEA
Barakai	Barakai (Russia)	Ldm2	NEA
Dereriyeh 1	Dereriyeh (Syria)	Ldm2	NEA
Dereriyeh 2	Dereriyeh (Syria)	Ldm2	NEA
Dereriyeh 2	Dereriyeh (Syria)	Ldm2	NEA
Shanidar 7	Shanidar (Iraq)	Ldm2	NEA
Amud III	Amud (Israel)	Ldm2	NEA
Kebara KMH1	Kebara (Israel)	Ldm2	NEA
Kebara KMH4	Kebara (Israel)	Ldm2	NEA
Tabun series IV	Tabun (Israel)	Ldm2	NEA
Skhul I	Skhul (Israel)	Ldm2	UPMH
Skhul I	Skhul (Israel)	Ldm2	UPMH
Skhul X	Skhul (Israel)	Ldm2	UPMH
Qafzeh 21	Qafzeh (Israel)	Ldm2	UPMH
Qafzeh 12	Qafzeh (Israel)	Ldm2	UPMH
Qafzeh 10	Qafzeh (Israel)	Ldm2	UPMH
Qafzeh 10	Qafzeh (Israel)	Ldm2	UPMH
Qafzeh 4	Qafzeh (Israel)	Ldm2	UPMH

Qafzeh 4	Qafzeh (Israel)	Ldm2	UPMH
Qafzeh 15	Qafzeh (Israel)	Ldm2	UPMH
Qafzeh 15	Qafzeh (Israel)	Ldm2	UPMH
Brassempouy 69	Brassempouy (France)	Ldm2	UPMH
Les Rois 1A	Les Rois (France)	Ldm2	UPMH
Les Rois R50/33	Les Rois (France)	Ldm2	UPMH
Fontéchevade 2	Fontéchevade (France)	Ldm2	UPMH
Cueva del Castillo 2	Cueva del Castillo (Spain)	Ldm2	UPMH
La Quina 761	La Quina (France)	Ldm2	UPMH
Bacho Kiro 559	Bacho Kiro (Bulgaria)	Ldm2	UPMH
Grotte des Enfants 1	Grotte des Enfants (France)	Ldm2	UPMH
Grotte des Enfants 1	Grotte des Enfants (France)	Ldm2	UPMH
Krapina 80	Krapina (Croatia)	LM1	NEA
Krapina D/D	Krapina (Croatia)	LM1	NEA
Krapina F/H	Krapina (Croatia)	LM1	NEA
Krapina F/H	Krapina (Croatia)	LM1	NEA
Krapina MND C	Krapina (Croatia)	LM1	NEA
Krapina MND E	Krapina (Croatia)	LM1	NEA
Krapina MND E	Krapina (Croatia)	LM1	NEA
Krapina MND G	Krapina (Croatia)	LM1	NEA
Krapina MND J	Krapina (Croatia)	LM1	NEA
Krapina MND J	Krapina (Croatia)	LM1	NEA
Krapina MND M	Krapina (Croatia)	LM1	NEA
Krapina MND P	Krapina (Croatia)	LM1	NEA
Krapina MND Q	Krapina (Croatia)	LM1	NEA
Krapina N/N	Krapina (Croatia)	LM1	NEA

Krapina R64 = MND L	Krapina (Croatia)	LM1	NEA
Amud 1	Amud (Israel)	LM1	NEA
Amud 1	Amud (Israel)	LM1	NEA
Kebara 2	Kebara (Israel)	LM1	NEA
Kebara 2	Kebara (Israel)	LM1	NEA
Scla 4A-1/M_1	Scladina (Belgium)	LM1	NEA
Scla 4A-9/M_1	Scladina (Belgium)	LM1	NEA
BD1	La Chaise-de-Vouthon Abri Bourgeois Delaunay (France)	LM1	NEA
BD1	La Chaise-de-Vouthon Abri Bourgeois Delaunay (France)	LM1	NEA
La Quina 9	La Quina (France)	LM1	NEA
Montgaudier mandible	Montgaudier (France)	LM1	NEA
M-G2-419	Moula-Guercy (France)	LM1	NEA
M-D1-230	Moula-Guercy (France)	LM1	NEA
M-L4-TNN5	Moula-Guercy (France)	LM1	NEA
Subalyuk 1	Subalyuk (Hungary)	LM1	NEA
Subalyuk 1	Subalyuk (Hungary)	LM1	NEA
Le Fate 6	Le Fate (Italy)	LM1	NEA
Le Fate 2	Le Fate (Italy)	LM1	NEA
Fossellone 3	Fossellone (Italy)	LM1	NEA
Taddeo 4	Taddeo (Italy)	LM1	NEA
PN11	Pontnewydd (UK)	LM1	NEA
Qafzeh 7	Qafzeh (Israel)	LM1	UPMH
Qafzeh 7	Qafzeh (Israel)	LM1	UPMH
Qafzeh 8	Qafzeh (Israel)	LM1	UPMH
Qafzeh 9	Qafzeh (Israel)	LM1	UPMH
Qafzeh 9	Qafzeh (Israel)	LM1	UPMH
DV3	Dolní Vestonice (Czech)	LM1	UPMH

DV3	Dolní Vestonice (Czech)	LM1	UPMH
DV13	Dolní Vestonice (Czech)	LM1	UPMH
DV13	Dolní Vestonice (Czech)	LM1	UPMH
DV15	Dolní Vestonice (Czech)	LM1	UPMH
DV15	Dolní Vestonice (Czech)	LM1	UPMH
DV14	Dolní Vestonice (Czech)	LM1	UPMH
DV14	Dolní Vestonice (Czech)	LM1	UPMH
Mladeč 54	Mladeč (Czech)	LM1	UPMH
Mladeč 54	Mladeč (Czech)	LM1	UPMH
Mladeč 52	Mladeč (Czech)	LM1	UPMH
Mladeč 52	Mladeč (Czech)	LM1	UPMH
Pavlov 1	Pavlov (Czech)	LM1	UPMH
Pavlov 1	Pavlov (Czech)	LM1	UPMH
Předmost 259	Předmost (Czech)	LM1	UPMH
Předmost 3070	Předmost (Czech)	LM1	UPMH
Předmost 4	Předmost (Czech)	LM1	UPMH
Předmost 4	Předmost (Czech)	LM1	UPMH
Předmost 1	Předmost (Czech)	LM1	UPMH
Předmost 1	Předmost (Czech)	LM1	UPMH
Předmost 26	Předmost (Czech)	LM1	UPMH
Předmost 27	Předmost (Czech)	LM1	UPMH

Předmost 27	Předmost (Czech)	LM1	UPMH
Předmost 476	Předmost (Czech)	LM1	UPMH
Předmost 476	Předmost (Czech)	LM1	UPMH
Předmost 3	Předmost (Czech)	LM1	UPMH
Předmost 3	Předmost (Czech)	LM1	UPMH
Předmost 9	Předmost (Czech)	LM1	UPMH
Předmost 9	Předmost (Czech)	LM1	UPMH
Předmost 14	Předmost (Czech)	LM1	UPMH
Předmost 14	Předmost (Czech)	LM1	UPMH
Předmost 18	Předmost (Czech)	LM1	UPMH
Předmost 18	Předmost (Czech)	LM1	UPMH
Předmost 7	Předmost (Czech)	LM1	UPMH
Předmost 10	Předmost (Czech)	LM1	UPMH
Předmost 10	Předmost (Czech)	LM1	UPMH
Předmost 5	Předmost (Czech)	LM1	UPMH
Předmost 5	Předmost (Czech)	LM1	UPMH
Abri Pataud P1	Abri Pataud (France)	LM1	UPMH
Abri Pataud P1	Abri Pataud (France)	LM1	UPMH
Cap Blanc 1	Cap Blanc (France)	LM1	UPMH
Cap Blanc 1	Cap Blanc (France)	LM1	UPMH
Les Rois A	Les Rois (France)	LM1	UPMH

Les Rois A	Les Rois (France)	LM1	UPMH
Les Rois R51.16	Les Rois (France)	LM1	UPMH
Les Rois 55.148b	Les Rois (France)	LM1	UPMH
Les Vachons 1	Les Vachons (France)	LM1	UPMH
L.B. II	Grotte de la Balauzière (France)	LM1	UPMH
L.B. III	Grotte de la Balauzière (France)	LM1	UPMH
L.B. IV	Grotte de la Balauzière (France)	LM1	UPMH
L.B. VIII	Grotte de la Balauzière (France)	LM1	UPMH
Mas d'Azil 902	Mas d'Azil (France)	LM1	UPMH
Mas d'Azil 902	Mas d'Azil (France)	LM1	UPMH
La Madeleine 24835	La Madeleine (France	LM1	UPMH
Saint Germain La Rivière B31970.8	Saint Germain La Rivière (France)	LM1	UPMH
Saint Germain La Rivière B31970.8	Saint Germain La Rivière (France)	LM1	UPMH
Saint Germain La Rivière 4	Saint Germain La Rivière (France)	LM1	UPMH
Saint Germain La Rivière B41970.8	Saint Germain La Rivière (France)	LM1	UPMH
Arene Candide 1	Arene Candide (Italy)	LM1	UPMH
Arene Candide 5	Arene Candide (Italy)	LM1	UPMH
Arene Candide 2	Arene Candide (Italy)	LM1	UPMH
Arene Candide 4	Arene Candide (Italy)	LM1	UPMH
Arene Candide 20	Arene Candide (Italy)	LM1	UPMH
Arene Candide 20	Arene Candide (Italy)	LM1	UPMH

Arene Candide 19.6725	Arene Candide (Italy)	LM1	UPMH
Arene Candide 19.6725	Arene Candide (Italy)	LM1	UPMH
Barma Grande 2	Barma Grande (Italy)	LM1	UPMH
Barma Grande 2	Barma Grande (Italy)	LM1	UPMH
Barma Grande 5	Barma Grande (Italy)	LM1	UPMH
Barma Grande 4	Barma Grande (Italy)	LM1	UPMH
Barma Grande 4	Barma Grande (Italy)	LM1	UPMH
Grotte des Enfants 6	Grotte des Enfants (France)	LM1	UPMH
Grotte des Enfants 6	Grotte des Enfants (France)	LM1	UPMH
Paglicci 12	Paglicci (Italy)	LM1	UPMH
Paglicci 12	Paglicci (Italy)	LM1	UPMH
Paglicci 20.d.G	Paglicci (Italy)	LM1	UPMH
Romanelli R7	Romanelli (Italy)	LM1	UPMH
Romanelli R8	Romanelli (Italy)	LM1	UPMH
Romito 1	Romito (Italy)	LM1	UPMH
Romito 1	Romito (Italy)	LM1	UPMH
Romito 4	Romito (Italy)	LM1	UPMH
Romito 4	Romito (Italy)	LM1	UPMH
Romito 3	Romito (Italy)	LM1	UPMH
Romito 6	Romito (Italy)	LM1	UPMH
Romito 6	Romito (Italy)	LM1	UPMH

Romito 2	Romito (Italy)	LM1	UPMH
LKH 1	Lakonis (Greece)	LM3	NEA
Shovakh 1	Shovakh (Israel)	LM3	NEA
Kebara 2	Kebara (Israel)	LM3	NEA
Kebara 2	Kebara (Israel)	LM3	NEA
Krapina 8	Krapina (Croatia)	LM3	NEA
Krapina 9	Krapina (Croatia)	LM3	NEA
Krapina 78	Krapina (Croatia)	LM3	NEA
Krapina F/H	Krapina (Croatia)	LM3	NEA
Krapina F/H	Krapina (Croatia)	LM3	NEA
Krapina MND E	Krapina (Croatia)	LM3	NEA
Krapina MND E	Krapina (Croatia)	LM3	NEA
Krapina MND G	Krapina (Croatia)	LM3	NEA
Krapina MND J	Krapina (Croatia)	LM3	NEA
Krapina MND K	Krapina (Croatia)	LM3	NEA
Krapina MND M	Krapina (Croatia)	LM3	NEA
Krapina R63	Krapina (Croatia)	LM3	NEA
Krapina R64 = MND L	Krapina (Croatia)	LM3	NEA
Krapina R64 = MND L	Krapina (Croatia)	LM3	NEA
P7-647-76	Grotte du Bison (France)	LM3	NEA
BD1	La Chaise-de-Vouthon Abri Bourgeois Delaunay (France)	LM3	NEA
BD1	La Chaise-de-Vouthon Abri Bourgeois Delaunay (France)	LM3	NEA
La Quina 9	La Quina (France)	LM3	NEA
C.G. 2D3, n°2.671	Montmaurin (France)	LM3	NEA
M-G2-419	Moula-Guercy (France)	LM3	NEA
Subalyuk	Subalyuk (Hungary)	LM3	NEA
Subalyuk	Subalyuk (Hungary)	LM3	NEA
Shanidar 1	Shanidar (Iraq)	LM3	NEA
Shanidar 1	Shanidar (Iraq)	LM3	NEA
Shanidar 2	Shanidar (Iraq)	LM3	NEA

Shanidar 2	Shanidar (Iraq)	LM3	NEA
Shanidar 4	Shanidar (Iraq)	LM3	NEA
Shanidar 6	Shanidar (Iraq)	LM3	NEA
Amud 1	Amud (Israel)	LM3	NEA
Amud 1	Amud (Israel)	LM3	NEA
Le Fate 3	Le Fate (Italy)	LM3	NEA
PN16	Pontnewydd (UK)	LM3	NEA
PN21	Pontnewydd (UK)	LM3	NEA
Qafzeh 7	Qafzeh (Israel)	LM3	UPMH
Qafzeh 8	Qafzeh (Israel)	LM3	UPMH
Qafzeh 9	Qafzeh (Israel)	LM3	UPMH
Qafzeh 9	Qafzeh (Israel)	LM3	UPMH
DV3	Dolní Vestonice (Czech)	LM3	UPMH
DV13	Dolní Vestonice (Czech)	LM3	UPMH
DV13	Dolní Vestonice (Czech)	LM3	UPMH
DV15	Dolní Vestonice (Czech)	LM3	UPMH
DV15	Dolní Vestonice (Czech)	LM3	UPMH
Mladeč 52	Mladeč (Czech)	LM3	UPMH
Pavlov 1	Pavlov (Czech)	LM3	UPMH
Předmost 3070	Předmost (Czech)	LM3	UPMH
Předmost 4	Předmost (Czech)	LM3	UPMH
Předmost 4	Předmost (Czech)	LM3	UPMH
Předmost 26	Předmost (Czech)	LM3	UPMH
Předmost 27	Předmost (Czech)	LM3	UPMH

Předmost 3	Předmost (Czech)	LM3	UPMH
Předmost 3	Předmost (Czech)	LM3	UPMH
Předmost 9	Předmost (Czech)	LM3	UPMH
Předmost 9	Předmost (Czech)	LM3	UPMH
Předmost 10	Předmost (Czech)	LM3	UPMH
Předmost 10	Předmost (Czech)	LM3	UPMH
Abri Blanchard	Abri Blanchard (France)	LM3	UPMH
Abri Pataud P1	Abri Pataud (France)	LM3	UPMH
Abri Pataud P1	Abri Pataud (France)	LM3	UPMH
R50.27	Les Rois (France)	LM3	UPMH
R50.3	Les Rois (France)	LM3	UPMH
L.B. XII	Grotte de la Balauzière (France)	LM3	UPMH
Arene Candide 5	Arene Candide (Italy)	LM3	UPMH
Arene Candide 5	Arene Candide (Italy)	LM3	UPMH
Arene Candide 2	Arene Candide (Italy)	LM3	UPMH
Arene Candide 2	Arene Candide (Italy)	LM3	UPMH
Arene Candide 4	Arene Candide (Italy)	LM3	UPMH
Arene Candide 4	Arene Candide (Italy)	LM3	UPMH
Arene Candide 20	Arene Candide (Italy)	LM3	UPMH
Arene Candide 20	Arene Candide (Italy)	LM3	UPMH
Arene Candide 19.6725	Arene Candide (Italy)	LM3	UPMH

Arene Candide 19.6725	Arene Candide (Italy)	LM3	UPMH
Barma Grande 2	Barma Grande (Italy)	LM3	UPMH
Barma Grande 5	Barma Grande (Italy)	LM3	UPMH
Grotte des Enfants 4	Grotte des Enfants (France)	LM3	UPMH
Grotte des Enfants 4	Grotte des Enfants (France)	LM3	UPMH
Romanelli R5	Romanelli (Italy)	LM3	UPMH
Romanelli R7	Romanelli (Italy)	LM3	UPMH
Romito 1	Romito (Italy)	LM3	UPMH
Romito 1	Romito (Italy)	LM3	UPMH
Romito 5	Romito (Italy)	LM3	UPMH
Romito 5	Romito (Italy)	LM3	UPMH
Romito 4	Romito (Italy)	LM3	UPMH
Romito 4	Romito (Italy)	LM3	UPMH
Romito 3	Romito (Italy)	LM3	UPMH
Romito 6	Romito (Italy)	LM3	UPMH
Romito 6	Romito (Italy)	LM3	UPMH
Romito 2	Romito (Italy)	LM3	UPMH
Romito 2	Romito (Italy)	LM3	UPMH

Table S14. Pleistocene and Holocene human comparative samples used for the geometric morphometric analyses of the crown outline and enamel-dentine junction (EDJ) shape. Ldm2, deciduous lower second molar; LM1, permanent lower first molar; Udm2, deciduous upper second molar; NEA, Neanderthals; UPMH, Upper Pleistocene modern humans; HH, Holocene humans (including specimens from the Neolithic to the 20th century); unp: unpublished

Specimen	Site (Country)	Tooth	Group	Analysis	Ref
D185	Krapina (Croatia)	Udm2	NEA	outline	*197*
D186	Krapina (Croatia)	Udm2	NEA	outline	*197*
D187	Krapina (Croatia)	Udm2	NEA	outline	*197*
D188	Krapina (Croatia)	Udm2	NEA	outline	*197*
D189	Krapina (Croatia)	Udm2	NEA	outline	*197*
Chateauneuf 2	Chateauneuf (France)	Udm2	NEA	outline	unp
Ferrassie ULdm2	La Ferrassie (France)	Udm2	NEA	outline	unp
Ferrassie URdm2	La Ferrassie (France)	Udm2	NEA	outline	unp
Pech de l'Azé ULdm2	Pech de l'Azé (France)	Udm2	NEA	outline	unp
Pech de l'Azé URdm2	Pech de l'Azé (France)	Udm2	NEA	outline	unp
Roc de Marsal ULdm2	Roc de Marsal (France)	Udm2	NEA	outline	*197*
Roc de Marsal URdm2	Roc de Marsal (France)	Udm2	NEA	outline	*197*
La Quina 18 ULdm2	La Quina (France)	Udm2	NEA	outline	unp
La Quina18 URdm2	La Quina (France)	Udm2	NEA	outline	unp
Gibraltar2	Gibraltar (Gibraltar)	Udm2	NEA	outline	*198*
La Tannerie	La Tannerie (France)	Udm2	UPMH	outline	unp
Pataud 230b	Abri Pataud (France)	Udm2	UPMH	outline	unp
Pataud 236	Abri Pataud (France)	Udm2	UPMH	outline	unp
Cavallo C	Grotta Cavallo (Italy)	Udm2	UPMH	outline	unp
Qafzeh 4 ULdm2	Qafzeh (Israel)	Udm2	UPMH	outline	unp
Qafzeh 4 URdm2	Qafzeh (Israel)	Udm2	UPMH	outline	unp
Qafzeh 10	Qafzeh (Israel)	Udm2	UPMH	outline	*198*
Qafzeh 15 ULdm2	Qafzeh (Israel)	Udm2	UPMH	outline	*198*
Qafzeh 15 URdm2	Qafzeh (France)	Udm2	UPMH	outline	*198*
18 specimens	France	Udm2	HH	outline	*199,200*,unp
Archi LLdm2	Archi (Italy)	Ldm2	NEA	outline	unp
Archi LRdm2	Archi (Italy)	Ldm2	NEA	outline	unp

Cavallo A	Grotta Cavallo (Italy)	Ldm2	NEA	outline	unp
D62	Krapina (Croatia)	Ldm2	NEA	outline	*197*
D63	Krapina (Croatia)	Ldm2	NEA	outline	*197*
D64	Krapina (Croatia)	Ldm2	NEA	outline	*197*
D65	Krapina (Croatia)	Ldm2	NEA	outline	*197*
D66	Krapina (Croatia)	Ldm2	NEA	outline	*197*
D68	Krapina (Croatia)	Ldm2	NEA	outline	*197*
Ferrassie	La Ferrassie (France)	Ldm2	NEA	outline	unp
Gibraltar 2	Gibraltar (Gibraltar)	Ldm2	NEA	outline	*198*
Le Fate 5	Le Fate (Italy)	Ldm2	NEA	outline	unp
Molare LLdm2	Molare (Italy)	Ldm2	NEA	outline	unp
Molare LRdm2	Molare (Italy)	Ldm2	NEA	outline	unp
Roc de Marsal LLdm2	Roc de Marsal (France)	Ldm2	NEA	outline	*197*
Roc de Marsal LRdm2	Roc de Marsal (France)	Ldm2	NEA	outline	*197*
S14-5	La Chaise-de-Vouthon Abri Suard (France)	Ldm2	NEA	outline	*197*
S37 LLdm2	La Chaise-de-Vouthon Abri Suard (France)	Ldm2	NEA	outline	*197*
S37 LRdm2	La Chaise-de-Vouthon Abri Suard (France)	Ldm2	NEA	outline	*197*
LV1	Lagar Velho (Portugal)	Ldm2	UPMH	outline	*197*
La Madeleine 4 LLdm2	La Madeleine (France)	Ldm2	UPMH	outline	*197*
La Madeleine 4 LRdm2	La Madeleine (France)	Ldm2	UPMH	outline	*197*
Pataud 230b LLdm2	Abri Pataud (France)	Ldm2	UPMH	outline	unp
Pataud230b LRdm2	Abri Pataud (France)	Ldm2	UPMH	outline	unp
Qafzeh 4 LLdm2	Qafzeh (Israel)	Ldm2	UPMH	outline	unp
Qafzeh 4 LRdm2	Qafzeh (Israel)	Ldm2	UPMH	outline	unp
Qafzeh 10	Qafzeh (Israel)	Ldm2	UPMH	outline	*198*
Qafzeh 15 LLdm2	Qafzeh (Israel)	Ldm2	UPMH	outline	*198*
Qafzeh 15 LRdm2	Qafzeh (Israel)	Ldm2	UPMH	outline	*198*
20 specimens	France	Ldm2	HH	outline	*199,200*,unp
D185	Krapina (Croatia)	Udm2	NEA	EDJ	*197*
D186	Krapina (Croatia)	Udm2	NEA	EDJ	*197*

D187	Krapina (Croatia)	Udm2	NEA	EDJ	*197*
D188	Krapina (Croatia)	Udm2	NEA	EDJ	*197*
D189	Krapina (Croatia)	Udm2	NEA	EDJ	*197*
Chateauneuf 2	Chateauneuf (France)	Udm2	NEA	EDJ	unp
Ferrassie ULdm2	La Ferrassie (France)	Udm2	NEA	EDJ	unp
Ferrassie URdm2	La Ferrassie (France)	Udm2	NEA	EDJ	unp
Pech de l'Azé ULdm2	Pech de l'Azé (France)	Udm2	NEA	EDJ	unp
Pech de l'Azé URdm2	Pech de l'Azé (France)	Udm2	NEA	EDJ	unp
Roc de Marsal ULdm2	Roc de Marsal (France)	Udm2	NEA	EDJ	*197*
Roc de Marsal URdm2	Roc de Marsal (France)	Udm2	NEA	EDJ	*197*
Gibraltar 2	Gibraltar (Gibraltar)	Udm2	NEA	EDJ	*198*
La Tannerie	La Tannerie (France)	Udm2	UPMH	EDJ	unp
Pataud 230b	Abri Pataud (France)	Udm2	UPMH	EDJ	unp
Pataud 236	Abri Pataud (France)	Udm2	UPMH	EDJ	unp
Qafzeh 4 ULdm2	Qafzeh (Israel)	Udm2	UPMH	EDJ	unp
Qafzeh 4 URdm2	Qafzeh (Israel)	Udm2	UPMH	EDJ	unp
Qafzeh 10	Qafzeh (Israel)	Udm2	UPMH	EDJ	*198*
Qafzeh 15 ULdm2	Qafzeh (Israel)	Udm2	UPMH	EDJ	*198*
Qafzeh 15 URdm2	Qafzeh (Israel)	Udm2	UPMH	EDJ	*198*
25 specimens	France and UK	Udm2	HH	EDJ	*199,200*,unp
BD-J4-C9	La Chaise-de-Vouthon Abri Bourgeois-Delaunay (France)	LM1	NEA	EDJ	*197*
S14-7	La Chaise-de-Vouthon Abri Suard (France)	LM1	NEA	EDJ	*197*
S49	La Chaise-de-Vouthon Abri Suard (France)	LM1	NEA	EDJ	*197*
S5	La Chaise-de-Vouthon Abri Suard (France)	LM1	NEA	EDJ	*197*
D105	Krapina (Croatia)	LM1	NEA	EDJ	*197*
D77	Krapina (Croatia)	LM1	NEA	EDJ	*197*
D79	Krapina (Croatia)	LM1	NEA	EDJ	*197*
D80	Krapina (Croatia)	LM1	NEA	EDJ	*197*
D81	Krapina (Croatia)	LM1	NEA	EDJ	*197*
Ehringsdorf I 1048	Ehringsdorf (Germany)	LM1	NEA	EDJ	*197*

EQ5	Equus Cave (South Africa)	LM1	UPMH	EDJ	*198*
EQ8	Equus Cave (South Africa)	LM1	UPMH	EDJ	*198*
LV1	Lagar Velho (Portugal)	LM1	UPMH	EDJ	*197*
Qafzeh 4 LLM1	Qafzeh (Israel)	LM1	UPMH	EDJ	unp
Qafzeh 4 LRM1	Qafzeh (Israel)	LM1	UPMH	EDJ	unp
Qafzeh 10	Qafzeh (Israel)	LM1	UPMH	EDJ	*198*
Qafzeh 15 LLM1	Qafzeh (Israel)	LM1	UPMH	EDJ	*198*
Qafzeh 15 LRM1	Qafzeh (Israel)	LM1	UPMH	EDJ	*198*
13 specimens	France	LM1	HH	EDJ	*201*,unp

Table S15. Tooth crown diameters of the Mandrin specimens compared with those of three chrono-geographic human groups from Europe and Middle East (*75, 76, 195, 196*). Ldm2, deciduous lower second molar; LM1, permanent lower first molar; LM3, permanent lower third molar; Udm2, deciduous upper second molar; NEA, Neanderthals; UPMH, Upper Pleistocene modern humans; HH, Holocene humans.

	N	MD (mm)	sd	N	BL (mm)	sd
Layer C -Ldm2						
Man11 C 204	1	10.7		1	9.4	
NEA	42	10.4	0.6	42	9.3	0.5
UPMH	19	10.7	0.6	20	9.5	0.6
HH	73	9.8	1.7	73	8.7	1.5
Layer C - LM3						
Man02 C 983	1	12.1		1	10.6	
NEA	37	12.0	0.7	36	11.0	0.6
UPMH	54	10.9	1.1	55	10.6	0.9
HH	185	10.6	0.7	185	10.4	0.7
Layer D - Udm2						
Man04 D 395	1	9.3		1	11.1	
Man04 D 679	1	9.3		1	10.9	
NEA	26	9.7	0.7	28	10.5	0.5
UPMH	14	9.5	0.8	26	10.4	0.6
HH	202	9.2	0.5	213	9.4	0.8
Layer F - LM1						
Man98 F 811	1	11.2		1	10.0	
NEA	35	11.8	0.8	34	11.0	0.7
UPMH	90	11.5	0.7	90	10.9	0.7
HH	174	11.4	0.6	174	11.0	0.5

Table S16. Statistics of the tooth crown diameters. Adjusted Z-score analysis of the mesiodistal and buccolingual of the Mandrin compared with Pleistocene and Holocene human samples from Europe and Middle East (*75, 76, 195, 197*). The values above or below 1, representing those outside of the 95% confidence interval of the comparative group variability, are highlighted in bold. Ldm2, deciduous lower second molar; LM1, permanent lower first molar; LM3, permanent lower third molar; Udm2, deciduous upper second molar; NEA, Neanderthals; UPMH, Upper Pleistocene modern humans; HH, Holocene humans.

Layer C - Ldm2	**MD (mm)**	**BL (mm)**
Man11 C 204 vs. NEA	0.27	0.07
Man11 C 204 vs. UPMH	-0.03	-0.05
Man11 C 204 vs. HH	0.25	0.23
Layer C - LM3		
Man02 C 983 vs. NEA	0.09	-0.28
Man02 C 983 vs. UPMH	0.54	-0.01
Man02 C 983 vs. HH	**1.05**	0.17
Layer D - Udm2		
Man04 D 395 vs. NEA	-0.27	0.54
Man04 D 395 vs. UPMH	-0.08	0.56
Man04 D 395 vs. HH	0.12	**1.14**
Man04 D 679 vs. NEA	-0.27	0.35
Man04 D 679 vs. UPMH	-0. 08	0.39
Man04 D 679 vs. HH	0.12	**1.01**
Layer F - LM1		
Man98 F 811 vs. NEA	-0.32	-0.72
Man98 F 811 vs. UPMH	-0.19	-0.66
Man98 F 811 vs. HH	-0.16	**-1.01**

Table S17. Lateral enamel thickness parameters. 3D-based tooth tissue proportion variables measured in the Mandrin specimens and compared with Pleistocene and Holocene human samples from Europe and Middle East (Table S12). Ldm2, deciduous lower second molar; LM1, permanent lower first molar; LM3, permanent lower third molar; Udm2, deciduous upper second molar; NEA, Neanderthals; UPMH, Upper Pleistocene modern humans; HH, Holocene humans.

	N	3D LAET (mm)	sd	N	3D LRET	sd
Layer C - Ldm2						
Man11 C 204	1	0.37			6.52	
NEA	12	0.35	0.06	12	6.24	1.06
UPMH	4	0.44	0.07	4	8.58	0.68
HH	14	0.42	0.06	14	7.88	1.40
Layer C - LM3						
Man02 C 983	1	0.77			12.21	
NEA	6	0.59	0.09	6	9.59	1.61
UPMH	1	0.49		1	7.93	
HH	7	0.52	0.11	7	9.11	1.56
Layer D - Udm2						
Man04 D 395	1	0.38			7.00	
Man04 D 679	1	0.42			7.99	
NEA	5	0.47	0.07	5	7.87	0.85
UPMH	5	0.51	0.06	5	9.88	0.77
HH	4	0.44	0.03	4	7.95	0.24
Layer F - LM1						
Man98 F 811	1	0.52		1	8.94	
NEA	10	0.58	0.11	10	8.67	1.30

UPMH	5	0.55	0.03	5	8.60	0.65
HH	13	0.56	0.09	13	9.73	1.06

Table S18. Statistics of the lateral enamel thickness parameters. Adjusted Z-score analysis of the three variables describing crown tissue proportions measured in the Mandrin teeth and compared with Pleistocene and Holocene human samples from Europe and Middle East (Table S12). The values above or below 1, representing those outside of the 95% confidence interval of the comparative group variability, are highlighted in bold. Ldm2, deciduous lower second molar; LM1, permanent lower first molar; LM3, permanent lower third molar; Udm2, deciduous upper second molar; NEA, Neanderthals; UPMH, Upper Pleistocene modern humans; HH, Holocene humans.

Layer C - Ldm2	**3D LAET (mm)**	**3D LRET**
Man11 C 204 vs. NEA	0.12	0.12
Man11 C 204 vs. UPMH	-0.31	-0.85
Man11 C 204 vs. HH	-0.37	-0.43
Layer C - LM3		
Man02 C 983 vs. NEA	0.72	0.59
Man02 C 983 vs. HH	0.86	0.76
Layer D - Udm2		
Man04 D 395 vs. NEA	-0.41	-0.33
Man04 D 395 vs. UPMH	-0.64	**-1.12**
Man04 D 395 vs. HH	-0.71	**-1.23**
Man04 D 679 vs. NEA	-0.23	0.05
Man04 D 679 vs. UPMH	-0.24	0.05
Man04 D 679 vs. HH	-0.49	-0.81
Layer F - LM1		
Man98 F 811 vs. NEA	-0.22	0.09
Man98 F 811 vs. UPMH	-0.29	0.17
Man98 F 811 vs. HH	-0.19	-0.33

Table S19. Root volumetric bifurcation index of Man02 C 983 and statistics. Root stem volume (Vstem; mm^3), root branch volume (Vbranch; mm^3), volumetric bifurcation index (VBI; %) and adjusted Z-scores (AZS; values above or below 1, representing those outside of the 95% confidence interval of the comparative group variability, are highlighted in bold) measured in the Mandrin LM3 Man02 C 983 and compared with Pleistocene and Holocene human samples from Europe, Africa and Middle East (*82*). NEA, Neanderthals; UPMH, Upper Pleistocene modern humans; HH, Holocene humans.

	N	**Vstem (mm^3)**	**sd**	**N**	**Vbranch (mm^3)**	**sd**	**N**	**VBI (%)**	**sd**	**AZS(Vstr)**	**AZS(Vbr)**	**AZS(VBI)**
Man02 C 983	1	379.76		1	61.76		1	86.01				
NEA	15	627.84	248.58	15	135.24	138.99	15	80.66	18.04	-0.45	-0.24	0.13
UPMH	8	403.45	61.65	8	235.50	115.67	8	64.62	15.11	-0.15	-0.60	0.56
HH	8	251.96	50.85	8	128.06	137.93	8	72.84	23.73	**1.00**	-0.19	0.22

Table S20. Results of the cross-validated between-group principal component analyses (bgPCA) for the 3D analyses of the EDJ shape. The leave-one-out cross-validation (CV) shows excellent predictive accuracy, with a clear discrimination between Neanderthals (NEA) and modern humans (MH), even if Upper Pleistocene modern (UPMH) and Holocene humans (HH) tend to overlap. The posterior probabilities that the Mandrin specimens are closer to any group (NEA, UPMH or HH) were then calculated. The highest probabilities are indicated in bold (the greater the number, the higher the probability). Ldm2, deciduous lower second molar; LM1, permanent lower first molar; Udm2, deciduous upper second molar; _geom, geometric-based reconstruction of the Mandrin specimens; _MH, modern human-based reconstruction of the Mandrin specimens; _NEA, Neanderthal-based reconstruction of the Mandrin specimens.

Layer	tooth	CV correct classification	posterior probability
C	Ldm2	UPMH: 68.4 %; HH: 33.3 % (MH: 92.3 %) NEA: 89.5 %	Man11 C 204: 0.001 UPMH; 0.016 HH; **0.701 NEA**
D	Udm2	UPMH: 66.7 %; HH: 61.1 % (MH: 100.0 %) NEA: 100.0 %	Man04 D 395: <0.001 UPMH; <0.001 HH; **0.590 NEA** Man04 D 679: <0.001 UPMH; <0.001 HH; **0.502 NEA**
E	Udm2	UPMH: 87.5 %; HH: 76.9 % (MH: 100.0 %) NEA: 92.3 %	Man12 E 1300_geom: **0.842 UPMH**; 0.070 HH; <0.001 NEA Man12 E 1300_MH: **0.870 UPMH**; 0.142 HH; 0.001 NEA Man12 E 1300_NEA: **0.952 UPMH**; 0.254 HH; <0.001 NEA
F	LM1	UPMH: 75.0 %; HH: 92.3 % (MH: 95.5 %) NEA: 70.0 %	Man98 F 811_geom: 0.008 UPMH; <0.001 HH; **0.381 NEA** Man98 F 811_MH: 0.004 UPMH; 0.012 HH; **0.890 NEA** Man98 F 811_NEA: 0.093 UPMH; 0.085 HH; **0.226 NEA**

Table S21. Results of the cross-validated canonical variates analyses (CVA) for the 3D analyses of the EDJ shape. The Jackknife cross-validation (CV) shows excellent predictive accuracy, with a clear discrimination between Neanderthals (NEA) and modern humans (MH), even if Upper Pleistocene modern (UPMH) and Holocene humans (HH) tend to overlap. The posterior probabilities that the Mandrin specimens belong to NEA, UPMH or HH were then calculated. Ldm2, deciduous lower second molar; LM1, permanent lower first molar; Udm2, deciduous upper second molar; _geom, geometric-based reconstruction of the Mandrin specimens; _MH, modern human-based reconstruction of the Mandrin specimens; _NEA, Neanderthal-based reconstruction of the Mandrin specimens.

Layer	tooth	CV correct classification	posterior probability
C	Ldm2	UPMH: 88.9 %; HH: 84.2 % (MH: 100.0 %) NEA: 100.0 %	Man11 C 204: 100.0 % NEA
D	Udm2	UPMH: 77.8 %; HH: 66.7 % (MH: 100.0 %) NEA: 100.0 %	Man04 D 395: 99.2 % NEA Man04 D 679: 100.0 % NEA
E	Udm2	UPMH: 100 %; HH: 75.9 % (MH: 100.0 %) NEA: 100.0 %	Man12 E 1300_geom: 97.0% UPMH Man12 E 1300_MH: 91.0 % UPMH Man12 E 1300_NEA: 86.0 % UPMH
F	LM1	UPMH: 100 %; HH: 92.3 % (MH: 100.0 %) NEA: 100.0 %	Man98 F 811_geom: 84.3 % NEA Man98 F 811_MH: 99.2 % NEA Man98 F 811 NEA: 99.7 % NEA

Table S22. Results of the cross-validated between-group principal component analysis (bgPCA) and cross-validated canonical variates analyses (CVA) for the 2D and 3D analyses of the deciduous upper second molar (Udm2) talon EDJ. The leave-one-out cross-validation (CV) shows excellent predictive accuracy, with a clear discrimination between Neanderthals (NEA) and modern humans (MH), even if Upper Pleistocene modern (UPMH) and Holocene humans (HH) tend to overlap. The posterior probabilities that the Mandrin specimens are closer to any group (NEA, UPMH or HH) or belong to one of these groups were then calculated for the bgPCA and CVA outputs, respectively. The highest probabilities are indicated in bold (the greater the number, the higher the probability)._geom, geometric-based reconstruction of the Mandrin specimens; _MH, modern human-based reconstruction of the Mandrin specimens; _NEA, Neanderthal-based reconstruction of the Mandrin specimens.

bgPCA 2D analyses of the EDJ talon		CVA 2D analyses of the EDJ talon	
CV correct classification	posterior probability	CV correct classification	posterior probability
UPMH: 75.0 %; HH: 65.5 % (MH: 100.0 %) NEA: 100.0 %	Man12 E 1300: **0.126 UPMH**; >0.001 HH; >0.001 NEA	UPMH: 75.0 %; HH: 79.3 % (MH: 100.0 %) NEA: 100.0 %	Man12 E 1300: 90.0 % UPMH
bgPCA 3D analyses of the EDJ talon		CVA 3D analyses of the EDJ talon	
CV correct classification	posterior probability	CV correct classification	posterior probability
UPMH: 75.0 %; HH: 79.3 % (MH: 100.0 %) NEA: 100.0 %	Man12 E 1300_geom: **0.300 UPMH**; 0.012 HH; 0.063 NEA Man12 E 1300_MH: **0.880UPMH**; 0.102 HH; 0.006 NEA Man12 E 1300_NEA: **0.365 UPMH**; 0.007 HH; 0.013 NEA	UPMH: 50.0 %; HH: 75.9 % (MH: 100.0 %) NEA: 100.0 %	Man12 E 1300_geom: 91.0 % UPMH Man12 E 1300_MH: 94.0 % UPMH Man12 E 1300_NEA: 97.0 % UPMH

Table S23. Proteins identified in each sample showing their scores, number of ion matches and number of sequences.

Specimen	Protein	Score	Matches	Sequences
1265	CO1A1	12571	632	64
	CO1A2	11139	394	51
	CO3A1	212	8	7
	CO5A2	162	7	6
	CO5A1	51	2	2
2583	CO1A2	10797	393	50
	CO1A1	10599	552	52
	CO5A2	126	4	3
	CO3A1	65	3	3
1275	CO1A1	11125	571	61
	CO1A2	9849	361	54
	CO5A2	87	3	3
	CO5A1	62	2	2
3299	CO1A1	11697	602	60
	CO1A2	10189	385	48
	CO5A2	144	5	5
	CO3A1	101	4	4
	CO5A1	80	3	3

1597	CO1A1	11470	567	57
	CO1A2	11028	451	51
	CO3A1	274	6	3
	CO5A1	140	7	5
	CO5A2	100	4	4
2855B	CO1A1	12516	639	65
	CO1A2	10713	399	57
	CO5A2	112	6	6
	CO5A1	60	2	2
2854	CO1A1	11899	586	64
	CO1A2	10797	426	48
	CO5A2	127	5	5
	CO5A1	81	2	1
	COBA2	68	2	2
1587B	CO1A1	12448	610	58
	CO1A2	10831	430	53
	CO5A1	87	4	4
	CO5A2	60	2	2
	CO3A1	51	2	2

1596	CO1A1	12281	592	55
	CO1A2	11208	453	54
	CO3A1	157	6	4
	CO5A1	127	3	2
	CO5A2	43	2	2

REFERENCES AND NOTES

1. J.-J. Hublin, A. Ben-Ncer, S. E. Bailey, S. E. Freidline, S. Neubauer, M. M. Skinner, I. Bergmann, A. le Cabec, S. Benazzi, K. Harvati, P. Gunz, New fossils from Jebel Irhoud, Morocco and the pan-African origin of *Homo sapiens*. *Nature* **546**, 289–292 (2017).

2. E. M. L. Scerri, M. G. Thomas, A. Manica, P. Gunz, J. T. Stock, C. Stringer, M. Grove, H. S. Groucutt, A. Timmermann, G. P. Rightmire, F. d'Errico, C. A. Tryon, N. A. Drake, A. S. Brooks, R. W. Dennell, R. Durbin, B. M. Henn, J. Lee-Thorp, P. deMenocal, M. D. Petraglia, J. C. Thompson, A. Scally, L. Chikhi, Did our species evolve in subdivided populations across Africa, and why does it matter? *Trends Ecol. Evol.* **33**, 582–594 (2018).

3. C. Stringer, The origin and evolution of *Homo sapiens*. *Philos. Trans. R. Soc. B* **371**, 20150237 (2016).

4. K. Harvati, C. Röding, A. M. Bosman, F. A. Karakostis, R. Grün, C. Stringer, P. Karkanas, N. C. Thompson, V. Koutoulidis, L. A. Moulopoulos, V. G. Gorgoulis, M. Kouloukoussa, Apidima Cave fossils provide earliest evidence of *Homo sapiens* in Eurasia. *Nature* **571**, 500–504 (2019).

5. J.-J. Hublin, The modern human colonization of western Eurasia: When and where? *Quat. Sci. Rev.* **118**, 194–210 (2015).

6. I. Hershkovitz, O. Marder, A. Ayalon, M. Bar-Matthews, G. Yasur, E. Boaretto, V. Caracuta, B. Alex, A. Frumkin, M. Goder-Goldberger, P. Gunz, R. L. Holloway, B. Latimer, R. Lavi, A. Matthews, V. Slon, D. B. Y. Mayer, F. Berna, G. Bar-Oz, R. Yeshurun, H. May, M. G. Hans, G. W. Weber, O. Barzilai, Levantine cranium from Manot Cave (Israel) foreshadows the first European modern humans. *Nature* **520**, 216–219 (2015).

7. W. Liu, M. Martinón-Torres, Y. J. Cai, S. Xing, H. W. Tong, S. W. Pei, M. J. Sier, X. H. Wu, R. L. Edwards, H. Cheng, Y. Y. Li, X. X. Yang, J. M. B. de Castro, X. J. Wu, The earliest unequivocally modern humans in southern China. *Nature* **526**, 696–699 (2015).

8. C. Clarkson, Z. Jacobs, B. Marwick, R. Fullagar, L. Wallis, M. Smith, R. G. Roberts, E. Hayes, K. Lowe, X. Carah, S. A. Florin, J. McNeil, D. Cox, L. J. Arnold, Q. Hua, J. Huntley, H. E. A. Brand,

T. Manne, A. Fairbairn, J. Shulmeister, L. Lyle, M. Salinas, M. Page, K. Connell, G. Park, K. Norman, T. Murphy, C. Pardoe, Human occupation of northern Australia by 65,000 years ago. *Nature* **547**, 306–310 (2017).

9. A. Moroni, A. Ronchitelli, S. Arrighi, D. Aureli, S. Bailey, P. Boscato, F. Boschin, G. Capecchi, J. Crezzini, K. Douka, G. Marciani, D. Panetta, F. Ranaldo, S. Ricci, S. Scaramucci, V. Spagnolo, S. Benazzi, P. Gambassini, Grotta del Cavallo (Apulia – Southern Italy). The Uluzzian in the mirror. *J. Anthropol. Sci.* **96**, 125–160 (2018).

10. S. Benazzi, V. Slon, S. Talamo, F. Negrino, M. Peresani, S. E. Bailey, S. Sawyer, D. Panetta, G. Vicino, E. Starnini, M. A. Mannino, P. A. Salvadori, M. Meyer, S. Paabo, J. J. Hublin, The makers of the Protoaurignacian and implications for Neandertal extinction. *Science* **348**, 793–796 (2015).

11. S. Benazzi, K. Douka, C. Fornai, C. C. Bauer, O. Kullmer, J. Svoboda, I. Pap, F. Mallegni, P. Bayle, M. Coquerelle, S. Condemi, A. Ronchitelli, K. Harvati, G. W. Weber, Early dispersal of modern humans in Europe and implications for Neanderthal behaviour. *Nature* **479**, 525–528 (2011).

12. M. Peresani, S. Bertola, D. Delpiano, S. Benazzi, M. Romandini, The Uluzzian in the north of Italy: Insights around the new evidence at Riparo Broion. *Archaeol. Anthropol. Sci.* **11**, 3503–3536 (2019).

13. J.-J. Hublin, N. Sirakov, V. Aldeias, S. Bailey, E. Bard, V. Delvigne, E. Endarova, Y. Fagault, H. Fewlass, M. Hajdinjak, B. Kromer, I. Krumov, J. Marreiros, N. L. Martisius, L. Paskulin, V. Sinet-Mathiot, M. Meyer, S. Pääbo, V. Popov, Z. Rezek, S. Sirakova, M. M. Skinner, G. M. Smith, R. Spasov, S. Talamo, T. Tuna, L. Wacker, F. Welker, A. Wilcke, N. Zahariev, S. P. McPherron, T. Tsanova, Initial Upper Palaeolithic *Homo sapiens* from Bacho Kiro Cave, Bulgaria. *Nature* **581**, 299–302 (2020).

14. P. Semal, H. Rougier, I. Crevecoeur, C. Jungels, D. Flas, A. Hauzeur, B. Maureille, M. Germonpré, H. Bocherens, S. Pirson, L. Cammaert, N. de Clerck, A. Hambucken, T. Higham, M. Toussaint, J. van der Plicht, New data on the late Neandertals: Direct dating of the Belgian Spy fossils. *Am. J. Phys. Anthropol.* **138**, 421–428 (2009).

15. J.-J. Hublin, S. Talamo, M. Julien, F. David, N. Connet, P. Bodu, B. Vandermeersch, M. P. Richards, Radiocarbon dates from the Grotte du Renne and Saint-Césaire support a Neandertal origin for the Châtelperronian. *Proc. Natl. Acad. Sci. U.S.A.* **109**, 18743–18748 (2012).

16. T. Higham, K. Douka, R. Wood, C. B. Ramsey, F. Brock, L. Basell, M. Camps, A. Arrizabalaga, J. Baena, C. Barroso-Ruíz, C. Bergman, C. Boitard, P. Boscato, M. Caparrós, N. J. Conard, C. Draily, A. Froment, B. Galván, P. Gambassini, A. Garcia-Moreno, S. Grimaldi, P. Haesaerts, B. Holt, M. J. Iriarte-Chiapusso, A. Jelinek, J. F. Jordá Pardo, J. M. Maíllo-Fernández, A. Marom, J. Maroto, M. Menéndez, L. Metz, E. Morin, A. Moroni, F. Negrino, E. Panagopoulou, M. Peresani, S. Pirson, M. de la Rasilla, J. Riel-Salvatore, A. Ronchitelli, D. Santamaria, P. Semal, L. Slimak, J. Soler, N. Soler, A. Villaluenga, R. Pinhasi, R. Jacobi, The timing and spatiotemporal patterning of Neanderthal disappearance. *Nature* **512**, 306–309 (2014).

17. F. Welker, M. Hajdinjak, S. Talamo, K. Jaouen, M. Dannemann, F. David, M. Julien, M. Meyer, J. Kelso, I. Barnes, S. Brace, P. Kamminga, R. Fischer, B. M. Kessler, J. R. Stewart, S. Pääbo, M. J. Collins, J. J. Hublin, Palaeoproteomic evidence identifies archaic hominins associated with the Châtelperronian at the Grotte du Renne. *Proc. Natl. Acad. Sci. U.S.A.* **113**, 11162–11167 (2016).

18. D. Richter, G. Tostevin, P. Škrdla, W. Davies, New radiometric ages for the early Upper Palaeolithic type locality of Brno-Bohunice (Czech Republic): Comparison of OSL, IRSL, TL and ^{14}C dating results. *J. Archaeol. Sci.* **36**, 708–720 (2009).

19. B. Gravina, F. Bachellerie, S. Caux, E. Discamps, J.-P. Faivre, A. Galland, A. Michel, N. Teyssandier, J.-G. Bordes, No reliable evidence for a Neanderthal-Châtelperronian association at La Roche-à-Pierrot, Saint-Césaire. *Sci. Rep.* **8**, 15134 (2018).

20. L. Slimak, For a cultural anthropology of the last Neanderthals. *Quat. Sci. Rev.* **217**, 330–339 (2019).

21. M. Cortés-Sánchez, F. J. Jiménez-Espejo, M. D. Simón-Vallejo, C. Stringer, M. C. Lozano Francisco, A. García-Alix, J. L. Vera Peláez, C. P. Odriozola, J. A. Riquelme-Cantal, R. Parrilla Giráldez, A. Maestro González, N. Ohkouchi, A. Morales-Muñiz, An early Aurignacian arrival in southwestern Europe. *Nat. Ecol. Evol.* **3,** 207–212 (2019).

22. L. Slimak, Sociodiversity and paradoxes from the end of the Middle Paleolithic to the emergence of the Upper Paleolithic, in *The Third Man. The Prehistory of the Altaï*, J. J. Cleyet−Merle, M. V. Shunkov, J. M. Geneste, A. P. Derevianko, L. Slimak, A. L. Krivoshapkin, B. Gravina, A. Turq, B. Maureille, Eds. (Éditions de la Réunion des musées nationaux – Grand Palais, 2017) pp. 125–133.

23. V. P. Chabai, A. Marks, K. Monigal, Crimea in the context of the Eastern European Middle Paleolithic and Early Upper Paleolithic, in *The Middle Paleolithic and Early Upper Paleolithic of Eastern Crimea*, V. P. Chabai, K. Monigal, A. E. Marks, Eds. (ERAUL, Liège, 2004), pp. 419–460.

24. P. R. Nigst, P. Haesaerts, F. Damblon, C. Frank-Fellner, C. Mallol, B. Viola, M. Götzinger, L. Niven, G. Trnka, J. J. Hublin, Early modern human settlement of Europe north of the Alps occurred 43,500 years ago in a cold steppe-type environment. *Proc. Natl. Acad. Sci. U.S.A.* **111**, 14394–14399 (2014).

25. L. Slimak, The Neronian and the historical structure of cultural shifts from Middle to Upper Palaeolithic in Mediterranean France. *J. Archaeol. Sci.* **35**, 2204–2214 (2008).

26. J. Combier, *Le Paléolithique de l'Ardèche dans son Cadre Paléoclimatique*. Mémoire de l'Institute de Préhistoire de l'Université de Bordeaux 4 (Delmas, 1967).

27. L. Metz, *Néandertal en armes? Des armes, et de l'arc, au tournant du 50ème millénaire en France Méditerranéenne*, thesis, Aix-Marseille University, France (2015).

28. J. Combier, De la fin du Moustérien au Paléolithique supérieur. Les données de la région rhodanienne, in *Paléolithique moyen récent et Paléolithique supérieur ancien. Ruptures et transitions : Examen critique de documents archéologiques*, C. Farizy, Ed. (Musée de Préhistoire d'Île de France, 1990), pp. 267–277.

29. L. Slimak, Sur un point de vue heuristique concernant la production et la transformation de support au Paléolithique moyen. *Gallia Préhistoire* **50**, 1–22 (2008).

30. M. D. Bosch, M. A. Mannino, A. L. Prendergast, T. C. O'Connell, B. Demarchi, S. M. Taylor, L. Niven, J. van der Plicht, J. J. Hublin, New chronology for Ksâr 'Akil (Lebanon) supports Levantine route of modern human dispersal into Europe. *Proc. Natl. Acad. Sci. U.S.A.* **112**, 7683–7688 (2015).

31. K. Douka, C. A. Bergman, R. E. M. Hedges, F. P. Wesselingh, T. F. G. Higham, Chronology of Ksar Akil (Lebanon) and implications for the colonization of Europe by anatomically modern humans. *PLOS ONE* **8**, e72931 (2013).

32. P. Skrdla, Comparison of Boker Tachtit and Stranska Skala MP/UP transitional industries. *J. Israel Prehistoric Soc.* **33**, 37–73 (2003).

33. I. Azoury, *Ksar Akil, Lebanon: A Technological and Typological Analysis of the Transitional and Early Upper Palaeolithic Levels of Ksar Akil and Abu Halka. Vol. I, Levels XXV-XII* (BAR International Series, 1986).

34. C. A. Bergman, Synthèse Paléolithique supérieur. *Paléorient* **14**, 223–227 (1988).

35. S. L. Kuhn, M. C. Stiner, D. S. Reese, E. Güleç, Ornaments of the earliest Upper Paleolithic: New insights from the Levant. *Proc. Natl. Acad. Sci. U.S.A.* **98**, 7641–7646 (2001).

36. K. Ohnuma, C. A. Bergman, A Technological Analysis of the Upper Paleolithic Levels (XXV-VI) of Ksar Akil, Lebanon, in *The Emergence of Modern Humans: An Archaeological Perspective*, P. Mellars, (Edinburgh Univ. Press, 1990), pp. 91–138.

37. C. A. Bergman, C. B. Stringer, Fifty years after: Egbert, an Early Upper Palaeolithic juvenile from Ksar Akil, Lebanon. *Paléorient* **15**, 99–111 (1989).

38. M. Kuhlwilm, I. Gronau, M. J. Hubisz, C. de Filippo, J. Prado-Martinez, M. Kircher, Q. Fu, H. A. Burbano, C. Lalueza-Fox, M. de la Rasilla, A. Rosas, P. Rudan, D. Brajkovic, Ž. Kucan, I. Gušic, T. Marques-Bonet, A. M. Andrés, B. Viola, S. Pääbo, M. Meyer, A. Siepel, S. Castellano, Ancient gene flow from early modern humans into Eastern Neanderthals. *Nature* **530**, 429–433 (2016).

39. F. A. Villanea, J. G. Schraiber, Multiple episodes of interbreeding between Neanderthal and modern humans. *Nat. Ecol. Evol.* **3**, 39–44 (2019).

40. M. J. Hubisz, A. L. Williams, A. Siepel, Mapping gene flow between ancient hominins through demography-aware inference of the ancestral recombination graph. *bioRxiv*, 687368 (2019)

41. B. Vernot, S. Tucci, J. Kelso, J. G. Schraiber, A. B. Wolf, R. M. Gittelman, M. Dannemann, S. Grote, R. C. McCoy, H. Norton, L. B. Scheinfeldt, D. A. Merriwether, G. Koki, J. S. Friedlaender, J. Wakefield, S. Pääbo, J. M. Akey, Excavating Neandertal and Denisovan DNA from the genomes of Melanesian individuals. *Science* **352**, 235–239 (2016).

42. A. B. Wolf, J. M. Akey, Outstanding questions in the study of archaic hominin admixture. *PLOS Genet.* **14**, e1007349 (2018).

43. J. D. Wall, M. A. Yang, F. Jay, S. K. Kim, E. Y. Durand, L. S. Stevison, C. Gignoux, A. Woerner, M. F. Hammer, M. Slatkin, Higher levels of neanderthal ancestry in East Asians than in Europeans. *Genetics* **194**, 199–209 (2013).

44. S. Sankararaman, N. Patterson, H. Li, S. Pääbo, D. Reich, The date of interbreeding between neandertals and modern humans. *PLOS Genet.* **8**, e1002947 (2012).

45. Q. Fu, M. Hajdinjak, O. T. Moldovan, S. Constantin, S. Mallick, P. Skoglund, N. Patterson, N. Rohland, I. Lazaridis, B. Nickel, B. Viola, K. Prüfer, M. Meyer, J. Kelso, D. Reich, S. Pääbo, An early modern human from Romania with a recent Neanderthal ancestor. *Nature* **524**, 216–219 (2015).

46. M. Hajdinjak, Q. Fu, A. Hübner, M. Petr, F. Mafessoni, S. Grote, P. Skoglund, V. Narasimham, H. Rougier, I. Crevecoeur, P. Semal, M. Soressi, S. Talamo, J. J. Hublin, I. Gušić, Ž. Kućan, P. Rudan, L. V. Golovanova, V. B. Doronichev, C. Posth, J. Krause, P. Korlević, S. Nagel, B. Nickel, M. Slatkin, N. Patterson, D. Reich, K. Prüfer, M. Meyer, S. Pääbo, J. Kelso, Reconstructing the genetic history of late Neanderthals. *Nature* **555** 652–656 (2018).

47. S. Vandevelde, J. É. Brochier, C. Petit, L. Slimak, Establishment of occupation chronicles in Grotte Mandrin using sooted concretions: Rethinking the Middle to Upper Paleolithic transition. *J. Hum. Evol.* **112**, 70–78 (2017).

48. S. Vandevelde, *Y'a pas de suie sans feu ! Étude micro-chronologique des concrétions fuligineuses. Étude de cas : Le site paléolithique de la Grotte Mandrin (France) [There's no soot without fire!*

Micro-chronological study of fuliginous speleothems. Case study: The Grotte of Mandrin (France) Paleolithic site], thesis, Université de Paris 1 – Panthéon-Sorbonne (2019).

49. T. F. G. Higham, R. M. Jacobi, C. Bronk Ramsey, AMS radiocarbon dating of ancient bone using ultrafiltration. *Radiocarbon*, **48**, 179–195 (2006).

50. C. Bronk Ramsey, T. F. G. Higham, A. Bowles, R. Hedges, Improvements to the pretreatment of bone at Oxford. *Radiocarbon* **46,** 155–163 (2004).

51. F. Brock, C. Bronk Ramsey, T. F. G. Higham, Quality Assurance of ultrafiltered bone dating. *Radiocarbon* **49,** 187–192 (2007).

52. M. Stuiver, H. A. Polach, Discussion reporting of ^{14}C data. *Radiocarbon* **19,** 355–363 (1977).

53. R. E. Wood, C. Bronk Ramsey, T. F. G. Higham, Refining the ultrafiltration bone pretreatment background for radiocarbon dating at ORAU. *Radiocarbon* **52**, 600–611 (2010).

54. A. G. Wintle, A. S. Murray, A review of quartz optically stimulated luminescence characteristics and their relevance in single-aliquot regeneration dating protocols. *Radiat. Meas.* **41**, 369–391 (2006).

55. C. Bronk Ramsey, Bayesian analysis of radiocarbon dates. *Radiocarbon* **51,** 337–360 (2009).

56. P. J. Reimer, W. E. N. Austin, E. Bard, A. Bayliss, P. G. Blackwell, C. Bronk Ramsey, M. Butzin, H. Cheng, R. L. Edwards, M. Friedrich, P. M. Grootes, T. P. Guilderson, I. Hajdas, T. J. Heaton, A. G. Hogg, K. A. Hughen, B. Kromer, S. W. Manning, R. Muscheler, J. G. Palmer, C. Pearson, J. van der Plicht, R. W. Reimer, D. A. Richards, E. M. Scott, J. R. Southon, CS. M. Turney, L. Wacker, F. Adolphi, U. Büntgen, M. Capano, S. M. Fahrni, A. Fogtmann-Schulz, R. Friedrich, P. Köhler, S. Kudsk, F. Miyake, J. Olsen, F. Reinig, M. Sakamoto, A. Sookdeo, S. Talamo, The IntCal20 Northern Hemisphere radiocarbon age calibration curve (0–55 cal kBP). *Radiocarbon* **62**(4): 725–757 (2020).

57. C. Bronk Ramsey, Dealing with outliers and offsets in radiocarbon dating. *Radiocarbon* **51**, 1023–1045 (2009).

58. E. Trinkaus, O. Moldovan, Milota, A. Bilgar, L. Sarcina, S. Athreya, S. E. Bailey, R. Rodrigo, G. Mircea, T. Higham, C. B. Ramsey, J. van der Plicht, An Early Modern Human from the Peştera cu Oase, Romania. *Proc. Natl. Acad. Sci. U.S.A.* **100,** 11231–11236 (2003).

59. K. Douka, T. F. G. Higham, C. Bergman, Statistical and archaeological errors invalidate the proposed chronology for the site of Ksar Akil. *Proc. Natl. Acad. Sci. U.S.A.* **112**, E7034 (2015).

60. M. Bosch, M. A. Mannino, A. L. Prendergast, T. C. O'Connell, B. Demarchi, S. M. Taylor, L. Niven, J. van der Plicht, J.-J. Hublin, Reply to Douka *et al*.: Critical evaluation of the Ksâr 'Akil chronologies. *Proc. Natl. Acad. Sci. U.S.A.* **112**, E7035 (2015).

61. S. L. Kuhn, N. Zwyns, Rethinking the initial Upper Paleolithic. *Quat. Int.* **347**, 29–38 (2014).

62. D. Richter, G. Tostevin, P. Škrdla, Bohunician technology and thermoluminescence dating of the type locality of Brno-Bohunice (Czech Republic). *J. Hum. Evol.* **55**, 871–885 (2008).

63. E. Boaretto, M. Hernandez, M. Goder-Goldberger, V. Aldeias, L. Regev, V. Caracuta, S. P. McPherron, J. J. Hublin, S. Weiner, O. Barzilai The absolute chronology of Boker Tachtit (Israel) and implications for the Middle to Upper Paleolithic transition in the Levant. *Proc. Natl. Acad. Sci. U.S.A.* **118**, e2014657118 (2021).

64. C. Gaunitz, A. Fages, K. Hanghøj, A. Albrechtsen, N. Khan, M. Schubert, A. Seguin-Orlando, I. J. Owens, S. Felkel, O. Bignon-Lau, P. de Barros Damgaard, A. Mittnik, A. F. Mohaseb, H. Davoudi, S. Alquraishi, A. H. Alfarhan, K. A. S. al-Rasheid, E. Crubézy, N. Benecke, S. Olsen, D. Brown, D. Anthony, K. Massy, V. Pitulko, A. Kasparov, G. Brem, M. Hofreiter, G. Mukhtarova, N. Baimukhanov, L. Lõugas, V. Onar, P. W. Stockhammer, J. Krause, B. Boldgiv, S. Undrakhbold, D. Erdenebaatar, S. Lepetz, M. Mashkour, A. Ludwig, B. Wallner, V. Merz, I. Merz, V. Zaibert, E. Willerslev, P. Librado, A. K. Outram, L. Orlando, Ancient genomes revisit the ancestry of domestic and Przewalski's horses. *Science* **360**, 111–114 (2018).

65. C. Gamba, K. Hanghøj, C. Gaunitz, A. H. Alfarhan, S. A. Alquraishi, K. A. S. al-Rasheid, D. A. N. I. E. L. G. Bradley, L. Orlando, Comparing the performance of three ancient DNA extraction methods for high-throughput sequencing. *Mol. Ecol. Resour.* **16**, 459–469 (2016).

66. N. Rohland, E. Harney, S. Mallick, S. Nordenfelt, D. Reich, Partial uracil-DNA-glycosylase treatment for screening of ancient DNA. *Philos. Trans. R. Soc. Lond. Ser. B Biol. Sci.* **370**, 20130624 (2015).

67. X. Xiufeng, U. Árnason, The complete mitochondrial DNA sequence of the horse, *Equus caballus*: Extensive heteroplasmy of the control region. *Gene* **148**, 357–362 (1994).

68. C. M. Wade, E. Giulotto, S. Sigurdsson, M. Zoli, S. Gnerre, F. Imsland, T. L. Lear, D. L. Adelson, E. Bailey, R. R. Bellone, H. Blöcker, O. Distl, R. C. Edgar, M. Garber, T. Leeb, E. Mauceli, J. N. MacLeod, M. C. T. Penedo, J. M. Raison, T. Sharpe, J. Vogel, L. Andersson, D. F. Antczak, T. Biagi, M. M. Binns, B. P. Chowdhary, S. J. Coleman, G. Della Valle, S. Fryc, G. Guérin, T. Hasegawa, E. W. Hill, J. Jurka, A. Kiialainen, G. Lindgren, J. Liu, E. Magnani, J. R. Mickelson, J. Murray, S. G. Nergadze, R. Onofrio, S. Pedroni, M. F. Piras, T. Raudsepp, M. Rocchi, K. H. Røed, O. A. Ryder, S. Searle, L. Skow, J. E. Swinburne, A. C. Syvänen, T. Tozaki, S. J. Valberg, M. Vaudin, J. R. White, M. C. Zody; Broad Institute Genome Sequencing Platform; Broad Institute Whole Genome Assembly Team; E. S. Lander, K. Lindblad-Toh, Genome sequence, comparative analysis, and population genetics of the domestic horse. *Science* **326**, 865–867 (2009).

69. M. Schubert, L. Ermin, C. D. Sarkissian, H. Jónsson, A. Ginolhac, R. Schaefer, M. D. Martin, R. Fernández, M. Kircher, M. McCue, E. Willerslev, L. Orlando, Characterization of ancient and modern genomes by SNP detection and phylogenomic and metagenomic analysis using PALEOMIX. *Nat. Protoc.* **9**, 1056–1082 (2014).

70. M. Schubert, S. Lindgreen, L. Orlando, AdapterRemoval v2: Rapid adapter trimming, identification, and read merging. *BMC. Res. Notes* **9**, 88 (2016).

71. C. F. Spoor, F. W. Zonneveld, G. A. Macho, Linear measurements of cortical bone and dental enamel by computed tomography: Applications and problems. *Am. J. Phys. Anthropol.* **91**, 469–484 (1993).

72. R. J. Fajardo, T. M. Ryan, J. Kappelman, Assessing the accuracy of high-resolution X-ray computed tomography of primate trabecular bone by comparisons with histological sections. *Am. J. Phys. Anthropol.* **118**, 1–10 (2002).

73. M. N. Coleman, M. W. Colbert, Technical note: CT thresholding protocols for taking measurements on three-dimensional models. *Am. J. Phys. Anthropol.* **133**, 723–725 (2007).

74. S. Benazzi, S. E. Bailey, M. Peresani, M. A. Mannino, M. Romandini, M. P. Richards, J. J. Hublin, Middle Paleolithic and Uluzzian human remains from Fumane Cave, Italy. *J. Hum. Evol.* **70**, 61–68 (2014).

75. M. Toussaint, A. J. Olejniczak, S. el Zaatari, P. Cattelain, D. Flas, C. Letourneux, S. Pirson, The Neandertal lower right deciduous second molar from Trou de l'Abîme at Couvin, Belgium. *J. Hum. Evol.* **58**, 56–67 (2010).

76. J.-L. Voisin, S. Condemi, M. H. Wolpoff, D. W. Frayer, A new online database (http://anthropologicaldata.free.fr) and a short reflection about the productive use of compiling Internet data. *PaleoAnthropology* **2012**, 241–244 (2012).

77. B. Maureille, H. Rougier, F. Houët, B. Vandermeersch, Les dents inférieures du néandertalien Regourdou 1 (site de Regourdou, commune de Montignac, Dordogne): Analyses métriques et comparatives. *Paleo* **13**, 183–200 (2001).

78. H. Scolan, F. Santos, A.-M. Tillier, B. Maureille, A. Quintard, Des nouveaux vestiges néanderthaliens à Las Pélénos (Monsempron-Libos, Lot-et-Garonne, France). *Bull. Mém. Soc. Anthropol. Paris* **24**, 69–95 (2012).

79. R. Macchiarelli, P. Bayle, L. Bondioli, A. Mazurier, C. Zanolli, From outer to inner structural morphology in dental anthropology. The integration of the third dimension in the visualization and quantitative analysis of fossil remains, in *Anthropological Perspectives on Tooth Morphology: Genetics, Evolution, Variation*, R.G. Scott, J.D. Irish, Eds. (Cambridge Univ. Press; Cambridge, 2013), pp. 250–277.

80. C. Zanolli, P. Bayle, L. Bondiolin, M. C. Dean, M. L. Luyer, A. Mazurier, W. Morita, R. Macchiarelli, Is the deciduous/permanent molar enamel thickness ratio a taxon-specific indicator in extant and extinct hominids? *C.R. Palevol* **16**, 702–714 (2017).

81. C. Zanolli, M. Martinón-Torres, F. Bernardini, G. Boschian, A. Coppa, D. Dreossi, L. Mancini, M. Martínez de Pinillos, L. Martín-Francés, J. M. Bermúdez de Castro, C. Tozzi, C. Tuniz, R. Macchiarelli, The Middle Pleistocene (MIS 12) human dental remains from Fontana Ranuccio (Latium) and Visogliano (Friuli-Venezia Giulia), Italy. A comparative high resolution endostructural assessment. *PLOS ONE* **13**, e0189773 (2018).

82. K. Kupczik, L. K. Delezene, M. M. Skinner, Mandibular molar root and pulp cavity morphology in *Homo naledi* and other Plio-Pleistocene hominins. *J. Hum. Evol.* **130**, 83–95.

83. S. E. Bailey, S. Benazzi, J.-J. Hublin, Allometry, merism, and tooth shape of the upper deciduous m2 and permanent M1. *Am. J. Phys. Anthropol.***154**, 104–114 (2014).

84. F.J. Rohlf, TpsDig2. *TpsSeries* (Department of Ecology and Evolution, SUNY, Stony Brook, New York, 2005).

85. S. E. Bailey, S. Benazzi, L. Buti, J.-J. Hublin, Allometry, merism, and tooth shape of the lower second deciduous molar and first permanent molar. *Am. J. Phys. Anthropol.* **159**, 93–105 (2016).

86. A. Cardini, P. D. Polly, Cross-validated between group PCA scatterplots: A solution to spurious group separation? *Evol. Biol.* **47**, 85–95 (2020).

87. P. Mitteroecker, F. L. Bookstein, Linear discrimination, ordination, and the visualization of selection gradients in modern morphometrics. *Evol. Biol.* **38**, 100–114 (2011).

88. A. Cardini, P. O'Higgins, F. J. Rohlf, Seeing distinct groups where there are none: Spurious patterns from between-group PCA. *Evol. Biol.* **46**, 303–316 (2019).

89. S. Schlager, Chapter 9 - Morpho and Rvcg – Shape Analysis in R: R-Packages for Geometric Morphometrics, Shape Analysis and Surface Manipulations, in *Statistical Shape and Deformation Analysis*, G. Zheng, S. Li, G. Szekely (London, Academic Press, 2017), pp. 217–256.

90. R Development Core Team. R: *A language and environment for statistical computing*. http://www.R-project.org. (2017).

91. F.L. Bookstein, *Morphometric Tools for Landmark Data: Geometry and Biology* (Cambridge Univ. Press, 1991).

92. G. Guerin, N. Mercier, G. Adamiec, Dose-rate conversion factors: Update. *Ancient TL* **29**, 5–8 (2011).

93. G. Guérin, N. Mercier, R. Nathan, G. Adamiec, Y. Lefrais, On the use of the infinite matrix assumption and associated concepts: A critical review. *Radiat. Meas.* **47**, 778–785 (2012).

94. N. Mercier, H. Valladas, G. Valladas, A new dosimetric calibration tool. *Nucl. Tracks Radiat. Meas.* **23**, 507–508 (1994).

95. V. J. Bortolot, A new modular high capacity OSL reader system. *Radiat. Meas.* **32**, 751–757 (2000).

96. J. R. Prescott, J. T. Hutton, Cosmic ray contributions to dose rates for luminescence and ESR dating: Large depths and long-term time variations. *Radiat. Meas.* **23**, 497–500 (1994).

97. F. De Corte, D. Vandenberghe, J. P. Buylaert, P. Van den Haute, J. Kucera, Relative and k0-standardized INAA to assess the internal (Th, U) radiation dose rate in the 'quartz coarse-grain protocol' for OSL dating of sediments: Unexpected observations. *Nucl. Instrum. Methods Phys. Res. A* **564**, 743–751 (2006).

98. D. Vandenberghe, F. De Corte, J. P. Buylaert, J. Kucera, P. Van den Haute, On the internal radioactivity in quartz. *Radiat. Meas.* **43**, 771–775 (2008).

99. D. Richter, A. Richter, K. Dornich, Lexsyg—A new system for luminescence research. *Geochronometria* **40**, 220–228 (2013).

100. D. Richter, R. Pintaske, K. Dornich, M. R. Krbetschek, A novel beta source design for uniform irradiation in dosimetric applications. *Ancient TL* **30**, 57–63 (2012).

101. A. S. Murray, A. G. Wintle, Luminescence dating of quartz using an improved single-aliquot regenerative-dose protocol. *Radiat. Meas.* **32**, 57–73 (2000).

102. G. A. T. Duller, Distinguishing quartz and feldspar in single grain luminescence measurements. *Radiat. Meas.* **37**, 161–165 (2003).

103. G. A. T. Duller, The Analyst software package for luminescence data: Overview and recent improvements. *Ancient TL* **33**, 35–42 (2015).

104. M. Dietze, S. Kreutzer, C. Burow, M. C. Fuchs, M. Fischer, C. Schmidt, The abanico plot: Visualizing chronometric data with individual standard errors. *Quat. Geochronol.* **9**, 54–64 (2012).

105. S. Kreutzer, C. Schmidt, M. C. Fuchs, M. Dietze, M. Fischer, M. Fuchs, Introducing an R package for luminescence dating analysis. *Ancient TL* **30**, 1–8 (2012).

106. L. J. Arnold, R. M. Bailey, G. E. Tucker, Statistical treatment of fluvial dose distributions from southern Colorado arroyo deposits. *Quat. Geochronol.* **2**, 162–167 (2007).

107. L. J. Arnold, R. G. Roberts, R. F. Galbraith, S. B. DeLong, A revised burial dose estimation procedure for optical dating of young and modern-age sediments. *Quat. Geochronol.* **4**, 306–325 (2009).

108. L. J. Arnold, M. Demuro, M. Navazo Ruiz, A. Benito-Calvo, A. Pérez-González, OSL dating of the Middle Palaeolithic Hotel California site, Sierra de Atapuerca, north-central Spain. *Boreas* **42**, 285–305 (2013).

109. L. J. Arnold, M. Demuro, N. A. Spooner, G. J. Prideaux, M. C. McDowell, A. B. Camens, E. H. Reed, J. M. Parés, J. L. Arsuaga, J. M. Bermúdez de Castro, E. Carbonell, Single-grain TT-OSL bleaching characteristics: Insights from modern analogues and OSL dating comparisons. *Quat. Geochronol.* **49**, 45–51 (2019).

110. M. Demuro, R. G. Roberts, D. G. Froese, L. J. Arnold, F. Brock, C. B. Ramsey, Optically stimulated luminescence dating of single and multiple grains of quartz from perennially frozen loess in western Yukon Territory, Canada: Comparison with radiocarbon chronologies for the late Pleistocene Dawson tephra. *Quat. Geochronol.* **3**, 346–364 (2008).

111. M. Demuro, L. J. Arnold, D. Froese, R. G. Roberts, OSL dating of loess deposits bracketing Sheep Creek tephra beds, northwest Canada: Dim and problematic single-grain OSL characteristics and their effect on multi-grain age estimates. *Quat. Geochronol.* **15**, 67–87 (2013).

112. M. J. Aitken, *An Introduction to Optical Dating: The Dating of Quaternary Sediments by the Use of Photon-stimulated Luminescence* (Oxford Univ. Press, 1998).

113. L. J. Arnold, M. Demuro, M. Navazo Ruiz, Empirical insights into multi-grain averaging effects from 'pseudo' single-grain OSL measurements. *Radiat. Meas.* **47**, 652–658 (2012).

114. L. Bøtter-Jensen, M. Mejdahl, Assessment of beta dose-rate using a GM multicounter system. *Nucl. Tracks Radiat. Meas.* **14**, 187–191 (1988).

115. P.J. Potts, M. Thompson, S.R.N. Chenery, P.C. Webb, H.U. Kasper, *Geopt13 - An International Proficiency Test for Analytical Geochemistry Laboratories - Report on Round 13 / July 2003 (Köln Loess)* (International Association of Geoanalysts, 2003).

116. B. J. Brennan, Beta doses to spherical grains. *Radiat. Meas.* **37**, 299–303 (2003).

117. O. Allkofer, *Introduction to Cosmic Radiation* (Verlag Karl Thiemig, Munich, 1974).

118. M. A. Smith, J. R. Prescott, M. J. Head, Comparison of ^{14}C and luminescence chronologies at Puritjarra Rock shelter, central Australia. *Quat. Sci. Rev.* **16,** 299–320 (1997).

119. V. Mejdahl, Internal radioactivity in quartz and feldspar grains. *Ancient TL* **5**, 10–17 (1987).

120. J. M. Bowler, H. Johnston, J. M. Olley, J. R. Prescott, R. G. Roberts, W. Shawcross, N. A. Spooner, New ages for human occupation and climatic change at Lake Mungo, Australia. *Nature* **421**, 837–840 (2003).

121. Z. Jacobs, G. A. T. Duller, A. G. Wintle, C. S. Henshilwood, Extending the chronology of deposits at Blombos Cave, South Africa, back to 140 ka using optical dating of single and multiple grains of quartz. *J. Hum. Evol.* **51**, 255–273 (2006).

122. S. M. Pawley, R. M. Bailey, J. Rose, B. S. P. Moorlock, R. J. O. Hamblin, S. J. Booth, J. R. Lee, Age limits on Middle Pleistocene glacial sediments from OSL dating, north Norfolk, UK. *Quat. Sci. Rev.* **27**, 1363–1377 (2008).

123. R. J. Lewis, J. Tibby, L. J. Arnold, C. Barr, J. Marshall, G. McGregor, P. Gadd, Y. Yokoyama, Insights into subtropical Australian aridity from Welsby Lagoon, North Stradbroke Island, over the past 80,000 years. *Quat. Sci. Rev.* **234**, 106262 (2020).

124. J. Rees-Jones, Optical dating of young sediments using fine-grain quartz. *Ancient TL* **13**, 9–14 (1995).

125. J. Rees-Jones, M. S. Tite, Optical dating results for British archaeological sediments. *Archaeometry* **39**, 177–187 (1997).

126. V. Mejdahl, Thermoluminescence dating: Beta-dose attenuation in quartz grains. *Archaeometry* **21**, 61–72 (1979).

127. M.J. Aitken, *Thermoluminescence Dating* (Academic Press, 1985).

128. M. L. Readhead, Thermoluminescence dose rate data and dating equations for the case of disequilibrium in the decay series. *Nucl. Tracks Radiat. Meas.* **13**, 197–207 (1987).

129. L. J. Arnold, M. Duval, C. Falguères, J.-J. Bahain, M. Demuro, Portable gamma spectrometry with cerium-doped lanthanum bromide scintillators: Suitability assessments for luminescence and electron spin resonance dating applications. *Radiat. Meas.* **47**, 6–18 (2012).

130. L. J. Arnold, M. Duval, M. Demuro, N. A. Spooner, M. Santonja, A. Pérez-González, OSL dating of individual quartz 'supergrains' from the Ancient Middle Palaeolithic site of Cuesta de la Bajada, Spain. *Quat. Geochronol.* **36**, 78–101 (2016).

131. R. F. Galbraith, A note on the variance of a background-corrected OSL count. *Ancient TL* **20**, 49–51 (2002).

132. G. A. T. Duller, Assessing the error on equivalent dose estimates derived from single aliquot regenerative dose measurements. *Ancient TL* **25**, 15–24 (2007).

133. V. Hansen, A. Murray, J.-P. Buylaert, E.-Y. Yeo, K. Thomsen, A new irradiated quartz for beta source calibration. *Radiat. Meas.* **81**, 123–127 (2015).

134. L. J. Arnold, R. G. Roberts, Stochastic modelling of multi-grain equivalent dose (D_e) distributions: Implications for OSL dating of sediment mixtures. *Quat. Geochronol.* **4**, 204–230 (2009).

135. R. M. Bailey, L. J. Arnold, Statistical modelling of single grain quartz De distributions and an assessment of procedures for estimating burial dose. *Quat. Sci. Rev.* **25**, 2475–2502 (2006).

136. L. J. Arnold, R. G. Roberts, Paper I – Optically Stimulated Luminescence (OSL) dating of perennially-frozen deposits in north-central Siberia: OSL characteristics of quartz grains and methodological considerations regarding their suitability for dating. *Boreas* **40**, 389–416 (2011).

137. R. F. Galbraith, R. G. Roberts, G. M. Laslett, H. Yoshida, J. M. Olley, Optical dating of single and multiple grains of quartz from Jinmium rock shelter, northern Australia: Part I, Experimental design and statistical models. *Archaeometry* **41**, 339–364 (1999).

138. L. J. Arnold, R. G. Roberts, R. D. E. MacPhee, E. Willerslev, A. N. Tikhonov, F. Brock, Optical dating of perennially frozen deposits associated with preserved ancient plant and animal DNA in north-central Siberia. *Quat. Geochronol.* **3**, 114–136 (2008).

139. L. J. Arnold, R. G. Roberts, R. D. E. Macphee, J. S. Haile, F. Brock, P. Möller, D. G. Froese, A. N. Tikhonov, A. R. Chivas, M. Thomas P. Gilbert, E. Willerslev, Paper II – Dirt, dates and DNA: OSL and radiocarbon chronologies of perennially frozen sediments in Siberia, and their implications for sedimentary ancient DNA studies. *Boreas* **40**, 417–445 (2011).

140. R. P. Nathan, P. J. Thomas, M. Jain, A. S. Murray, E. J. Rhodes, Environmental dose rate heterogeneity of beta radiation and its implications for luminescence dating: Monte Carlo modelling and experimental validation. *Radiat. Meas.* **37**, 305–313 (2003).

141. H. Valladas, Thermoluminescence dating of flint. *Quat. Sci. Rev.* **11**, 1–5 (1992).

142. G. Valladas, A gamma ray irradiator. *PACT* **3**, 439–442 (1978).

143. G. Guérin, J. C. Lefèvre, A low cost TL–OSL reader dedicated to high temperature studies. *Measurement* **49**, 26–33 (2014).

144. R. Sempéré, B. Charrière, F. Van Wambeke, G. Cauwet, Carbon inputs of the Rhône River to the Mediterranean Sea: Biogeochemical implications. *Glob. Biogeochem. Cycles* **14**, 669–681 (2000).

145. S. Vandevelde, J. É. Brochier, B. Desachy, C. Petit, L. Slimak, Sooted concretions: A new micro-chronological tool for high temporal resolution archaeology. *Quat. Int.* **474**, 103–118 (2018).

146. P. Goldberg, Micromorphology and site formation at Die Kelders Cave I, South Africa. *J. Hum. Evol.* **38**, 43–90 (2000).

147. G. Stoops, *Guidelines for Analysis and Description of Soil and Regolith Thin Sections* (Soil Science Society of America, Madison, WI, 2003).

148. V. Jacq, P. Albert, R. Delome, Le mistral – Quelques aspects des connaissances actuelles. *La Météorol.* **50**, 30–38 (2005).

149. L. K. Horowitz, P. Goldberg, A study of Pleistocene and Holocene hyaena coprolites. *J. Archaeol. Sci.* **16**, 71–94 (1989).

150. R. Macphail, P. Goldberg, Geoarchaeological Investigation of Sediments from Gorham's and Vanguard Caves, Gibraltar: Microstratigraphical (Soil Micromorphological and Chemical) Signatures, in *Neanderthals on the Edge* (eds Stringer, C., Barton, C.M. & Finlayson C.) 183–200 (Oxbow, 2000).

151. L. Slimak, Les Dernières Expressions du Moustérien entre Loire et Rhône. Phd thesis, Université de Provence (2004).

152. L. Slimak, Le Néronien et la structure historique du basculement du Paléolithique moyen au Paléolithique supérieur en France méditerranéenne. *C. R. Palevol* **6**, 301–309 (2007).

153. L. Slimak, D. Pesesse, Y. Giraud, Reconnaissance d'une installation du Protoaurignacien en vallée du Rhône. Implications sur nos connaissances concernant les premiers hommes modernes en France méditerranéenne. *C. R. Palevol* **5,** 909–917 (2006).

154. J. Zilhão, D. E. Angelucci, E. Badal-García, F. d'Errico, F. Daniel, L. Dayet, K. Douka, T. F. G. Higham, M. J. Martínez-Sánchez, R. Montes-Bernárdez, S. Murcia-Mascarós, C. Pérez-Sirvent, C. Roldán-García, M. Vanhaeren, V. Villaverde, R. Wood, J. Zapata, Symbolic use of marine shells and mineral pigments by Iberian neandertals. *Proc. Natl. Acad. Sci. U.S.A.* **107**, 1023–1028 (2010).

155. M. Peresani, I. Fiore, M. Gala, M. Romandini, A. Tagliacozzo, Late Neandertals and the intentional removal of feathers as evidenced from bird bone taphonomy at Fumane Cave 44 ky B.P., Italy. *Proc. Natl. Acad. Sci. U.S.A.* **108**, 3888–3893 (2011).

156. C. Finlayson, K. Brown, R. Blasco, J. Rosell, J. J. Negro, G. R. Bortolotti, G. Finlayson, A. Sánchez Marco, F. Giles Pacheco, J. Rodríguez Vidal, J. S. Carrión, D. A. Fa, J. M. Rodríguez Llanes, Birds of a feather: Neanderthal exploitation of raptors and corvids. *PLOS ONE* **7**, e45927 (2012).

157. A. Gómez-Olivencia, N. Sala, C. Núñez-Lahuerta, A. Sanchis, M. Arlegi, J. Rios-Garaizar, First data of Neandertal bird and carnivore exploitation in the Cantabrian Region (Axlor; Barandiaran excavations; Dima, Biscay, Northern Iberian Peninsula). *Sci. Rep.* **8**, 10551 (2018).

158. R. Blasco, J. Rosell, A. Sanchez-Marco, A. Gopher, R. Barkai, Feathers and food: Human-bird interactions at Middle Pleistocene Qesem Cave, Israel. *J. Hum. Evol.* **136**, 102653 (2019).

159. M. Romandini, M. Peresani, V. Laroulandie, L. Metz, A. Pastoors, M. Vaquero, L. Slimak, Convergent evidence of eagle talons used by late neanderthals in Europe: A further assessment on symbolism. *PLOS ONE* **9**, e101278 (2014).

160. D. Radovčić, A. Sršen, J. Radovčić, D. Frayer, Evidence for neandertal jewelry: Modified white-tailed eagle claws at krapina. *PLOS ONE*, **10**, e0119802 (2015).

161. R. G. Klein, Out of Africa and the evolution of human behavior. *Evol. Anthropol.* **17**, 267–281 (2008).

162. A. M. Kubicka, Z. M. Rosin, P. Tryjanowski, E. Nelson, A systematic review of animal predation creating pierced shells: Implications for the archaeological record of the Old World. *PeerJ* **5**, e2903 (2017).

163. D. Garofoli, Do early body ornaments prove cognitive modernity? A critical analysis from situated cognition. *Phenomenol. Cogn. Sci.* **14**, 803–825 (2015).

164. W. Roebroeks, M. J. Sier, T. K. Nielsen, D. de Loecker, J. M. Pares, C. E. S. Arps, H. J. Mucher, Use of red ochre by early Neandertals. *Proc. Natl. Acad. Sci. U.S.A.* **109**, 1889–1894 (2012).

165. R. F. Rifkin, Assessing the efficacy of red ochre as a prehistoric hide tanning ingredient. *J. Afr. Archaeol.* **9**, 131–158 (2011).

166. P. R. B. Kozowyk, G. H. J. Langejans, J. A. Poulis, Lap shear and impact testing of ochre and beeswax in experimental Middle Stone Age compound adhesives. *PLOS ONE* **11**, e0150436 (2016).

167. S. Kadowaki, T. Kurozumi, H. Donald, Marine Shells from Tor Fawaz, Southern Jordan, and Their Implications for Behavioral Changes from the Middle to Upper Palaeolithic in the Levant, in *Learning Among Neanderthals and Palaeolithic Modern Humans*, Y. Nishiaki, O. Jöris, Eds. (Springer, 2019), pp 161–178.

168. J. F. Ewing, Preliminary note on the excavations at the Palaeolithic site of Ksâr 'Akil, Republic of Lebanon. *Antiquity* **21**, 186–196 (1947).

169. I. Azoury, F. R. Hodson, Comparing palaeolithic Assemblages: Ksar Akil, a Case Study. *World Archaeol.* **4**, 292–306 (1973).

170. K. Ohnuma, *Ksar Akil, Lebanon: A Technological Study of the Earlier Upper Palaeolithic Levels of Ksar Akil* (British Archaeological Reports International Series, 1988), vol. III: Levels XXV-XIV 338 pp.

171. C. A. Tryon, L. Metz, Archeological evidence for human dispersals around the Mediterranean basin? *Evol. Anthropol.* **28**, 233–235 (2019).

172. S. Kuhn, From Initial Upper Paleolithic to Ahmarian at Üçağızlı cave. *Anthropologie* **42**, 249–262 (2004).

173. S. L. Kuhn, M. C. Stiner, E. Güleç, I. Özer, H. Yılmaz, I. Baykara, A. Açıkkol, P. Goldberg, K. M. Molina, E. Ünay, F. Suata-Alpaslan, The early Upper Paleolithic occupations at Üçağızlı Cave (Hatay, Turkey). *J. Hum. Evol.* **56**, 87–113 (2009).

174. B. H. Smith, Patterns of molar wear in hunter-gatherers and agriculturalists. *Am. J. Phys. Anthropol.* **63**, 39–56 (1984).

175. C. G. Turner II, C. R. Nichol, G. R. Scott, Scoring procedures for key morphological traits of the permanent dentition: The Arizona State University Dental Anthropology System" in *Advances in Dental Anthropology*, M.A. Kelley, C.S. Larsen, Eds. (Wiley-Liss, 1991), pp. 13–31.

176. R. M. G. Martin, J.-J. Hublin, P. Gunz, M. M. Skinner, The morphology of the enamel-dentine junction in Neanderthal molars: Gross morphology, non-metric traits, and temporal trends. *J. Hum. Evol.* **103,** 20–44 (2017).

177. M. Martinón-Torres, M. M. de Pinillos, M. M. Skinner, L. Martín-Francés, A. Gracia-Téllez, I. Martínez, J. L. Arsuaga, J. M. B. de Castro, Talonid crests expression at the enamel–dentine junction of hominin lower permanent and deciduous molars. *C. R. Palevol* **13,** 223–234 (2014).

178. M. Buckley, M. Collins, J. Thomas-Oates, J. C. Wilson, Species identification by analysis of bone collagen using matrix-assisted laser desorption/ionisation time-of-flight mass spectrometry. *Rapid Commun. Mass Spectrom.* **23**, 3843–3854 (2009).

179. M. Pal Chowdhury, R. Wogelius, P. L. Manning, L. Metz, L. Slimak, M. Buckley, Collagen deamidation in archaeological bone as an assessment for relative decay rates. *Archaeometry*, **61(6),** 1382–1398 (2019).

180. M. Buckley, R. A. Fariña, C. Lawless, P. S. Tambusso, L. Varela, A. A. Carlini, J. E. Powell, J. G. Martinez, Collagen sequence analysis of the extinct giant ground sloths *Lestodon* and *Megatherium*. *PLOS ONE* **10**, e0139611 (2015).

181. R. Fleischmajer, J. S. Perlish, R. E. Burgeson, F. Shaikh-Bahai, R. Timpl, Type I and type III collagen interactions during fibrillogenesis. *Ann. N. Y. Acad. Sci.* **580**, 161 (1990).

182. R. J. Wenstrup, J. B. Florer, E. W. Brunskill, S. M. Bell, I. Chervoneva, D. E. Birk, Type V collagen controls the initiation of collagen fibril assembly. *J. Biol. Chem.* **279**, 53331–53337 (2004).

183. A. Baker, P. L. Smart, R. L. Edwards, D. A. Richards, Annual growth banding in a cave stalagmite. *Nature* **364**, 518–520 (1993).

184. A. Baker, C. L. Smith, C. Jex, I. J. Fairchild, D. Genty, L. Fuller, Annually laminated speleothems: A review. *Int. J. Speleol.* **37**, 193–206 (2008).

185. M. S. Roberts, P. L. Smart, A. Baker, Annual trace element variations in a Holocene speleothem. *Earth Planet. Sci. Lett.* **154**, 217–246 (1998).

186. J.M. Desmarchelier, *High-resolution Palaeoenvironmental Information from Southeast Australian Speleothems.* PhD Thesis, University of Tasmania, Australia (1999).

187. Y. Huang, I. J. Fairchild, A. Borsato, S. Frisia, N. J. Cassidy, F. McDermott, C. J. Hawkesworth, Seasonal variations in Sr, Mg and P in modern speleothems (Grotta di Ernesto, Italy). *Chem. Geol.* **175**, 429–448 (2001).

188. I. J. Fairchild, A. Baker, A. Borsato, S. Frisia, R. W. Hinton, F. McDermott, A. F. Tooth, Annual to sub-annual resolution of multiple trace-element trends in speleothems. *J. Geol. Soc. Lond.* **158**, 831–841 (2001).

189. P. Treble, J. M. G. Shelley, J. Chappell, Comparison of high resolution sub-annual records of trace elements in a modern (1911–1992) speleothem with instrumental climate data from southwest Australia. *Earth Planet. Sci. Lett.* **216**, 141–153 (2003).

190. K. Johnson, C. Hu, N. Belshaw, G. Henderson, Seasonal trace-element and stable-isotope variations in a Chinese speleothem: The potential for high-resolution paleomonsoon reconstruction. *Earth Planet. Sci. Lett.* **244**, 394–407 (2006).

191. H. M. Stoll, W. Müller, M. Prieto, I-STAL, a model for interpretation of Mg/Ca, Sr/Ca and Ba/Ca variations in speleothems and its forward and inverse application on seasonal to millennial scales. *Geochem. Geophys. Geosyst.* **13**, 1–27 (2012).

192. G. Nagra, P. C. Treble, M. S. Andersen, P. Bajo, J. Hellstrom, A. Baker, Dating stalagmites in Mediterranean climates using annual trace element cycles. *Nat. Sci. Rep.* **7**, 1–12 (2017).

193. S. Vandevelde, J.-L. Lacour, C. Quéré, L. Marie, C. Petit, L. Slimak, Identification du rythme annuel de précipitation des carbonates pariétaux pour un calage micro-chronologique des occupations archéologiques pyrogéniques: Cas de la Grotte Mandrin (Malataverne, Drôme, France) [Identification of parietal carbonates' annual precipitation rate for a microchronological setting of pyrogenic archaeological occupations: The Grotte Mandrin (Malataverne, Drome, France) case]. *BSGF Earth Sci. Bull.* **192**, 1–22 (2021).

194. J. Durcan, G. King, G. Duller, DRAC: Dose rate and age calculator for trapped charge dating. *Quat. Geochronol.* **28**, 54–61 (2015).

195. S. W. Hillson, E. Trinkaus, Comparative Dental Crown Metrics, in *Portrait of the Artist as a Child. The Gravettian Human Skeleton from the Abrigo do Lagar Velho and its Archaeological Context*, J. Zilhão, E. Trinkaus (Instituto Português de Arqueologia, Lisboa, 2002), pp. 356–364.

196. E. Barberia, M. C. Suárez, G. Villalón, M. Maroto, F. García-Godoy, Standards for mesiodistal and buccolingual crown size and height of primary molars in a sample of Spanish children. *Eur. J. Paed. Dent.* **10**, 169–175 (2009).

197. NESPOS Database, Neanderthal Studies Professional Online Service. (2020).

198. ESRF Paleontological Microtomographic database (2020); http://paleo.esrf.eu.

199. P. Bayle, R. Macchiarelli, E. Trinkaus, C. Duarte, A. Mazurier, J. Zilhao, Dental maturational sequence and dental tissue proportions in the early Upper Paleolithic child from Abrigo do Lagar Velho, Portugal. *Proc. Natl. Acad. Sci. U.S.A.* **107**, 1338–1342 (2010).

200. M. Le Luyer, *Dental Evolution in Late Pleistocene and Early Holocene Human Populations (19000–5500 Cal. BP): A Whole Crown Perspective in the Aquitaine Basin, Southwest France, and Its Margins.* PhD Thesis, Université de Bordeaux, France (2016).

201. C. Zanolli, L. Bondioli, A. Coppa, C. M. Dean, P. Bayle, F. Candilio, S. Capuani, D. Dreossi, I. Fiore, D. W. Frayer, Y. Libsekal, L. Mancini, L. Rook, T. Medin Tekle, C. Tuniz, R. Macchiarelli, The late early Pleistocene human dental remains from Uadi Aalad and Mulhuli-Amo (Buia), Eritrean Danakil: Macromorphology and microstructure. *J. Hum. Evol.* **74**, 96–113 (2014).